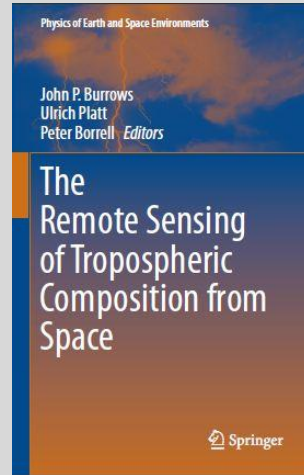**The Remote Sensing of Tropospheric Composition from Space**

Editors:
      John P. Burrows
      Ulrich Platt
      Peter Borrell

Pages 153 to 230

Chapter 4

Microwave Absorption, Emission and Scattering: Trace Gases and Meteorological Parameters

Klaus Kunzi, Peter Bauer, Reima Eresmaa,
Patrick Eriksson, Sean B. Healy, Alberto Mugnai,
Nathaniel Livesey, Catherine Prigent, Eric A. Smith
and Graeme Stephens

February 2011

Chapter 4
Microwave Absorption, Emission and Scattering: Trace Gases and Meteorological Parameters

Klaus Kunzi, Peter Bauer, Reima Eresmaa, Patrick Eriksson, Sean B. Healy, Alberto Mugnai, Nathaniel Livesey, Catherine Prigent, Eric A. Smith and Graeme Stephens

4.1 Introduction

Space-borne remote sensing techniques are widely used today to investigate the atmosphere, both by operational and experimental instruments on a large number of satellites. Sensors operating in the microwave range, defined as being wavelengths from 10 to 0.1 cm, frequency 3–300 GHz *(microwaves also comprise submillimetre waves or frequencies up to 3,000 GHz)* of the electromagnetic spectrum were among the first instruments used for this purpose from the ground and on board air- and space-borne platforms. Those instruments measured the thermal emission from a molecular resonance or used the absorption and scattering properties of water droplets or ice crystals to obtain information on atmospheric parameters and composition.

K. Kunzi (✉)
University of Bremen, Institute of Environmental Physics, Bremen, Germany

P. Bauer, R. Eresmaa and S.B. Healy
European Centre for Medium-Range Weather Forecasts (ECMWF), Reading, UK

P. Eriksson
Department of Earth and Space Sciences, Chalmers University of Technology, Gothenburg, Sweden

A. Mugnai
Istituto di Scienza dell'Atmosfera e del Clima, CNR, Roma, Italy

N. Livesey
Microwave Atmospheric Science Team, Jet Propulsion Laboratory, Pasadena, CA, USA

C. Prigent
CNRS, Observatoire de Paris, Paris, France

E.A. Smith
NASA/Goddard Space Flight Center, Greenbelt, MD, USA

G. Stephens
Colorado State University, Fort Collins, CO, USA

Measuring the atmospheric temperature profile using space-borne sensors observing thermal emission from molecular oxygen, O_2, was first proposed by Meeks (1961) and applied for the first time to data collected by the Nimbus-E Microwave Sensor (NEMS) on Nimbus-5 (Waters et al. 1975). The total water vapour content was first measured with combined 15 and 22 GHz radiometers on the Mariner-2 probe on Venus (Barath et al. 1964).

In the nineteen seventies, the Nimbus-E Microwave Sounder (NEMS) and the Scanning Microwave Sounder (SCAMS), flown on the Nimbus-5 and 6 satellites respectively, demonstrated the advantage of this type of instrumentation to retrieve parameters such as the atmospheric temperature profile, amounts of water vapour and liquid water. The frequency bands and observing geometries selected for these early instruments are still used today by operational sensors on meteorological satellites in polar orbits.

Microwave limb sensors, designed mainly to measure stratospheric composition, have become prominent since the launch of the Upper Atmosphere Research Satellite UARS by NASA. Such instruments also provide significant information on water vapour and minor constituents in the middle and upper troposphere with good vertical resolution.

Recently active sensors (radar) were used successfully to obtain information about the distribution of hydrometeors (suspended or falling liquid and solid particles). More recently also the signals from satellites of the Global Positioning System (GPS) are being used to retrieve temperature profiles and amounts of water vapour in the atmosphere.

Overall sensors operating in the microwave spectral range have evolved in the past decades to be an extremely successful atmospheric sounding technique, and these types of sensors are expected to remain cornerstones for remote sensing applications in atmospheric research, climatology and meteorology.

4.2   Atmospheric Remote Sensing in the Microwave range

4.2.1   Vector and Scalar Radiative Transfer

Three processes influence the intensity of electromagnetic radiation propagating through the troposphere: absorption, emission and scattering. The assumption of local thermodynamic equilibrium, as explained by Goody and Yung (1989), is valid for microwave radiation. As a consequence the atmospheric emission depends only on the local temperature and the local absorption. Gaseous absorption, and the associated emission, has generally no polarization dependency, one exception being the emission by the oxygen molecule, O_2.

The interaction of the O_2 with the radiation field is due to the magnetic dipole moment of two unpaired electrons; Zeeman splitting in the Earth magnetic field therefore affects the O_2 lines. The effect has to be considered when the lines get

very narrow in the upper stratosphere and above, making the thermal radiation dependent on the terrestrial magnetic field strength and orientation with respect to the polarization of the receiving antenna.

On the other hand, the interaction between radiation and particles, as well as the Earth's surface, normally causes the intensity to vary with the observed polarization. Different formalisms to describe the complete polarization state have been developed. In this work the Stokes vector (Bohren and Huffman 1998) will be used. In this case a real vector describes the intensity $\vec{I}$ and the general expression for the radiative transfer equation (Chandrasekhar 1960) can be written as:

$$\frac{d\vec{I}(m)}{ds} = -\bar{K}\vec{I} + \vec{a}B + \int_{4\pi} \bar{P}(m, m')\vec{I}(m')dm' \tag{4.1}$$

where m is the coordinate along the line of propagation, s is the distance along this direction, $\bar{K}$ is a matrix describing the extinction, i.e. the sum of absorption and scattering, $\vec{a}$ is the vector describing absorption, B is the Planck function, and the matrix $\bar{P}$ describes the scattering between the m' and m directions, normally denoted as the phase matrix.

The radiation measured by microwave radiometers is expressed as an equivalent black body temperature or brightness temperature T_B. The brightness temperature is defined as the physical temperature T_P of a black body emitting the same radiative power as that received from the observed target. For temperatures encountered in the Earth atmosphere and for frequencies below 200 GHz, the Planck law is adequately approximated for many applications by the Rayleigh-Jeans law, and the relationship between T_B and T_P becomes linear.

The three terms on the right-hand side of Eq. 4.1 describe respectively extinction, emission and scattering into line-of-sight. It is assumed that particles scattering the electromagnetic radiation are randomly and sparsely distributed and that the scattering by different particles is incoherent. The matrices $\bar{P}$ and $\bar{K}$ can then be set to represent ensemble properties. More detailed descriptions of the vector radiative transfer equation are found in Mishchenko et al. (2002) and Liou (2002).

The differential Eq. 4.1 is simplified for atmospheric conditions where particle scattering can be neglected. A scalar representation then suffices and an analytical solution is given by the following (Ulaby et al. 1981; Liou 2002):

$$I = I_l \exp\left(-\int_0^l k \cdot ds\right) + \int_0^l kB \exp\left(-\int_0^s k \cdot ds'\right) ds \tag{4.2}$$

where k is the absorption coefficient and l is the length of the propagation path. The first term on the right-hand side of Eq. 4.2 describes the intensity of the radiation at the start of the propagation path, I_l. This "background term" is the cosmic

background radiation for limb observations, while for downward measurements it is the sum of the surface emission and the reflected down-welling radiation. The second term on the right-hand side of Eq. 4.2 integrates the emission along the propagation path, weighted by the transmission between the observation and emission points.

Eq. 4.1 and Eq. 4.2 describe monochromatic radiation propagating along an infinitely narrow beam. In contrast, the response of an instrument has both a frequency and an angular extension. As a result radiative transfer calculations must normally be performed for a set of frequencies and propagation directions in order to correctly incorporate the frequency and angular responses of a particular instrument.

4.2.2   Gas Absorption in the Microwave Region

For microwave wavelengths H_2O, O_2 and N_2 are the dominating absorbing gases in the troposphere. O_2 dominates the absorption below 10–20 GHz (depending on altitude), by a line complex around 60 GHz and by individual transitions starting at 118.75 GHz. Water vapour is the main absorber close to the surface. Absorption by N_2, which lacks resonant transitions, becomes significant at higher altitudes, especially for frequencies at some distance from H_2O and O_2 resonances. More detailed calculations need to consider the absorption of ozone, O_3, and possibly also other minor atmospheric constituents. The calculated zenith absorption is shown in Fig. 4.1.

The position and strength of molecular transitions in the microwave region are known with a relatively high accuracy. In contrast pressure broadening and non-resonant absorption are less well known. Line broadening resulting from thermal motion (Doppler broadening) becomes important at altitudes around the stratopause and can be neglected for the troposphere. Pressure broadening causes a line shape of van Vleck and Weisskopf type, which, for higher altitudes and frequencies can be simplified to the Lorentz line shape (Rosenkranz 1993). The HITRAN database (Rothman et al. 2005) provides a complete set of parameters with the exception of O_2 around 60 GHz where line mixing must be considered. The Jet Propulsion Laboratory (JPL) spectral catalogue (Pickett et al. 2001) does not treat pressure broadening and covers only the microwave range, but it is considered to contain more accurate data for line position and strength.

Several mechanisms cause additional absorption not covered by summing up the resonant absorption of individual molecular transitions (Rosenkranz 1993). The additional non-resonant absorption is frequently denoted as continuum absorption, and must be considered for all the three main absorbers (H_2O, O_2 and N_2). For this reason, a number of absorption models were created, which provide a combination of data for most important transitions and empirically determined terms to incorporate continuum absorption (Liebe et al. 1993; Rosenkranz 1993; 1998). A detailed review of this topic is given by Kuhn (2003).
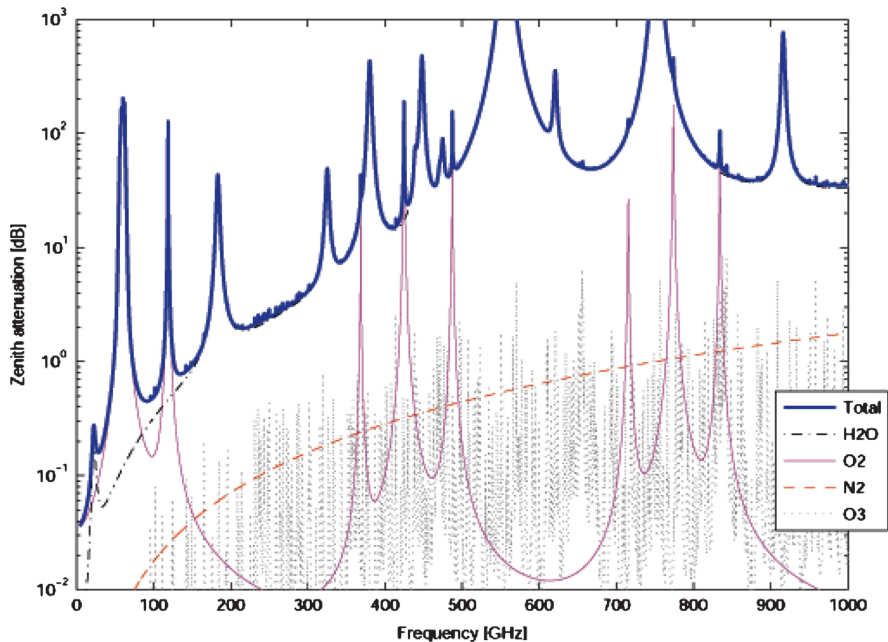
Fig. 4.1 The zenith attenuation for a mid-latitude winter scenario given in dB (Note that dB is a logarithmic measure for power ratios, 10 dB correspond to a factor of 10). The thick solid line gives the total attenuation, while the other lines show the contribution of each gas component. The water vapour profile has a liquid equivalent of 7 mm (*ca.* 2.3×10^{23} molecule/cm^2). Absorption was calculated by the Atmospheric Radiative Transfer Simulator ARTS-1.x (Eriksson and Buehler 2008). The absorption models of Rosenkranz (1998), Rosenkranz (1993) and Liebe et al. (1993) were used for H_2O, O_2 and N_2, respectively. Spectroscopic data for ozone were taken from the Jet Propulsion Laboratory (JPL) and High resolution Transmission Model (HITRAN) catalogues.

4.2.3   Particle Extinction in the Microwave Region

The scattering cross-section of any particle depends strongly on the ratio of its size and the wavelength of the electromagnetic radiation. Aerosols, with typical radii below 1 μm, do not scatter significantly because they are small compared to microwave wavelengths. For the same reason molecular scattering can safely be neglected. Also atmospheric aerosol densities are such that microwave absorption is negligible.

Ice and liquid water particles found in fog, clouds and precipitation are commonly denoted as hydrometeors, and the extinction of such particles can be very high. This extinction can be dominated by either absorption or scattering, depending on the particle size ranging from ~1 μm to ~1 cm, and the complex refractive index *n*, see Fig. 4.2.

The calculation of the complete phase matrix $\bar{P}$ is a challenge, Eq. 4.1, except for some special particle shapes. Spherical particles are treated by the Lorentz-Mie

theory (Liou 2002), while the so-called T-matrix approach addresses any rotationally symmetric particle such as spheroids and cylinders (Mishchenko et al. 2002). An example of a general calculation method is the Discrete Dipole Approximation (DDA) (Draine 2000), but its high demands on computational resources and memory strongly reduce the practical usefulness of the method. As it is so demanding to calculate the absorption and scattering properties for arbitrarily shaped particles and since the particle shapes are not well known, hydrometeors are frequently treated as spherical or have some shape handled by the T-matrix method. This is in general acceptable for liquid clouds and rain droplets, but is problematic for the treatment of ice particles that are highly variable in shape. Extinction and scattering cross-sections for spherical liquid and ice particles are shown in Fig. 4.3.

4.2.4 Simulation Software

A variety of computer codes with the purpose of simulating atmospheric radiative transfer are available, however the emphasis is placed on the general software developed especially for the microwave region, which is publicly available. A complete software package is required to enable the instrument responses to be
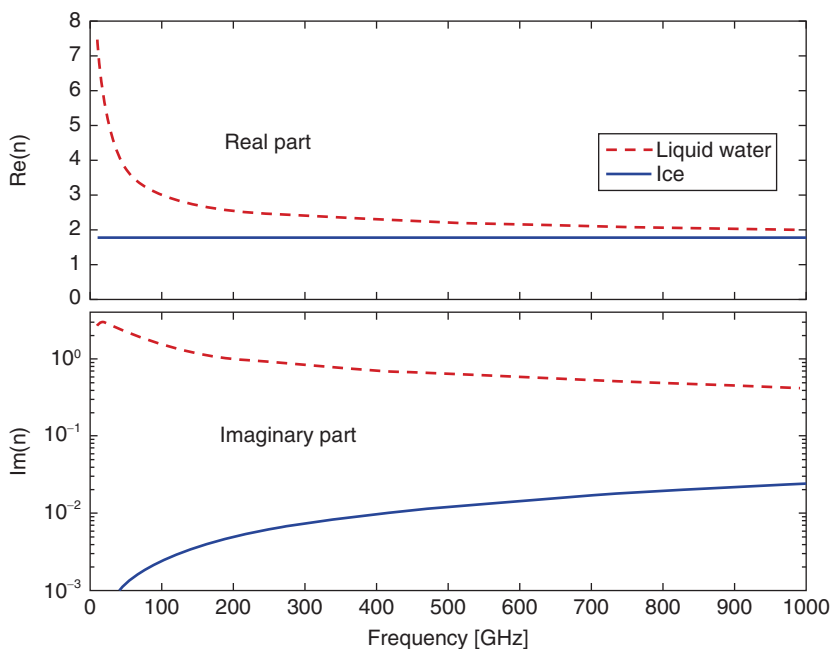

Fig. 4.2 The complex refractive index, n, of water for liquid and ice (Liebe et al. 1993). The real part determines the propagation speed, and the wavelength in the medium, while the imaginary part determines the medium's absorptivity.

incorporated. The term forward model is here used for such codes rather than the more restricted notation, such as radiative transfer code.

Most forward models dedicated to microwave applications describe only scalar radiative transfer without scattering and can thus be denoted as clear-sky models. Eight such forward models are presented and their consistency has been compared by Melsheimer et al. (2005). Most clear-sky forward models are developed for a specific instrument and are not distributed freely. The exceptions include the Atmospheric Transmission at Microwaves (ATM) (Pardo et al. 2001) and the Atmospheric Radiative Transfer Simulator, version 1 (ARTS-1) (Buehler et al. 2005). The retrieval methodologies normally applied for non-scattering measurements require the Jacobian matrix. That is, that the partial derivatives of the measured spectrum, with respect to the quantities to be retrieved, can be calculated. Expressions for Jacobian calculations are found in Buehler et al. (2005) and Read et al. (2006). The inclusion of instrument properties is given special attention in Eriksson et al. (2006). Clear-sky forward models assume in most cases a spherically symmetric one dimensional (1-D) atmosphere. Forward models, which allow atmospheric variables to vary in the horizontal dimension include the two dimensional (2-D) model by Read et al. (2006) and the three dimensional (3-D) development version of ARTS (v1.x) (Eriksson and Buehler 2008).
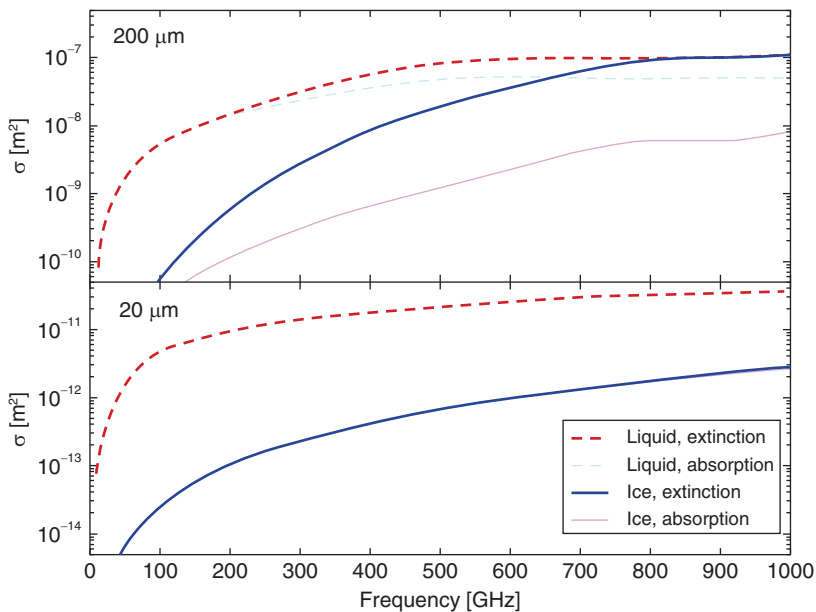

Fig. 4.3 Extinction and absorption cross-section σ of spherical liquid and ice water cloud particles with diameters of 200 μm (top) or 20 μm (bottom). The extinction of 20 μm particles is almost purely due to absorption. Refractive indexes as in Fig. 4.2 are assumed, and cross-sections are calculated with the Lorentz-Mie implementation by Mätzler (2002).

Scattering forward models differ in complexity with respect to radiative transfer implementation (scalar or vector), atmospheric dimensionality (1–3-D), allowed particle shapes, geometrical restrictions and surface scattering properties. The radiative transfer equation has no analytical solution in the case of scattering and different iterative solution methods have been developed. The selection of a solution method largely determines the calculation speed and main applications of a particular forward model. A review of 12 scattering codes is provided by Sreerekha et al. (2006), where, with the exception of ARTS-1.x (Eriksson and Buehler 2008), a flat Earth is assumed. The latter forward model has been developed to deal with vector radiative transfer and 3-D atmospheres. This is required for the accurate simulation of limb sounding observations. ARTS-1.x includes two scattering modules, Discrete Ordinate Iterative method (DOIT) (Emde et al. 2004) and reversed Monte Carlo (MC) (Davis et al. 2005). The latter and other MC algorithms provide comparably high calculation speed for 3-D calculations where the intensities for only a few directions are required (Battaglia et al. 2007). Other methods are favoured if larger portions of the complete radiation field are required. Another possible choice is then Spherical Harmonic Discrete Ordinate Method (SHDOM) (Evans 1998), which is a versatile and well-established scalar 3-D radiative transfer code, which has a rapid 1-D version called SHDOMPP. Another 1-D forward model frequently used for microwave measurements is the MicroWave MODel (MWMOD) (Czekala and Simmer 1998), which performs vector radiative transfer for non-spherical particles with non-random orientations.

As a result of the restrictions imposed by computer power, full radiative transfer calculations are not suitable for numerical weather prediction and fast regression models have therefore been developed. For example the fast Radiative Transfer (RTTOV) for the Television and Infrared Observation Satellite (TIROS) Operational Vertical Sounder (TOVS) (Eyre 1991) provides rapid simulations of radiances for satellite IR and microwave radiometers given an atmospheric profile of temperature, variable gas concentrations, cloud and surface properties (see Section 4.5.3). Later versions of RTTOV contain the forward, tangent linear, adjoint and full Jacobian matrices for the operational sensors. Clouds (liquid and ice) and rain can be considered. In the microwave, RTTOV computes the scattering effects using the delta-Eddington approximation.

The forward model for radar observations describes the particle back scattering as a function of distance to the transmitter assuming single scattering. The forward models and software discussed above describe the scattering of thermal emission. Multiple scattering of radar pulses requires dedicated software, such as Battaglia et al. (2006). Up to the present simulation of radar, which includes multiple scattering, are based on Monte Carlo methods.

4.2.5   The Inverse Problem

In most cases, remote sensing measurements form an ill posed problem, that is, a large, or infinite, number of geophysical states exist, which are consistent with the

measurement. One example of what could be considered as a unique measurement is the distance information provided by cloud radars, assuming that multiple scattering can be ignored. The task of extracting geophysical information from atmospheric remote sensing data requires special care because of the problem of non-uniqueness. The data extraction step using remotely sensed data is known as retrieval or inversion. A standard text for atmospheric data retrieval has been published by Rodgers (2000). It contains, for example, an updated presentation of the general method used for characterizing atmospheric inversion problems (Rodgers 1990). Additional information or constraints are needed to determine the best possible solution from a non-unique set of measurements. Several methodologies are used to solve ill posed problems, but for atmospheric sounding, statistical approaches are popular.

A theoretical starting point for statistically oriented retrievals is Bayes' theorem. This theorem is used to determine the probability distribution of all states after the measurement is performed, the *a posteriori* probability density function (PDF). A pure Bayesian method makes direct use of this PDF when choosing a solution. Common solutions take the most likely state (maximum of the PDF) or the expected value (PDF weighted state). The statistical constraint is provided as the *a priori* PDF of the state to be retrieved. This constrains the solution to a distribution of expected or known solutions. The *a posteriori* PDF can be determined in an analytical manner for linear, and in practice also moderately non-linear, inversion cases where both measurement uncertainties and *a priori* information follow Gaussian statistics. This solution is frequently referred to as the *optimal estimation method* (Rodgers 1976), while Rodgers (2000) prefers the general nomenclature of the *maximum a posteriori* solution. The most likely and expected states are identical and the *a posteriori* PDF is symmetric for the assumed conditions. The solution is here found by inverting the radiative transfer model, and the forward model must be able to provide the Jacobian matrix (Section 4.2.4).

Methods have been developed to determine *a posteriori* PDF for highly non-linear or non-Gaussian retrieval cases as well. These methods are, however, normally too computationally demanding to be practical. More efficient and potentially rapid processing is often achieved by obtaining the solution through a pre-calculated retrieval database. The basic challenge for such approaches is to generate an ensemble of atmospheric states that cover all relevant variables and mimic the true atmospheric variability with sufficient accuracy. The states in the retrieval database are distributed according to the *a priori* (multi-dimensional) PDF. The retrieval database is completed by calculating, using a radiative transfer tool, the measurement vectors corresponding to all the considered states of the atmosphere. The inversion is performed by finding a weighted average of the database states that are based on the similarity between the measurement and the simulated radiance. The weights for the database entries are calculated explicitly in the Bayesian Monte Carlo integration approach of Evans et al. (2002).

An implicit weighting is performed when the database is used for creating a regression model, including the training of neural networks (NNs). The application of NNs is growing. For example, early microwave satellite water vapour retrievals

used simple regression models (Staelin et al. 1976), while more recent algorithms tend to use NNs (Cabrera-Mercader and Staelin 1995; Jiménez et al. 2005). A general review of NNs for geophysical inversions is provided by Krasnopolsky (2007). To what extent a special implementation of these later methods can be viewed as Bayesian depends on how well the retrieval database matches the true atmospheric statistics and the optimisation constraint when determining the regression model parameters.

The estimation of the atmospheric state at a given time for the initialisation of numerical weather prediction (NWP) models involves complex data assimilation techniques. Assimilation is frequently performed inside a Kalman filtering framework that can be seen as an extension of the Bayesian method also covering time evolving states. For further details, readers are referred to Rodgers (2000). A brief summary of data assimilation and the contribution of microwave remote sensing to current NWP are given in Section 4.5.4.

4.2.6   Observing Technique

Microwave radiometers measure the thermal emission from a target. These types of sensors, which use radiation present in the system, are termed passive; in contrast instruments which emit radiation and then measure the backscattered signal are called radar, and will be considered in Section 4.7. A more general treatment of microwave radiometers can be found in the chapter by Tiuri (1966) in the book by Vowinkel (1988) (pp 236–293) and in the book edited by Janssen (1993).

Fig. 4.4 shows schematically the building blocks of a radiometer. Initially the antenna receives the thermal emission from the target. The spatial resolution of the instrument is given by the refraction limited beam width of the antenna, which is proportional to λ/D, where D is the antenna diameter and λ, the observed wavelength. The next element in the instrument chain is the calibration unit. The very high amplification (*ca.* 100 dB) needed for microwave radiometers require a careful and frequent calibration to minimise unavoidable gain drifts and fluctuations. Such an instrument is called a Total-Power-Radiometer (TPR) and instruments of this type are generally used today. A TPR is calibrated by switching black bodies at well-known temperatures in front of the radiometer. The "hot" black body is typically a microwave absorber at a well-monitored temperature. The cold calibration element is, for space-borne sensors, the cold background radiation of approximately 2.7 K. The frequency for the calibration process is determined by measuring the Allen-Variance (Allan 1966; Rau et al. 1984; Ossenkopf 2008), which determines the period for which gain variations of the instrument are negligible.

The calibration is followed by the amplifier. Up to frequencies in the order of 100 GHz (wavelength 3 mm) direct amplification is feasible by solid-state devices. As a result of the lack of amplifiers for higher frequencies, down-conversion of the original signal to a much lower frequency by using a heterodyne receiver is
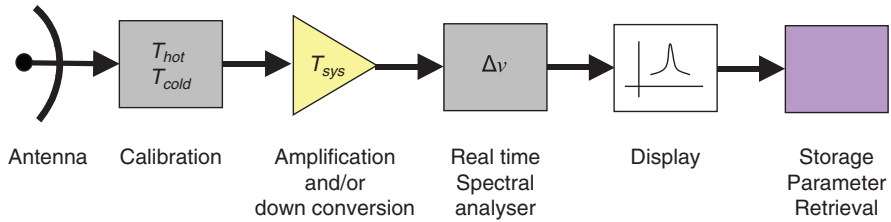
Fig. 4.4 Building blocks of a microwave radiometer.

preferred. This is achieved by using a non-linear element, typically a diode, and a local oscillator. The down-converted signal at the intermediate frequency is then amplified by standard components. The radiometer is characterized by its system noise temperature T_{sys} that is defined as the temperature of a black body at the input of a totally lossless and noiseless instrument, producing the same output power as found for the real system.

The next element in the detection chain is the real time spectral analyser, which is used for resolving the line shape of an emission line. Depending on the application, the width of individual channels range from more than 100 MHz down to less than 0.1 MHz. For applications where no high frequency resolution is needed the bandwidth of a microwave radiometer can be as large as many 1,000 MHz.

The last steps in the detector chain is the data display, storage and processing, providing the desired geophysical parameter.

The quantity, which determines the sensitivity of a radiometer, is the thermal noise generated in the various electronic elements of the receiver and also unavoidable losses in passive components such as transmission lines. The sensitivity of the radiometer is characterised by its system noise temperature, T_{sys}. Typical values for T_{sys} are shown in Fig. 4.5 for receiver types presently used. The quantity characterizing the sensitivity of a radiometer is the minimum detectable temperature difference Δt_{min} when observing a given target, Δt_{min} can be calculated from the following expression

$$\Delta t_{\min} = \frac{T_{sys}}{\sqrt{\Delta v \cdot \tau}} \qquad (4.3)$$

with Δv the selected spectral resolution and τ the integration time for one single measurement.

For real time spectrum analysis various techniques are available with Filterbanks, Acousto-Optical-Spectrometers (AOS), being frequently used. Recently broadband Fast Fourier Transform Spectrometer (FFTS) became available. This approach is described in Klein et al. (2006), who also provide a brief review of the other types of real time spectrum analysers. All types offer total bandwidth in excess of 1,000 MHz and can provide a spectral resolution to resolve easily the exact shape of atmospheric emission lines.
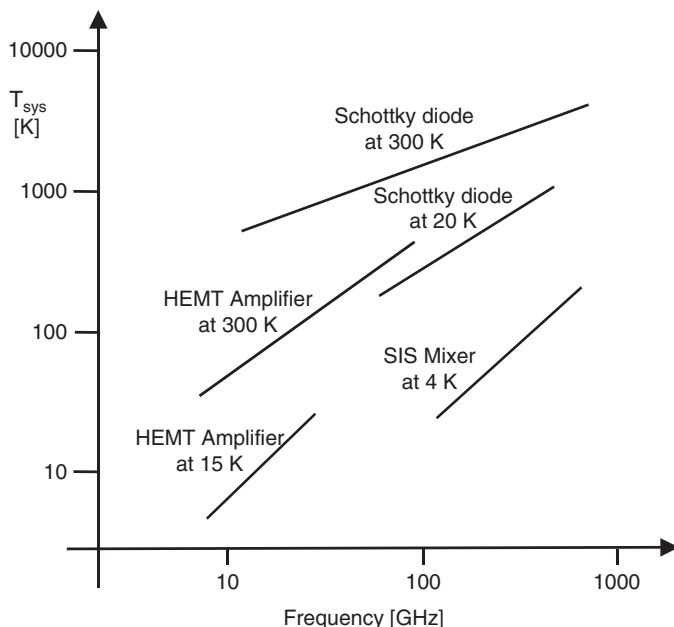
Fig. 4.5 Typical system noise temperature T_{sys} limits of various radiometric receivers. A substantial improvement in noise temperature is possible by cooling; examples are the Schottky diode mixers and the High Electron Mobility Transistor (HEMT) amplifiers. The Superconducter-Insolator-Superconducter (SIS) device is by far the most sensitive receiver but requires cooling to 4 K.

4.3   Temperature and Water Vapour Profiles

4.3.1   Introduction

Similar to the methods first developed for IR observations, the retrieval of atmospheric profiles from microwave observations is based on the different absorption of atmospheric gases at different frequencies around an absorption line. Since in the troposphere, line width is proportional to pressure, the absorption decreases rapidly with altitude at a given frequency off the line centre, for a molecule with a constant mixing ratio such as O_2. If the absorption at a particular frequency off the line centre is high, making the total atmosphere opaque or nearly opaque, it can be seen that the radiation received by a downward looking sensor on a spacecraft originates mainly from a layer at a particular altitude h_{peak}, since for higher altitudes the absorption and therefore also the emission reduces rapidly due to the narrowing of the emission line. On the other hand for altitudes considerably lower than h_{peak}, the radiation will be absorbed by the strong absorption of higher

layers. This explains qualitatively the concept of weighting functions as shown in Fig. 4.6.

If the mixing ratio of the particular molecule is constant, as assumed above, the received radiation at various frequencies off line centre, which corresponds to various pressure altitudes, will allow the retrieval of the atmospheric temperature profile. Emission from O_2, which is uniformly mixed up to nearly 100 km, is well suited to estimate the atmospheric temperature profile. On the other hand, if the temperature profile is known, the only unknown is the concentration of the particular molecule. The temperature profile in the atmosphere is not highly variable with time at a given location, and the response of the measured signal to changes in temperature is nearly linear (Rayleigh-Jeans approximation), which is in contrast to thermal IR where a highly non-linear relation exists near the peak of the Planck function. This fact allows for the retrieval of atmospheric species from microwave radiances with good accuracy even with a poorly known temperature.

Fig. 4.6 presents the temperature and water vapour weighting functions for O_2 lines at 57.290 GHz and 118.750 GHz and for the 183.310 GHz H_2O line. The H_2O line around 22 GHz is very weak and not suitable for profile retrievals (the weighting functions for this line are very broad). Nevertheless observations near this line can provide the integrated water vapour in the atmosphere over ocean, where the water vapour appears in emission in front of a cold background due to the low emissivity of the ocean surface. The 50–60 GHz O_2 band and both the 22 GHz and the 183 GHz H_2O lines are the spectral regions currently used by operational meteorological satellites for temperature and water vapour measurements.

Due to the increasing opacity of the atmosphere and the perturbing effect of clouds and precipitation with increasing frequency, O_2 and H_2O lines at higher frequencies are not currently used for atmospheric profiling in a downward looking geometry. However since the satial resolution of microwave sensors is limited by the size of the antenna (Section 4.2.6), it has been suggested that higher frequencies for instruments on geostationary satellites be used, for example the Geostationary Observatory for Microwave Atmospheric Sounding (GOMAS) proposed to the European Space Agency (ESA). From Fig. 4.6 it can be seen that weighting functions at 57.290 and 118.750 GHz are very similar under clear sky conditions. Note that the spatial resolution near 118 GHz is better by nearly a factor of two compared with frequencies near 60 GHz, for a given antenna size. The performances and limitations of sensors operating at higher frequencies are investigated by Klein and Gasiewski (2000) and Prigent et al. (2006).

The microwave spectral regions used to sound the lower atmosphere must be sufficiently transparent; examples are the 22 GHz water vapour line, or the O_2 lines with weighting functions intersecting the surface. However in this case surface emission needs to be treated explicitly. As pointed out above, the ocean emissivity is low, ~0.5, and its dependence on the sea and instrument characteristics, such as temperature, surface wind speed, salinity and the observing geometry, can be modelled. However, land surface emissivity is large, typically being ~0.95, and depends on a large number of poorly known parameters, such as soil moisture, vegetation type, snow cover and type, parameters having high spatial and temporal
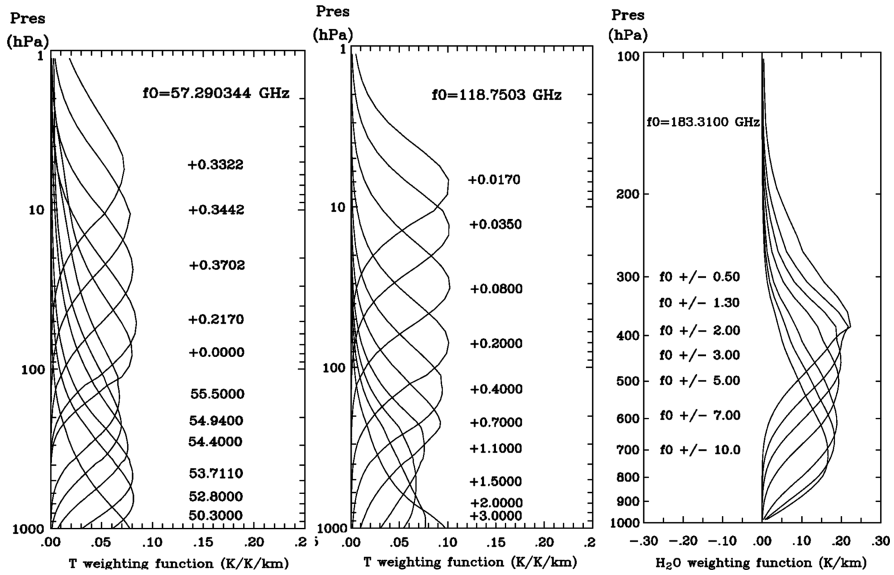
Fig. 4.6 Monochromatic weighting functions for selected frequencies near the 57 GHz O_2 band (left), the 118 GHz O_2 line (centre) and the 183 H_2O line (right), calculated for nadir sounding over land (a surface emissivity of 1 is assumed) for a mean standard atmosphere. Weighting functions show the sensitivity as a function of altitude (Prigent et al. 2005).

variability. As a result of the high emissivity, the brightness temperature of the land surface is close to the physical temperature of the surface. As the temperature of the lower atmospheric layers is very similar to the surface brightness temperature, the contrast between the surface emission and that from the lower atmospheric signal is small, reducing the sensitivity to the lower troposphere and the retrievals of atmospheric parameters requires an adequate knowledge of the surface emission. For this reason, surface-sensitive channels are not used over land to retrieve data products in the operational centres, but attempts have been made in a research mode (Karbou et al. 2005).

4.3.2   Examples

After a few tests in the Earth atmosphere with instruments on the Russian Cosmos satellites (Akvilonova et al. 1973), the NEMS instrument on the Nimbus-5 meteorological satellite provided the first global maps of integrated water vapour column amount over the ocean. The retrieval technique comprised a multi-dimensional regression analysis, trained on simulated radiances computed using data from radiosondes at different latitudes over a 2-year period (Staelin et al. 1976). The accuracy

of the retrieved integrated water vapour column was claimed to be 0.2 g/cm^2. Schaerer and Wilheit (1979) described water vapour profiling using the strong H$_2$O line at 183 GHz, which became available after 1991 with the launch of the Special Sensor Microwave/Temperature-2 (SSM/T-2) instrument (Manning and Wang 2003).

Most operational atmospheric microwave sounders observe with a cross-track scanning geometry at incidence angles between 0° and 55°. Examples are the SSM/T-1 and 2, the Microwave Sounding Unit (MSU), the Advance Microwave Sounding Unit (AMSU-A and B) and the Humidity Sensor for Brasil (HSB). An exception is the Special Sensor Microwave Imager (SSM/I), which includes both sounding and imaging frequencies, using a conical scanning geometry.

Rosenkranz et al. (1997) compared the performances of the two scanning geometries, cross-track and conical, for profiling applications. So-called window channels are included between the molecular resonances to measure surface properties, such as the wind speed over ocean, soil parameters and to obtain additional information on hydrometeors.

4.4 Remote Sensing of Clouds and precipitation

4.4.1 Introduction

Hydrometeors require the radiative transfer to include the effects of scattering. In contrast to visible and IR instruments, which are only sensitive to radiation scattered or emitted from the top of the cloud, microwave radiation can penetrate clouds and precipitation to some degree. The penetration depth depends strongly on the ratio between the hydrometeor size and the wavelength, and on the phase of the hydrometeors, ice, or liquid. As a result of the large imaginary part of the refractive index of liquid water in the microwave range (Fig. 4.2), liquid particles significantly absorb and emit microwave radiation. Ice particles on the other hand, with a small imaginary refractive index, mainly scatter microwave radiation. At frequencies below 50 GHz, the microwave signal is essentially dominated by emission and absorption by liquid clouds and rain and is little affected by the presence of ice clouds. At higher frequencies, scattering effects on frozen particles increase, eventually masking the signal from the liquid cloud and rain.

The remote sensing of clouds and precipitation and the retrieval of data products relies on an accurate understanding of the interaction between the radiation and the hydrometeors. For each frequency the radiation measured by the radiometer is determined by the phase, size and shape distribution, and vertical profile of the hydrometeors.

The microwave radiative transfer in scattering atmospheres has been recently reviewed in depth by Battaglia et al. (2006). A comparison of several multiple scattering radiative transfer models (two-stream, multiple stream and Monte Carlo) concluded that differences between the codes were small (Smith et al. 2002). The main difficulties in simulating the microwave response of clouds and precipitation stem from the lack of information about the particle spatial distribution and their physical properties.

Cloud resolving models, for example Meso-NH (Lafore et al. 1998) or the Goddard Cumulus Ensemble model (Tao and Simpson 1993), can provide high-resolution 3-D structures of the hydrometeor content, along with some indication about the particle size distribution, shape, and phase (ice or water). For instance, Meso-NH calculates the distribution of five parameters (cloud droplet, pristine ice, rain, graupel, and snow) having horizontal and vertical resolutions of the order of 1 km and 100 m respectively. Aircraft campaigns can also give information on particle properties. However, large uncertainties in the description of the physical properties of frozen particles result in significant errors in the interpretation of microwave observations, especially in convective situations at frequencies above 50 GHz.

Fig. 4.7 presents simulations with and without hydrometeors for the ATM Model (Pardo et al. 2001) with a mean standard atmosphere, over ocean and land. The water content of clouds is expressed in cloud liquid water (CLW) which is given by the column in g/m^2 of liquid water integrated over the cloud layer along the line of sight of the instrument. Cloud ice water content is similarly defined.

During the emission/absorption process, liquid particles cause brightness temperatures to increase over a radiatively cold background such as the ocean; the induced warming of the signal increases with frequency up to a saturation level (Fig. 4.7 left, middle). Retrieval of the cloud liquid water path over ocean is currently based on the signals measured between 19 and 85 GHz. Over land, signals from clouds and rain are much weaker (Fig. 4.7 right, middle). However, when frozen particles are large enough with respect to the wavelength, scattering reduces the amount of radiation measured by the sensor, due to scattering of the cold space background. The scattering signal can be used to estimate the cloud ice content and precipitation over ocean and land (Fig. 4.7 bottom). However, the emission originating in the liquid lower part of cloud and rain layers is affected by the scattering process in the upper part of the cloud, especially at higher frequencies.

Satellite observations from the Tropical Rainfall Measuring Mission (TRMM) Microwave Imager (TMI) (TRMM, radar is discussed in Section 4.7) between 10 and 85 GHz are shown in Fig. 4.8 for Hurricane Bret on 22nd August 1999 in the Gulf of Mexico. The top and middle rows show the vertical and horizontal polarizations respectively for the five frequencies. For frequencies below 40 GHz, the cloud results in a warming of the brightness temperatures over ocean and a small cooling over land for both polarizations. At 85 GHz a significant decrease of the brightness temperatures is observed in the spiral arms of the hurricane, where large
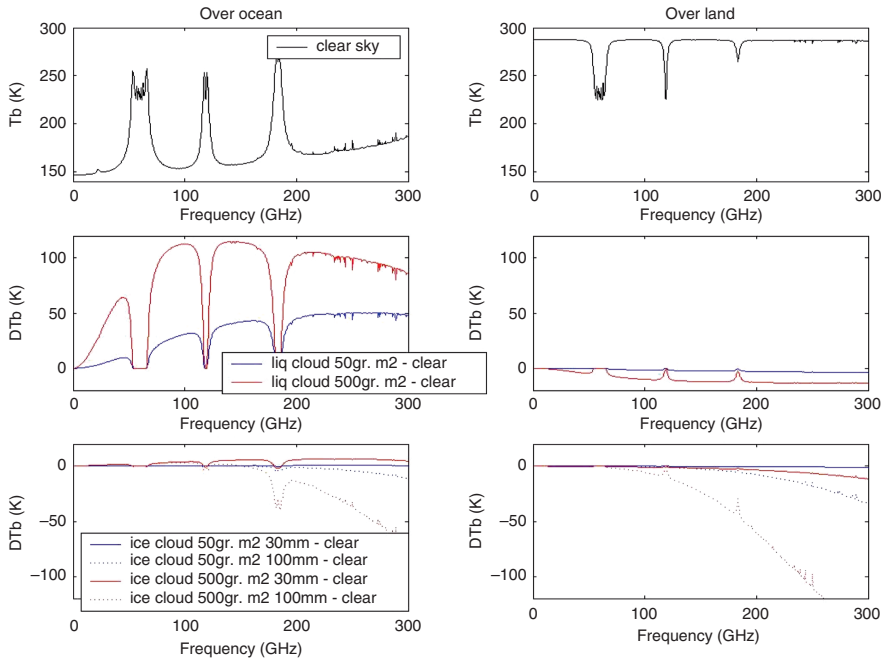
Fig. 4.7 Simulations with the ATM (Pardo et al. 2001), for a mean standard atmosphere, over ocean (left) and land (right). The brightness temperatures Tb under clear sky conditions are presented (top two figures), for an incidence angle of 53°. The surface emissivity is assumed to be 0.5 over ocean and 1 over land. The brightness temperatures difference DTb due a cloud is calculated as DTb = Tb(cloudy) – Tb(clear), for two clouds extending from 2 to 3 km altitude (middle two figures) with a CLW of 50 g/m^2 and 500 g/m^2 and correspondingly for two ice clouds extending from 7 to 8 km altitude (bottom two figures) with a CIW of 50 g/m^2 and 500 g/m^2. Single size spherical particles are considered, water particles have a diameter of 20 μm and ice particles have diameters D of 60 or 200 μm.

quantities of frozen particles scatter the signal. The lower the frequency, the more transparent the clouds become. Large polarisation differences have been observed over ocean at 10 GHz (lower row) even in the presence of clouds because of the almost transparent atmosphere and the strong dependence of ocean surface reflectivity on polarization. At 85 GHz no contrast is observed between ocean and land, because the atmosphere is nearly opaque at this frequency. Note also the increase in spatial resolution from 10 to 85 GHz (from 37·63 km^2 to 5·7 km^2), because the instrument uses the same antenna for all frequencies.

Several studies have characterized the convective activity based on passive microwave scattering observations (Mohr et al. 1999; Hong et al. 2005a; 2005b) or correlate the scattering signal to the radar reflectivity or to the electrical activity (Nesbitt et al. 2000; Cecil et al. 2005; Prigent et al. 2005). They all show that scattering by ice above 80 GHz is a very sensitive indicator of the convective strength, and provides information on the cloud microphysics.
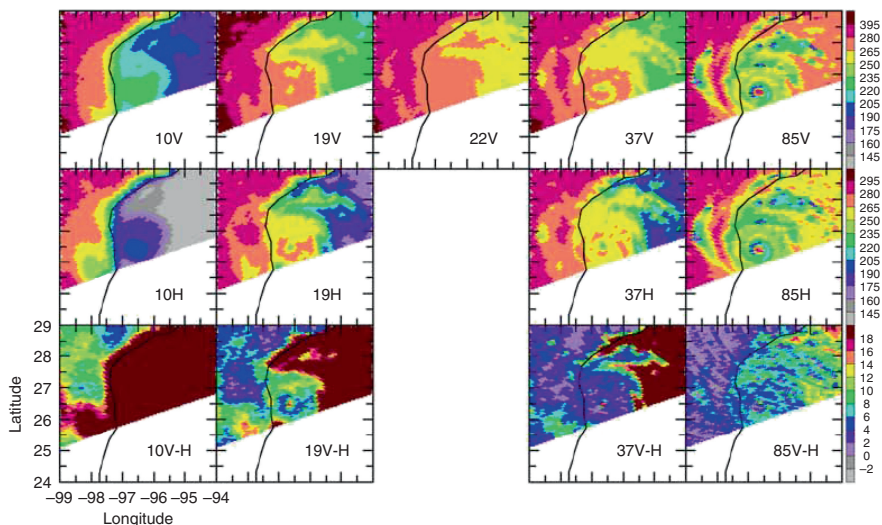
Fig. 4.8 Satellite observations of the brightness temperature from TMI between 10 and 85 GHz (see frequencies and polarization in plots) are presented for Hurricane Bret on 22nd August 1999, in the Gulf of Mexico. The top and middle rows show the vertical and horizontal polarizations for the five frequencies, whereas the polarization difference is displayed in the bottom row. The coastline is indicated by a solid black line. Fig. from Wiedner et al. (2004).

4.4.2   Retrieval of Cloud Liquid Water

Estimates of CLW are used for climate model validation and to study the impact of clouds on the radiative budget as described in Stephens and Greenwald (1991) and Borg and Bennartz (2007). The retrieval of CLW requires a high accuracy of the measurement (L'Ecuyer and Stephens 2003; Turner et al. 2007). An advantage is that microwave measurements yield consistent cloud data during the day and night and are quite insensitive to the cloud particle size distribution, and are not impacted by the presence of thin ice clouds (cirrus) in contrast to passive remote sounding in the visible.

As pointed out earlier, small liquid droplets with a radius below 50 μm, typical for non-precipitating clouds, absorb and emit microwave radiation but do not scatter significantly. The absorption from such liquid particles is proportional to the CLW [Rayleigh approximation, (Ulaby et al. 1981)]. CLW over ocean is routinely estimated from the emission measured between 19 and 85 GHz by imagers such as SSM/I, TMI, or the Advanced Microwave Scanning Radiometer (AMSR).

Over ocean: Different types of algorithms have been developed to retrieve CLW over the ocean from microwave observations, but all of them suffer from the lack of validation measurements. Estimates of CLW from ground-based microwave measurements are considered as the most direct and most reliable data for validation.

Contrary to the satellite case, the ground-based estimates are not contaminated by surface contributions, and are therefore more accurate. Alishouse et al. (1990) developed a statistical algorithm to estimate CLW from a few coincident satellite observations with ground-based radiometric estimates of CLW.

The majority of CLW retrieval algorithms are derived from statistical regressions between simulated radiances and cloud water content, for typical atmospheric and cloud conditions. The difficulty is to find a set of representative situations due to the large spatial and temporal natural variability. Pioneer work was conducted with a two-channel algorithm using data collected at 22 and 31 GHz from observations with the NEMS instrument on Nimbus-5 (Staelin et al. 1976). Subsequent developments tend to use more channels (Chang and Wilheit 1979) or suggest the use of different sets of frequencies, depending on the liquid water range (Weng and Grody 1994), with the low frequency (below 30 GHz) less likely to saturate for high CLW, and the higher frequencies around 85 GHz more sensitive to low CLW. The complexity of the radiative transfer models varies from simple codes for non-scattering clouds (Greenwald et al. 1993; Weng and Grody 1994) to multi-scattering transport models (Liu and Curry 1993; Bauer and Schluessel 1993). The theoretical error is generally claimed to be in the 10 to 30 g/m^2 range. A climatology of CLW has been established from this type of algorithm (Weng et al. 1997). Collocated visible and IR information can be used to separate clear and cloudy pixels to constrain the problem (Liu and Curry 1993).

So-called physical algorithms minimize iteratively the difference between observed and simulated radiances using the radiative transfer equation and a first guess (Prigent et al. 1994; Wentz 1997). Several geophysical variables are retrieved simultaneously, to ensure consistency (usually water vapour, cloud liquid water, ocean surface wind speed, and rain rate). Direct assimilation of the radiances from microwave imagers into a Numerical Weather Prediction (NWP) model was tested by Phalippou (1996) to retrieve the cloud liquid water along with the water vapour and surface wind speed over ocean. This 1-D variational assimilation is now used routinely at the European Centre for Medium Range Weather Forecast (ECMWF), but more advanced CLW estimates from 4-D assimilation is not yet performed by NWP centres.

Due to the lack of systematic CLW *in situ* measurements, the microwave-derived CLW products have been evaluated by comparisons with estimates from IR/vis observations, such as the products from the International Satellite Cloud Climatology Project (ISCCP) (Lin and Rossow 1994), or the estimates from MODIS (Greenwald et al. 2007). An inter-comparison of four published and well-accepted CLW algorithms based on SSM/I data showed significant differences in the tropics with up to a factor of 4 between the lowest and the largest estimates, even when averaged over a month and over latitude bands (Deblonde and Wagneur 1997). The discrepancies were attributed to the partition between CLW and rain, to the lack of sensitivity to low CLW, to the scarcity of *in situ* measurements for calibration, and to the beam-filling problem. Using comparisons between AMSR-derived CLW and MODIS estimates, Greenwald et al. (2007) confirm the influence of the beam filling issue but also found a dependence of the microwave CLW product on the surface wind speed over ocean.

The combination of multi-sensor observations is suggested to partly overcome these problems. Horváth and Davies (2007) compared CLW estimated from microwave observations (TMI) and optical measurements from MODIS and the Multiangle Imaging Spectro Radiometer (MISR). The agreement is satisfying for warm clouds (correlation of 0.85 and rms difference of ~25 g/m^2) with an overestimation for cloud fractions below 65%; however the errors are much larger for cold clouds.

Over land: The land surface emissivity is usually close to unity, making atmospheric features difficult to identify against such a background because of the small contrast. In addition, the emissivity is variable in space and time and difficult to model since it depends on the topography, vegetation, soil moisture, and snow, among other factors. In order to retrieve CLW over land from microwave measurements, Jones and Vonder Haar (1990) suggested first estimating the land surface microwave emissivity from collocated visible, IR, and microwave observations under clear sky conditions, and then to use the emissivity for determining the CLW. Promising results were obtained over central USA. Prigent and Rossow (1999) and Aires et al. (2001) developed a similar technique to be used globally. Aires et al. (2001) is based on a neural network scheme to retrieve simultaneously the surface skin temperature, the water vapour content, and the cloud liquid water, based on a large simulated database, with realistic cloud parameters derived from ISCCP (Rossow and Schiffer 1999). This approach leads to a theoretical rms error in CLW of 80 g/m^2.

4.4.3   Retrieval of Cloud Ice Water

Global coverage of ice clouds is ~30% on average (Stubenrauch et al. 2006), and shows a very large variability from thin cirrus to thick anvils (Heymsfield et al. 2004) with CIW varying from 5 to more than 1,000 g/m^2 and particle equivalent sphere diameter, D_e, from 10 to more than 1,000 µm. No existing satellite instrument is capable alone of observing the full range of CIW and D_e. Due to the wavelength-to-size ratio, visible techniques are very sensitive to small particles. IR techniques become insensitive for particle diameters above ~100 µm. Microwave to sub-millimetre observations can complement the visible and infrared measurements, and provide ice cloud characteristics for larger particles and optically thick clouds.

Before 1987, space borne microwave observations by imagers were limited to frequencies below 37 GHz. At these frequencies, negligible effects due to ice clouds are expected, with the exception of deep convective cores (Spencer et al. 1983). Estimating CIW from microwave observations was first suggested by Evans and Vivekanandan (1990) by simulating the effect of various ice crystal shapes at 37, 85, and 157 GHz. With the availability after 1987 of the SSM/I channel at 85 GHz, CIW have been estimated from microwave observations, using radiative transfer modelling (Weng and Grody 1994; Bauer and Schluessel 1993). Lin and Rossow (1996) and Minnis et al. (2007) have suggested adding visible and IR to the

microwave observations in order to constrain the problem and obtain more accurate CIW estimates. Retrieval of CIW from space-borne microwave observations above 100 GHz has been tested by Liu and Curry (1999), using the relationship between CIW and the brightness temperature depression at 150 GHz of the SSM/T instrument. Based on their experience with the aircraft Millimetre-Wave Imaging Radiometer (MIR), Liu and Curry (2000) estimate CIW from measurements with the 89 and 150 GHz AMSU-B channels, using simple scattering efficiency estimates from cloud models and radiative transfer calculations (Ferraro et al. 2000; Weng and Grody 2000). These algorithms are limited to CIW above 300 g/m^2. Greenwald and Christopher (2002) conducted a near-global analysis of coincident 183 GHz AMSU-B measurements and thermal IR data from the Advanced Very High Resolution Radiometer (AVHRR) in order to estimate the effect of cold clouds at millimetre wavelengths. They confirm that non-precipitating cold clouds have a rather weak impact on the 183 GHz brightness temperature (of the order of 1.4K), whereas precipitating clouds have a much larger effect (around 7K). The brightness temperature depression at 183 GHz is difficult to relate to a quantitative characterization of clouds or rain, because it is a complicated function of hydrometeor type, size, and profile.

In order to understand the relationship between the physical and radiative properties of frozen hydrometeors, many efforts have been undertaken recently, with simulation studies (Liu 2004; Kim 2006), with comparison with satellite data (Meirold-Mautner et al. 2007) and with aircraft observations (Skofronick-Jackson et al. 2008).

Several modelling studies explored the potential of the sub-millimetre domain for ice cloud characterization and concluded that several, widely spaced frequencies can determine CIW and ice particle size distribution (Gasiewski 1992; Evans and Stephens 1995a; 1995b). Evans et al. (1998) extended the previous studies with the objective of deriving an algorithm to estimate the global distribution of ice mass from observations at 150, 220, 340, 500, 630, and 880 GHz. Additional observations near the H$_2$O line at 183 GHz have been suggested for quantifying the water vapour contribution above the cloud (Evans et al. 2005). Millimetre and sub-millimetre receivers have been developed and flown on board aircraft, such as the Goddard Space Flight Center (GSFC) MIR including channels at 85, 150, 183, 220, and 325 GHz (Racette et al. 1996). This sensor has collected data during several measurement campaigns (Wang et al. 1998; Liu and Curry 1998; Deeter and Evans 2000; Skofronick-Jackson et al. 2003). The Conical Scanning Submillimetre-wave Imaging Radiometer (CoSSIR), which has 12 channels at 183, 220, 380, 487, and 640 GHz was used by Evans et al. (2005) during the CRYSTAL-FACE campaign to test a Bayesian retrieval algorithm of CIW and D_e, in comparison to coincident 94 GHz airborne radar observations. A Fourier Transform Spectrometer (FTS), the Far IR Sensor for Cirrus (FIRSC) for use on an aircraft, has also been developed to explore the whole sub-millimetre region between 300 GHz and 3,000 GHz (Evans et al. 1999; Vaneck et al. 2001). This wide coverage in frequency provides high sensitivity for a large range of particle sizes.

Following these simulation studies and results from aircraft campaigns, satellite instruments have been proposed to the space agencies. In Europe, the Cloud Ice
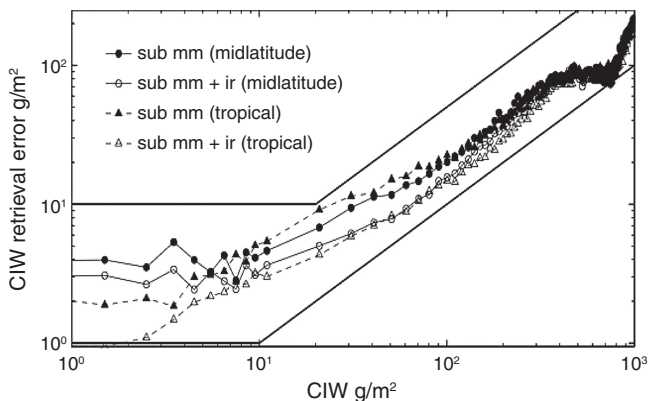
Fig. 4.9 Theoretical errors using the CIWSIR instrument to retrieve the CIW as a function of CIW, for two types of atmospheres (mid-latitude and tropical), with and without IR information (Buehler et al. 2007).

Water Sub-millimetre Imaging Radiometer (CIWSIR) (Kunzi et al. 2001; Buehler et al. 2005; 2007) is a conically scanning instrument to be flown on a polar orbit in tandem with MetOp, with 12 channels around 183, 243, 325, 448 and 664 GHz, and a thermal IR channel. A similar instrument has been proposed in the US by Ackermann et al.

Simulations show that CIWSIR can provide CIW with a detection threshold of 2 g/m^2 and an error of 20%, along with an estimate on the equivalent sphere diameter D_e and a median cloud altitude, with accuracies of 30 μm and 300 m respectively (Jiménez et al. 2007).

Fig. 4.9 shows the CIW retrieval performance as a function of CIW, for tropical and mid-latitude conditions (Buehler et al. 2007).

4.4.4 Precipitation

Rain is an intermittent phenomenon, highly variable in intensity, time, and space. Convective rain cells can have rain rates above 50 mm/h lasting a few minutes with characteristic sizes of a few square kilometres, whereas stratiform clouds are typically accompanied by rain rates below 1 mm/h, with life cycles of a few days, covering hundreds of square kilometres.

Precipitation retrievals over the ocean are mostly based on the emission measured at frequencies below 40 GHz (Wilheit et al. 1977; Prabhakara et al. 1992). Over land, the emission-based algorithms are no longer valid since, due to the high surface emissivities, there is no contrast between rain and no rain. However the scattering signal at 85.5 GHz has been used, for example by Spencer et al.

(1989) or Grody (1991), to estimate precipitation indirectly over ocean and land. The emission signal originates in the liquid lower part of the cloud and in the rain layer, whereas the scattering in the upper frozen part of the cloud reduces the emission. As a consequence, the amount of scattering can be an indirect measurement of precipitation, relying on the relationship between the presence of large ice particles in upper layers and the precipitation below. These algorithms are applicable over all surfaces, ocean, land, and mixed.

Channels below 40 GHz are the most sensitive to rain, but are also affected by other parameters such as water vapour, clouds, and surface characteristics. In addition, they suffer from poor spatial resolution. On the other hand, higher frequencies offer spatial resolution in better agreement with the small-scale structure of rain cells, but are mostly sensitive to cloud ice.

The first rain retrieval methods were simple regressions between surface rain rates and their corresponding simulated or measured brightness temperatures (Wilheit et al. 1977). These approaches are still used to generate long-term climatology. Nevertheless the highly non-linear character of the radiative transfer function that links rain and brightness temperatures is a natural limit for such methods. Other algorithms rely on the fact that the space of the possible solutions is limited and can be described by a number of well-documented situations in a database. Retrievals from Kummerow et al. (1996; 2001), Bauer (2001) and Bauer et al. (2001) are all based on probabilistic techniques derived from Bayes theorem.

The performances of these retrievals depend heavily on the simulated database. On the basis of elaborate cloud microphysics obtained from cloud resolving models, radiative transfer calculations can be performed for detailed hydrometeor profiles, taking into account different hydrometeor phases and various size distributions (Smith et al. 1992b; Mugnai et al. 1993; Kummerow and Giglio 1994). The need for consistency between models and measurements has been stressed by Panegrossi et al. (1998) and Tassa et al. (2003). The cloud model and the associated radiative transfer calculations have to be able to explain and reproduce all the observed signatures.

Iterative techniques based on radiative transfer models have also been developed. The simplest one is a profile adjustment using a loop over a radiative transfer model (Kummerow et al. 1989). Unified ocean parameter retrieval algorithms use similar methodology and provide simultaneously near-surface wind speed over ocean, total water vapour, total cloud liquid water, and rain rate, with the advantage of limited correlation between the retrieved parameters (Wentz and Spencer 1998). Most of these algorithms were originally developed for retrieving rain over ocean but some of them also have an over-land module that relies on the scattering at 85 GHz by ice clouds above the rain. Elaborate variational assimilation schemes have also been tested (Moreau et al. 2003) and are currently implemented at ECMWF.

To overcome the sampling problem due to the low-level orbits of the current IR geostationary measurements, they have been combined with microwave observations from low orbits: the microwave rain retrieval is used as a reference and the IR

images provide the almost continuous measurement required to follow the evolution of the systems (Sorooshian et al. 2002; Tapiador et al. 2004). The Global Precipitation Climatology Project merges not only microwave and IR observations but also rain gauge data (Adler et al. 2003), to quantify the distribution of precipitation globally from 1979 to the present.

At millimetre and sub-millimetre wavelengths, the measurements are not expected to sense the rain directly, since the cloud opacity in the precipitating area is too large. Correlations between precipitation and brightness temperatures at millimetre waves are expected to arise from the relationship between the cloud, the particular atmospheric profile, and precipitation.

Rain rates have been estimated from AMSU-B observations over ocean and land from a simple differential scattering index in the clouds at 89 and 150 GHz (Ferraro et al. 2000), and an operational product from NOAA is available (Ferraro et al. 2005). These estimates are based on limited cloud model data and *in situ* precipitation measurements. In Staelin and Chen (2000), a neural network scheme is developed to retrieve precipitation rates from AMSU-A and B observations near 54 and 183 GHz, with a training database generated from collocated observations by AMSU and 3 GHz radar. The rms errors, evaluated for different rain-rate categories, are of the order of 50%.

A neural network methodology is also used by Defer et al. (2008), but trained on simulations derived from the coupling of mesoscale cloud models and radiative transfer calculations. The results are tested on AMSU-B observations collocated with radar measurements.

The differential response of the oxygen bands at 50–57 GHz and 118 GHz to the absorption and scattering by hydrometeors has also been suggested for estimating the rain rate (Bauer and Mugnai 2003), but has not yet been tested.

Observations of severe weather events require a high sampling rate. So far, microwave observations are only available from satellites in low orbits, with limited revisiting time. Geostationary orbits provide the adequate sampling but deploying microwave sensors in a geostationary orbit requires the use of millimetre and sub-millimetre radiometers to observe precipitation with an adequate spatial resolution while keeping a reasonable antenna size. The potential of millimetre and sub-millimetre observations for precipitation monitoring has been evaluated by Staelin and Surussavadee (2007), Surussavadee and Staelin (2008a; 2008b) and Defer et al. (2008), showing very good results for rain rates above 1 mm/h over both ocean and land. The GOMAS project was proposed to ESA with channels between 50 and 425 GHz and a 3 m antenna, providing a spatial resolution of 12 km at 380 GHz. Presently simulation studies and aircraft experiments are in progress.

The estimation of snowfall is a challenging problem, with the difficulty first to model accurately the scattering by snow and second to discriminate between the falling snow and the strongly variable emissivity of the snow on the ground. A physical approach has been tried by Kim et al. (2008) to retrieve snowfall rate over land using AMSU-B observations.

4.5 Applications of Microwave Data in Operational Meteorology

4.5.1 Data Assimilation

Data assimilation systems in Numerical Weather Prediction (NWP) provide the technical framework for performing atmospheric analyses that represent the best estimate of the state of the atmosphere at a certain time and that are used to initialise forecast models. Obviously, the quality of the forecast depends on both the accuracy of the model as well as the accuracy of the initial state estimate. The initial state estimate is called the analyses and represents an inversion problem. In general, this inversion is under-determined so that the analysis must employ information from *a priori* data (in NWP usually short-range forecasts initialised with previous analysis) and observations using a mathematical framework to combine optimally the two.

The complexity of the data assimilation system to be used depends on the application and the affordable computational cost and can range from simple interpolation schemes to four-dimensional variational and Ensemble Kalman filter schemes or even non-linear methods (Daley 1991). Global analysis systems are solving the above inversion problem with state vector dimensions of the order of 5×10^7 (the product of the number of grid points, number of levels and number of state variables) and observation vector dimensions of the order of 10^7 (product of number of observation points, number of levels and channels). This fact limits the use of non-linear models and ensemble-based methods, the latter usually being run at much lower resolution and with less detail than deterministic systems.

Most global operational NWP centres are operating efficient incremental four-dimensional variational (4D-Var) data assimilation systems that are based on the assumption that model behaviour is nearly linear in the vicinity of a good short-range forecast of the model state (Bouttier and Courtier 2002). The advantage of 4D-Var methods lies in the fact that they are dynamically consistent because the optimisation is performed over a time window through which the model is integrated, and that computationally efficient adjoint models can be used (Courtier et al. 1993). Systems like this are currently in use at ECMWF, the UK Met Office, Météo-France, the Meteorological Service of Canada (MSC), the Japan Meteorological Agency (JMA) (for the regional model) and in the US soon at the National Center for Environmental Prediction (NCEP).

4.5.2 Microwave Data in Operational Meteorology

Satellite data can be assimilated as level-1 (e.g. calibrated and located radiances), or level-2 (e.g. derived geophysical products) data. The choice depends on various factors, most prominently on the amount of maintenance required in an operational system. Level-2 products often employ a similar inversion framework to

retrieve parameters from radiances as is used in assimilation, namely *a priori* information, radiative transfer, error and bias models. If these ingredients are identical to those used in the level-1 data assimilation system, the result between assimilating level-1 or level-2 products should also be identical (Dee and Da Silva 2003).

However, most level-2 products employ different models and *a priori* constraints than used in NWP modelling and their characteristics are often not well defined or difficult to account for in data assimilations systems (Joiner and Dee 2000). The use of level-1 radiance data has advantages because (a) today's operational microwave radiative transfer models are very fast and quite accurate (Saunders et al. 1999), (b) it allows the flexible use of radiometer channels as a function of situation-dependent sensitivity and potential channel corruption, and greatly simplifies error and bias estimation.

In the early days of satellite data assimilation however, retrieved geophysical products were preferred due to less efficient models, more simple observation operators and the uncertain impact of satellite data in general. One of the earliest protagonists of microwave radiometer data in assimilation were Eyre et al. (1993) in Europe, producing retrieved temperature profiles from TOVS including the instruments, High-resolution Infrared Radiation Sounder (HIRS), Microwave Sounding Unit (MSU), and the Stratospheric Sounding Unit (SSU) data. The retrievals were obtained via a 1D-Var algorithm that also used the NWP model forecast as the *a priori* constraint. This approach was later extended to the use of moisture sensitive channels and instruments such as the AMSU-B and the SSM/I (Phalippou 1996). In all cases, the initial retrieval-based systems were replaced by direct radiance assimilation for the above-mentioned reasons (Andersson et al. 1994; Derber and Wu 1998).

The initial concerns over general satellite data impact were mostly overcome by the time 4D-Var data assimilation systems were established, mainly because of the improved treatment of spatial and temporal collocation between data and model trajectory and the interaction of temperature and moisture with model dynamics (Andersson and Thépaut 2008). Since then, data from passive microwave radiometers exploiting the 50–60 GHz oxygen absorption line complex for temperature sounding, and the 183.31 GHz water vapour absorption line for moisture sounding, have proven to be the most important satellite observing system in NWP. At the time of writing, these observations are supplied by AMSU-A, AMSU-B and the Microwave Humidity Sounder (MHS) onboard several NOAA satellites (15–19), Aqua and one METOP spacecraft. (METOP is a series of three satellites to be launched sequentially over 14 years, forming the space segment of EUMETSAT's Polar System (EPS) satellites.) This system is complemented by the so called microwave imagers (e.g. SSM/I, and the follow-on instruments Special Sensor Microwave Imager/Sounder (SSMIS), AMSR-E, TMI) that contribute information on sea-surface temperature, near-surface wind speed, integrated atmospheric moisture, clouds and precipitation.

Fig. 4.10 shows the temporal development of the observing system in the ECMWF 40-year reanalysis project ERA-40 (Uppala et al. 2004). Atmospheric

moisture and temperature analyses are largely constrained by MSU, SSU and later AMSU-A and SSM/I data. The strong positive impact of the improved observing system on the Television and IR Observation Satellite (TIROS) with the instruments TIROS Operational Vertical Sounder (TOVS) in 1979 and the Advanced TOVS (ATOVS) in 1998 on the analysis and forecasts is demonstrated by the much improved fit to surface pressure observations at weather stations and buoys (Fig. 4.10).

Apart from clear-sky microwave data, efforts towards cloud-affected data assimilation have been successful in recent years. This was mainly achieved by the greatly improved global model moist physical parameterisations and the enhanced computational capabilities that allow the operational employment of multiple scattering radiative transfer models (Bauer et al. 2006a). The explicit treatment of clouds and precipitation in operational analysis systems is accompanied by a large set of uncertainties. For example, greater model non-linearity, potential dynamic instabilities, large and unknown error structures as well as unknown model biases (Errico et al. 2007). However, several conservative methods have been implemented in operations, for example at ECMWF based on SSM/I data that provide significant and positive impact on both moisture analysis and forecasts (Bauer et al. 2006b; 2006c).

Another recent development in NWP is the use of microwave radiometer observations over land surfaces to constrain the soil moisture analysis. The research has been motivated by the planned ESA Soil Moisture and Ocean Salinity mission (SMOS) (launched in November 2009) that provides moderate resolution at 1.4 GHz from synthetic aperture imagery. Also channels near 6 and 10 GHz provide soil moisture information and is already available from TMI and AMSR-E.

4.5.3 Microwave Radiative Transfer Modelling in Data Assimilation

One of the most relevant issues is the trade-off between the accuracy of the forward radiative transfer model and its computational speed. The latter is optimised by the development of parameterised absorption models that produce regressions as a function of a selection of model predictors (e.g. temperature, humidity etc.) and that are trained with accurate line-by-line absorption models and representative atmospheric profile datasets (Matricardi et al. 2004). Their accuracy is usually better than radiometer noise for both IR and microwave.

Models such as Radiative Transfer for TOVS (RTTOV) are continuously maintained and improved by the NWP community, for example in the framework of RTTOV (by Numerical Weather Predication – Satellite Application Facility, NWP-SAF) or Community Radiative Transfer Model (CRTM) (by the Joint Center for Satellite Data Assimilation, JCSDA) models. On current super-computers, RTTOV produces about 40 forward calculations per millisecond.
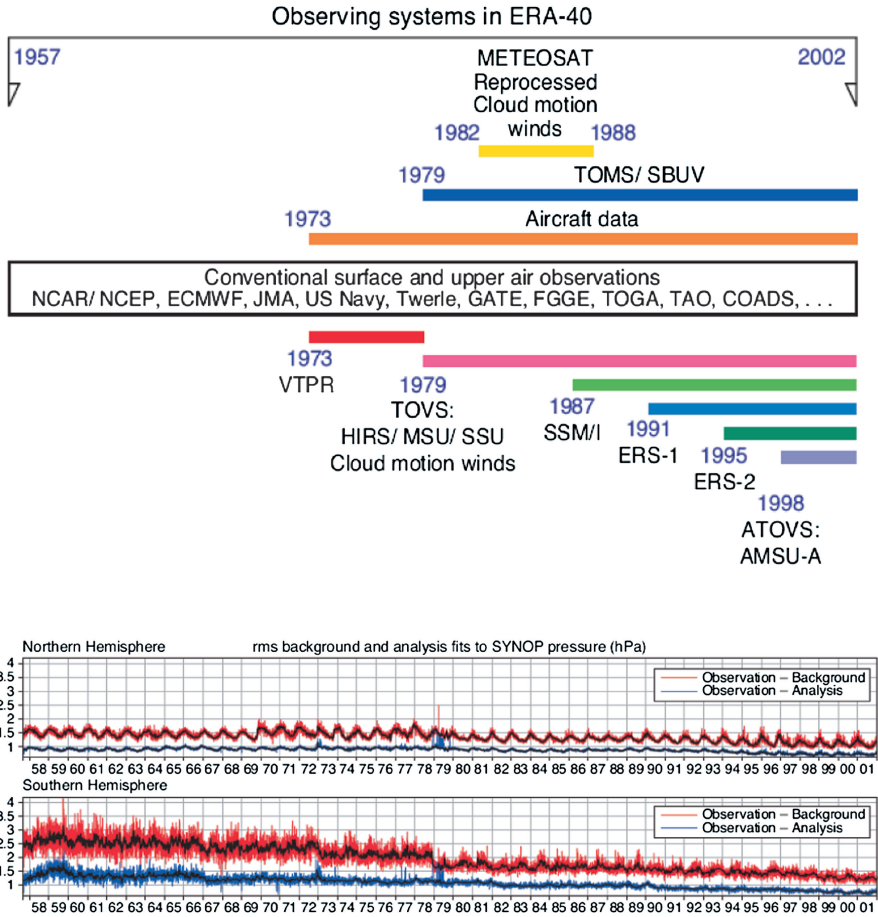
Fig. 4.10 Top: Development of the ERA-40 observing system between 1957 and 2002 with significant contributions from microwave data since 1979 (SSU, MSU), continued by AMSU-A since 1998 and SSM/I since 1987. Bottom: The rms of the background and analysis fits for ERA-40, background (daily (red) and 15-day moving average (black)) and analysis (daily (blue) and 15-day moving average (black)) fits to 00 UTC SYNOP (surface stations) and SHIP (ship observations) surface pressure observations (**a**) over the extratropical northern (upper) and (**b**) southern hemispheres (Uppala et al. 2004).

Note in this context that the temperature information used from AMSU-A observations originates from model-minus-observation departures of 0.1–0.3 K, which sets the target for modelling accuracy requirements. These requirements must be seen in the frame of a data assimilation system in which the short-range forecast of temperature, moisture and wind is already very accurate and where the information from the observations is significant only in relation to the short-range forecast accuracy. The precision is also a function of so called bias-correction

schemes (Auligné et al. 2007) that remove the systematic differences between model and observations.

The most apparent problems related to microwave radiative transfer modelling that are relevant for data assimilation in NWP are the simulation of surface emissivity, in particular over land surfaces, the modelling in the presence of clouds and precipitation, and more subtle phenomena such as the impact of the Zeeman line-splitting for channels sensitive to stratospheric layers and Faraday-rotation near 1.4 GHz. A good summary of the status of microwave radiative transfer modelling and all related issues is given by Mätzler (2006).

4.5.4   Impact of Remote Sensing Data on NWP

Data impact in NWP systems can be quantified in various ways by assessing the impact on both analysis and forecast. The latter assumes that better analysis will provide better initial conditions for forecasts. The most prominent impact assessment tool is the Observing System Experiment (OSE) in which new data is added to an existing system and the relative difference to a control system is evaluated. Similarly, individual data sources can be withdrawn from a full system (Andersson et al. 2004).

More sophisticated methods involve the model operators that are used in the data assimilation system. Based on forecast error estimates from the difference between forecasts and verifying analysis, the model and observation operator adjoints can be used to deduce the dependence of this forecast error on individual observation types (Tan et al. 2007) that were used in the initialising analysis (Zhu and Gelaro 2008). An alternative is the use of ensemble-based analysis and forecasting techniques that evaluate forecast impact as a function of ensemble spread with or without specific observation types. Lastly, the Observing System Simulation Experiments (OSSE) provides a framework for observations that do not yet exist and therefore require an observation simulation from independent NWP models (Arnold and Dey 1986).

In clear skies, the main objective for using microwave data in NWP is to constrain temperature and moisture distributions in the analysis. A major OSE impact study was conducted in 2006–2007 to evaluate the impact of the satellite observing system in global NWP at ECMWF (Kelly and Thépaut 2007). The experiments were performed with state-of-the-art modelling and data assimilation system of the time. Fig. 4.10 shows the comparative impact of the Aqua Advanced IR Sounder (AIRS) and the NOAA-16 AMSU-A/B instruments with reference to a baseline (all conventional observations), control (full operational observing system), and the baseline to which only Atmospheric Motion Vectors (AMV) were added. The plot shows the rms error of the forecast for the southern hemisphere (Fig. 4.11a) at 500 hPa geopotential height, a parameter, which is related to large-scale dynamic structures.
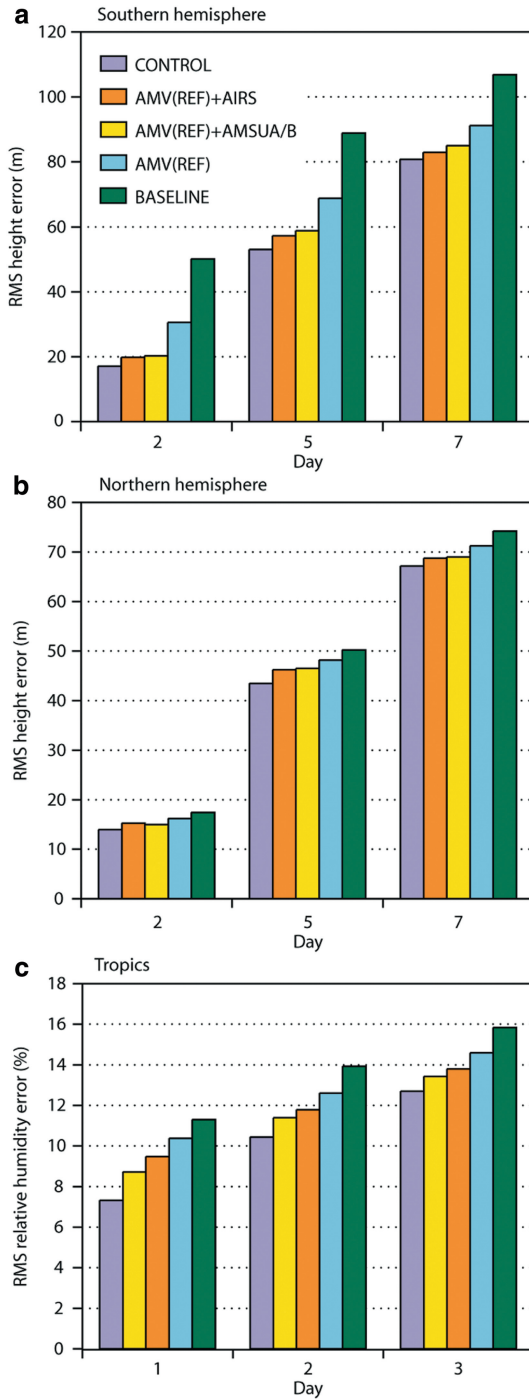
Fig. 4.11 The rms error in the forecast (forecast error) for 500 hPa geopotential height in the southern (**a**) and northern hemisphere (**b**) as well as relative humidity at 500 hPa in the tropics (**c**) from observing system experiments performed at ECMWF (see text for details).

The plot demonstrates that: (a) over the southern hemisphere with few conventional observations even AMV observations produce a significant improvement over the poor baseline configuration despite their limited accuracy and coverage, and (b) that the AMSU-A/B instrument combination produces a very similar relative impact compared to one advanced IR sounder well into the medium range.

The results are similar for the northern hemisphere (Fig. 4.11b) but with a smaller dynamic range due to the stronger constraint from more conventional observations obtained over the continents. Interestingly, the AMSU-A/B combination produces a stronger positive impact for relative humidity than AIRS in the tropics (Fig. 4.11c), mainly due to the weaker sensitivity to clouds. The latter is a significant driver of the valuable contribution of microwave instruments in global NWP.

Fig. 4.12 shows the results from similar OSEs that also include SSM/I observations both in clear and cloud/rain-affected situations. Here, the control and baseline experiments were set up as for Fig. 4.11 but SSM/I observations from two Defense Meteorological Satellite Program (DMSP) satellites (F-13 and 14) were added to a baseline that also contained observations from one AMSU-A instrument. This was necessary for adjusting the large-scale dynamic structures before constraining moisture fields with SSM/I observations.

The SSM/I OSEs tested the separate and combined impact of clear-sky and cloud affected data, both in addition to the baseline and by withdrawing the SSM/I data from the control experiment that contains all observations. The results clearly demonstrate that adding individual systems to a poor baseline always produces a much stronger impact than withdrawing them from a full observing system. This is the consequence of the complementary, and often redundant information provided by various instruments and instrument types. The impact of clear-sky SSM/I data is about as strong as that of cloud-affected data, a remarkable success given the difficulties associated with the assimilation of cloud-affected data mentioned earlier.
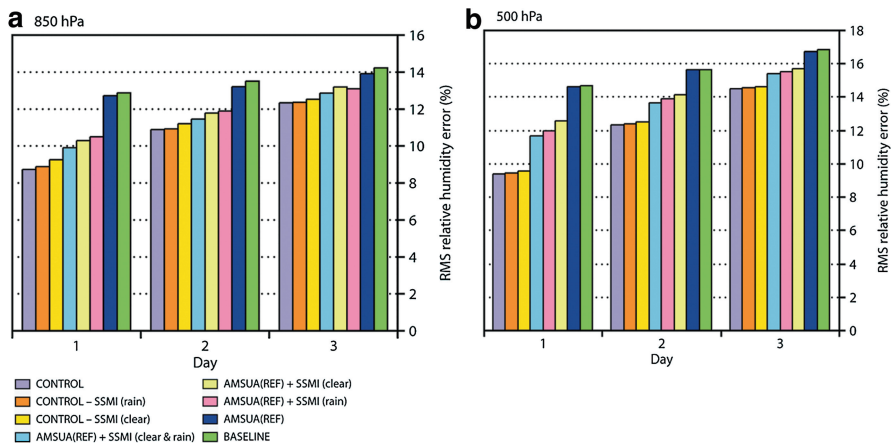

Fig. 4.12 The rms forecast errors for relative humidity at 850 hPa (**a**) and 500 hPa (**b**) in the tropics from SSM/I observing system experiments performed at ECMWF (see text for details).

The results from Kelly and Thépaut (2007) also confirm previous investigations that were dedicated to the assessment of those observing systems that contribute most to the humidity analysis. Andersson et al. (2007) concluded that SSM/I data has the strongest impact in the lower troposphere over oceans complemented by AMSU-B data in the mid and upper troposphere.

Fig. 4.13 shows a different measure of global analysis and forecast impact from selected observation types. Fig. 4.13a shows an example of the information content of rain-affected SSM/I observations in the ECMWF analysis (Cardinali et al. 2004).

The information content shows that a specific observation type contributes to the model analysis. Numbers are between 0 (the observation has no impact on the analysis) and 1 (only the observation determines the analysis). Large values of observation impact are produced along the ITCZ, SPCZ and other areas of significant precipitation occurrence in tropical and mid-latitude weather systems. This impact on the analysis is manifested in the forecast by a significant reduction of forecast errors (in terms of dry energy norm reduction (Zhu and Gelaro 2008), i.e. negative numbers/blue areas) with a similar geographical distribution (Fig. 4.13b).

The same metric of forecast error reduction was produced for selected observation types and for winter 2006/2007 (Fig. 4.13c). They indicate that AMSU-A represents the strongest system, i.e. the largest sensitivity of forecast error reduction (negative numbers) is obtained. This is from the combined effect of the impact of AMSU-A per observation and the large number of observations maintained in the system at that time (AMSU-A onboard NOAA-16/17/18, Aqua and METOP). Microwave observations related to humidity receive much less weight (SSM/I, AMSU-B), which is, to a large extent, explained by the fact that, in the current formulation, the forecast error term does not include the error contributions from atmospheric moisture. Fig. 4.13c shows that SSM/I data in both clear and cloud/rain-affected areas contribute to forecast error reduction. The differences between summer and winter seasons affect both magnitude and relative impact of observing systems (not shown).

4.5.5   Conclusions

Together with advanced IR sounders, microwave sounders and imagers represent the most important satellite observing systems currently available for NWP. These instruments mainly constrain temperature and moisture fields in the analysis, but are increasingly used in cloud and precipitation-affected areas in which IR observations only provide information on the atmosphere above clouds. These satellite observations are mostly assimilated as radiances due to the accuracy obtained with radiative transfer models – this even applies to a large degree to multiple scattering calculations. This conclusion is mainly valid for global modelling systems, but will increasingly be true for regional systems.
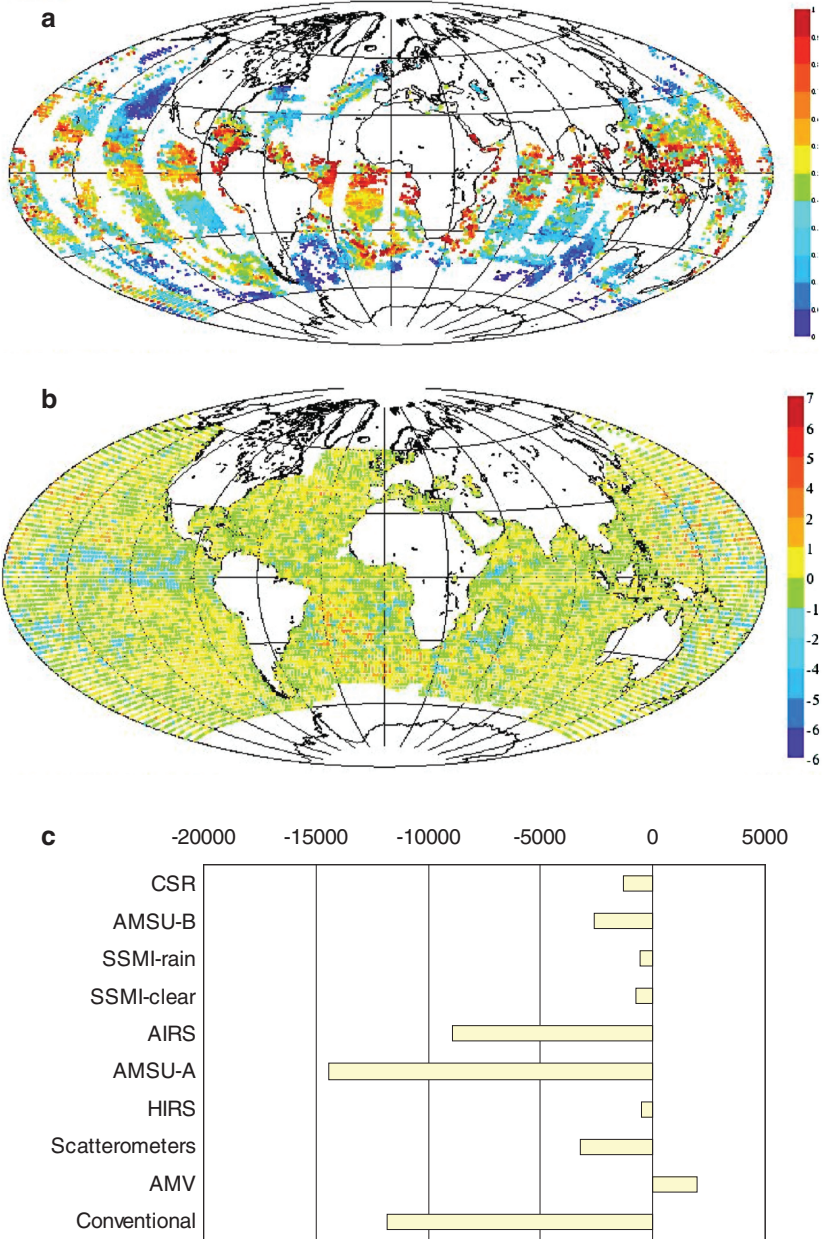
Fig. 4.13 (**a**) Information content of rain-affected SSM/I observations in ECMWF analysis; (**b**) 24-h forecast error sensitivity (dry energy norm in J/kg) to rain-affected SSM/I observations; and (**c**) accumulated sensitivity to all observation types for winter 2006/2007. Courtesy Carla Cardinali).

In the future, active microwave observations will deserve attention: currently Cloudsat radar and precipitation radar (PR) (e.g. TRMM PR see Section 4.7), serve mainly for validation but are expected to become part of the assimilated satellite data suite (Benedetti et al. 2005).

Currently, soil moisture is only analysed from near-surface temperature and humidity, but microwave observations have the potential to improve greatly on this situation through their sensitivity to top-soil water content as a function of land surface type, vegetation, soil moisture itself and observation frequency (Seuffert et al. 2003). Initial results using TMI data show both improved moisture analysis as well as impact on lower tropospheric moisture and clouds (Drusch 2007). Similar studies (Scipal et al. 2008) investigate the impact to be expected from soil moisture missions using existing scatterometers like METOP's Advanced SCATterometer (ASCAT).

4.6 Microwave Limb Sounding of the Troposphere

4.6.1 Background to Microwave Limb Sounding of the Troposphere

The use of limb sounding geometries for space-borne observations of atmospheric composition dates back to 1975 with the Limb Radiance Inversion Radiometer (LRIR) on NASA's Nimbus-6 and in 1978 with the Limb Infrared Monitor of the Stratosphere (LIMS) and Stratospheric and Mesospheric Sounder (SAMS) on Nimbus-7. Limb sounding – viewing the atmosphere "edge on" – offers significant advantages over nadir or near nadir sounding, particularly for atmospheric composition studies. Scanning an instrument's field of view across the Earth's limb brings a wealth of information on the vertical structure of the atmosphere, enabling observations with a higher resolution than is typical of nadir techniques. In addition, the longer viewing path lengths associated with limb sounding (200–500 km compared to *ca*. 20 km for nadir geometries) enhances the signature of trace gases in the observed spectra. However, these advantages typically come at the cost of poorer horizontal resolution than nadir-swath viewing instruments. In addition, limb sounding instruments typically require more precise optics and moving parts, and hence complexity, than nadir sounders using the same wavelength regions.

The microwave region of the electromagnetic spectrum is particularly attractive for limb sounding of atmospheric composition. This is because a wide variety of important atmospheric species are readily observable in the microwave where spectral lines are typically associated with rotational transitions, so that any molecule having a dipole moment is, in principle, observable. In addition microwave signals are unaffected by thin cirrus clouds or atmospheric aerosols that significantly hamper observations at shorter wavelengths, particularly when viewed in

limb geometry where the long path length reduces the probability of observing sufficiently cloud-free scenes. Thermal emission by the dry and moist air continua limits microwave limb sounding observations to altitudes above approximately 6 km, except in the extremely dry and cold conditions occasionally found in polar regions.

The millimetre-scale wavelength of microwave radiation observed has important implications for instrument design. In particular, the spatial resolution of microwave instruments is set by diffraction effects rather than being determined mainly by geometrical optics as at shorter wavelengths. The vertical width of a microwave limb sounder field of view is defined by the aperture size and wavelength. Increasing the aperture size proportionally decreases the width of the field-of-view (thus the total power received is invariant). For example, with the Aura Microwave Limb Sounder, the primary antenna length of 1.6 m gives a vertical field-of-view width at the limb of ~4.5 km at 190 GHz and ~1.5 km at 640 GHz.

Thermal emission and absorption lines are subject to both Doppler and pressure broadening, with pressure broadening dominating for microwave lines in the troposphere and stratosphere. Most spectral lines broaden by ~3 MHz/hPa, giving a typical linewidth of ~300 MHz to 1.5 GHz for signatures in the upper troposphere (100–500 hPa). This broadening, combined with increasing interest in remote sounding of tropospheric composition, has driven the development of wide bandwidth microwave observing systems and receivers for atmospheric science applications.

4.6.2   Previous, Existing and Planned Microwave Limb Sounding Instruments

The Microwave Limb Sounder (MLS) on NASA's Aura satellite is a successor to MLS on the Upper Atmosphere Research Satellite (UARS) (Barath et al. 1993), making observations in five spectral regions from 118 GHz to 2.5 THz (Waters et al. 2006), measuring more than 14 atmospheric species. Aura MLS's receiver and spectrometer bandwidths are appreciably increased over those of UARS MLS, allowing composition observations to extend into the upper troposphere (notably for O_3, CO and HNO_3), in addition to the established water vapour and cloud-ice observations.

In addition to the UARS and Aura MLS instruments, three other space-borne microwave limb sounding instruments have flown or are nearing launch. The Millimeterwave Atmospheric Sounder (MAS) (Croskey et al. 1992) was a component of the ATmospheric Laboratory for Application and Science (ATLAS) I, II and III missions flown by the NASA space shuttle in March 1992, March/April 1993 and November 1994. The Odin Sub-Millimeter Radiometer (ODIN-SMR) (Murtagh et al. 2002) is a four-band microwave instrument designed for limb sounding of stratospheric and mesospheric composition, and also measures water vapour and cloud ice in the upper troposphere. The Odin mission is notable in that

atmospheric viewing is time-shared with astronomical observations. The Japanese Experiment Module Superconducting Submillimeter-Wave Limb-Emission Sounder (JEM-SMILES) launched successfully in September 2009, and attached to the international space station, uses, for the first time in space, low-noise superconducting receivers to make high precision observations of stratospheric chemistry in tropical and mid-latitude regions.

4.6.3 Applications of Microwave Limb Sounding of the Troposphere

The upper troposphere is an important and somewhat poorly observed region of the atmosphere, with microwave limb sounding (notably from Aura MLS) providing one of the few high vertical resolution daily global satellite datasets. The upper troposphere is where both water vapour and ozone – two strong greenhouse gases – have their largest impact on Earth's radiative balance (Held and Soden 2000; Forster and Shine 1997). The processes that control stratospheric humidity, an important issue for polar stratospheric ozone loss, act in the tropopause transition layer (TTL), essentially the tropical upper troposphere and lowermost stratosphere. Intercontinental transport of air pollution in the upper troposphere, where winds are generally fastest, is an important and currently poorly modelled process affecting global and regional air quality (Stohl et al. 2002; Wang et al. 2006).

Most microwave limb sounding observations are based on spectrally-resolved observations of an individual line or line cluster. However, geophysical information can also be derived from measurements of absolute radiance. In particular, absolute radiance values in the 204 GHz "window" region of the spectrum, used in UARS MLS to measure stratospheric ClO, convey information on upper tropospheric humidity due to strong emission from the water vapour continuum. This information was used to provide the first daily global vertically-resolved observations of upper tropospheric humidity (UTH) from 465 to 147 hPa (Read et al. 1995; 2001). Later this information was combined with the 183 GHz observations of stratospheric water vapour (from 68 to 0.0046 hPa) (Pumphrey et al. 1998) to produce a merged dataset covering the entire TTL (Read et al. 2004a).

UARS MLS UTH data have been used in studies of climate-related phenomena such as El Niño (Chandra et al. 1998; Waters et al. 1999) and the Madden-Julian oscillation (MJO) (Madden and Julian 1971; 1994), see, for example, Stone et al. (1996), Mote et al. (2000) and Ziemke and Chandra (2003). The UARS MLS UTH observations also give needed new insight into the processes in the TTL that regulate the humidity of the stratosphere (Read et al. 2004b) and give rise to the so-called tape-recorder variation in stratospheric humidity (and other species as illustrated in Fig. 4.14, itself discovered in UARS MLS stratospheric H_2O data (Mote et al. 1995; 1996)).
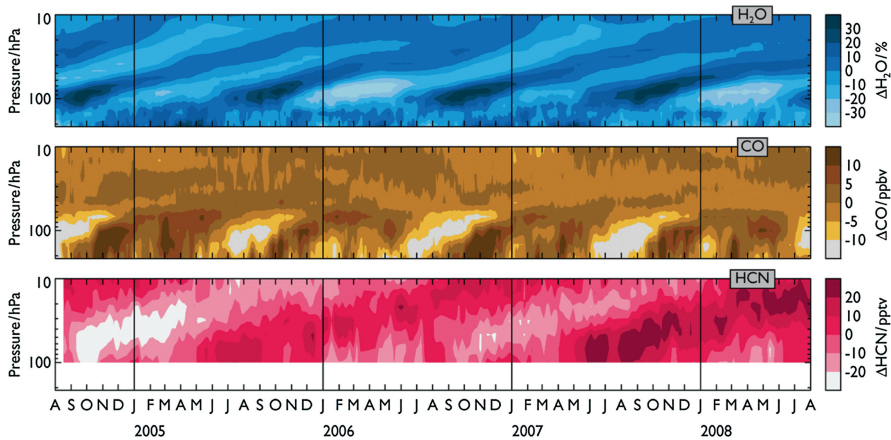
Fig. 4.14 Aura MLS observations of (top) water vapour, (middle) CO, and (bottom) HCN anomalies (differences from long-term mean). All these species show "tape recorder" signatures, with rising bands of alternately enhanced and reduced abundances. In the case of water vapour, as tropical air slowly rises from 12 km (where the bulk of convective outflow occurs) into the stratosphere it passes the "cold point" where it is freeze dried. The humidity of an air parcel thus reflects the coldest temperature it was exposed to. The annual cycle in the cold point temperature is thus recorded in the humidity of air, which subsequently rises in the tropical lower stratosphere. CO is a product of combustion both industrial and biomass related, the CO tape recorder signature reflects the annual cycle in CO emissions due mainly to biomass burning. The shorter chemical lifetime of CO in the stratosphere, compared to water vapour, leads to more rapid dissipation of the tape recorder signal in the vertical. HCN is mainly produced in forest fires. In the record shown, the HCN tape recorder seems to exhibit a two-yearly cycle rather than an annual cycle (Pumphrey et al. 2008), which probably reflects inter-annual variability in forest fires.

The Aura MLS instrument, having a broader measurement bandwidth than UARS MLS, is able to resolve spectrally the 183 GHz water vapour line with more than 3 GHz of instantaneous bandwidth. This enables Aura MLS observations of upper tropospheric humidity to be based on spectral contrast rather than absolute radiance measurement, providing contiguous data from one spectral region from the upper troposphere to the mesosphere (Read et al. 2007). The combination of these data with simultaneous MLS observations of atmospheric composition and cloud ice has provided new insights into important physical processes in the upper troposphere and lower stratosphere, as discussed below.

The UARS and Aura MLS instruments provided the first daily global observations of vertically resolved CIW in the upper troposphere. Scattering from large-particle ice clouds affects microwave limb radiances leading to radiance enhancement or suppression depending on the limb view angle. Initial observations from UARS MLS (Wu et al. 2005) indicated that deep convection was the dominant source of observed variability in relative humidity at 100 hPa. More recent CIW observations from Aura MLS (Wu et al. 2008) offer improved sensitivity and vertical registration, and some particle size information through observations covering a large frequency range.

Cloud processes, while critical to many aspects of weather and climate, are generally poorly captured in global models. Prior to the Aura MLS CIW observations, state-of-the art climate models exhibited differences by factors of *ca*. 20 in their estimates of CIW (compared to ~20% for parameters such as precipitation). This disagreement reflected the lack of global CIW observations available to constrain the model estimates. MLS CIW observations were used by ECMWF to justify changes to their cloud microphysics parameterisations, leading to improvements in their representation of tropical deep convection (Bougeault 2006, personal communication).

MLS observations of UTH and CIW have enabled us to make new quantifications of cloud and water vapour feedbacks on climate. Su et al. (2006) examined the relationship between sea surface temperature (SST) and MLS observations of UTH and upper tropospheric cloud ice (used as a measure of the strength of deep convection) overhead. The authors found a dramatic increase in the positive correlation of both UTH and cloud ice with SST for SSTs above 300K (see Fig. 4.15), and estimated that this accounted for ~65% of the previously-observed "super greenhouse effect".
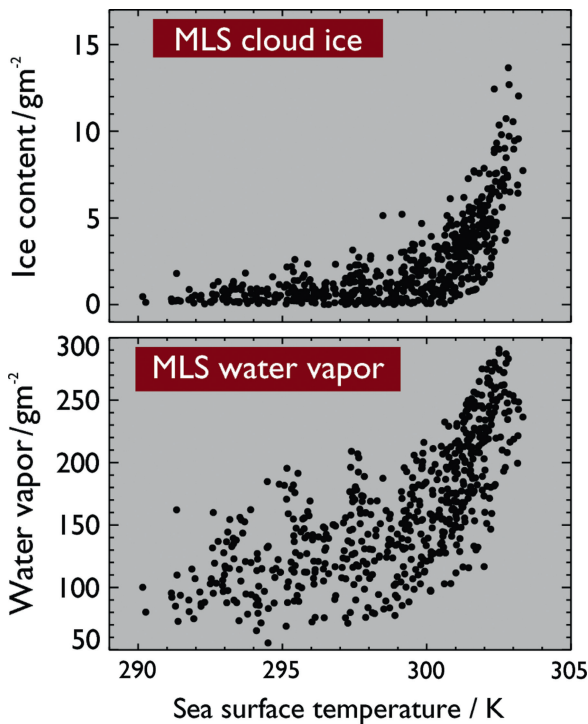

Fig. 4.15 Aura MLS observations of 215 hPa cloud ice (an indicator of deep convection) and water vapour correlated with underlying sea surface temperature (SST). Adapted from Su et al. (2006).

In addition to these data from Aura, similar humidity and cloud-ice datasets have recently been produced from Odin SMR (Eriksson et al. 2007; Ekström et al. 2007). Comparisons of the humidity observations with those from Aura MLS and the airborne measurements of ozone and water vapour by MOZAIC show agreement within 10% – better than the estimated accuracies of the instruments involved (Ekström et al. 2008). Comparisons of SMR cloud ice observations with CloudSat and Aura MLS indicate a common accuracy of 70% – sufficient for directing improvements to model parameterisations (Eriksson et al. 2008b).

4.6.4   Upper Tropospheric Composition and Chemistry

Although Odin-SMR stratospheric composition observations have been used in studies of tropospheric phenomena (Ricaud et al. 2007), the only direct observations of upper tropospheric composition for species other than water vapour, have been observations of O_3, CO and nitric acid, HNO_3 from Aura MLS (Filipiak et al. 2005; Livesey et al. 2008; Santee et al. 2007).
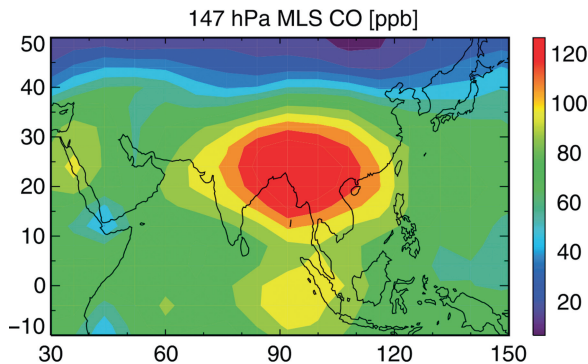

Fig. 4.16 Trapping of pollution in the upper troposphere by the anticyclone over the Asian monsoon region, as seen in 147 hPa observations of CO from the Aura Microwave Limb Sounder. Adapted from Li et al. (2005).

CO is a well established tracer of atmospheric pollution both from biomass burning and industrial sources (Stohl et al. 2002) and MLS upper tropospheric CO data show clear evidence of the trapping of pollution in the upper tropospheric anticyclone over the Asian monsoon region (Li et al. 2005) (see Fig. 4.16). MLS data also show a strong influence of convection on upper tropospheric CO abundance and long range transport (Jiang et al. 2007) (see Fig. 4.17 for an example). MLS CO observations in the upper troposphere and lower stratosphere have shown a strong "tape recorder" signature, as seen in water vapour (Schoeberl et al. 2006).

1-6 June 2006

13-18 September 2004

24-30 December 2006

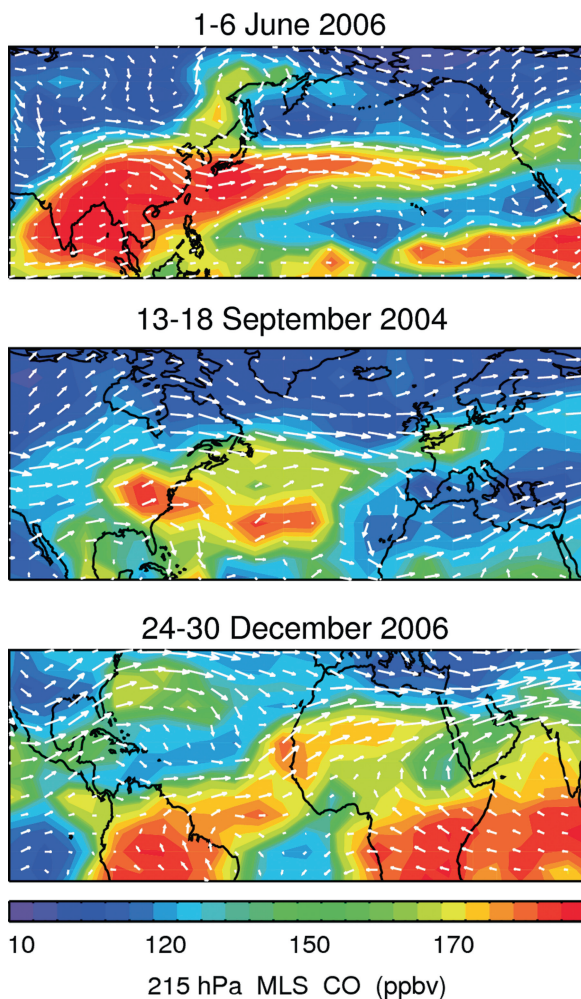10   120   150   170

215 hPa MLS CO (ppbv)

Fig. 4.17 Sample 5 day averages of Aura-MLS CO observations at 215 hPa, showing clear examples of long-range pollution transport in the upper troposphere. The arrows show winds from the GEOS-4 analysis.

The MLS observations of CO and H_2O together with other measurements have shown interesting insights into the processes that act in the TTL (Liu et al. 2007; Read et al. 2008).

MLS observations of O_3, CO and HNO_3 in the upper troposphere and lower stratosphere offer needed new insights into processes such as stratosphere/troposphere exchange that influence the abundance of tropospheric ozone and hence climate. Sample MLS observations of these species are shown in Fig. 4.18 at latitudes with ozone-poor air in the tropical upper troposphere. The "wave one"
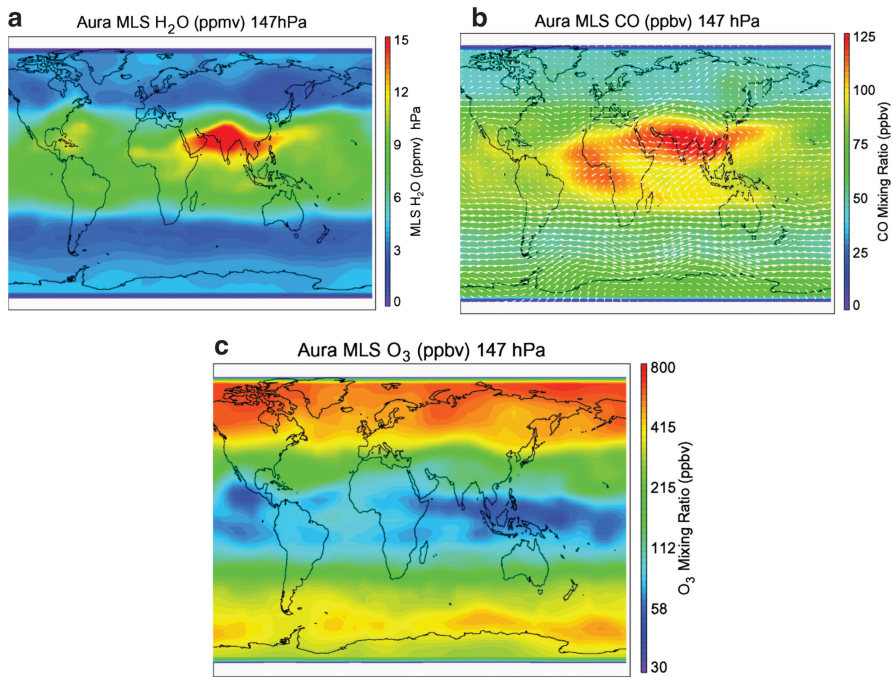
Fig. 4.18 Aura MLS observations of atmospheric composition at 147 hPa (~12 km). This pressure level is in the upper troposphere in the tropics and in the lower stratosphere at higher latitudes. (**a**) Water vapour, showing a clear distinction between the moist tropical upper troposphere and the arid lower stratosphere at higher latitudes. Meridional gradients follow the morphology of the tropopause (not shown). The signature of moist air from strong convection over the Indian subcontinent is clear. (**b**) CO, showing enhanced CO from convective vertical transport of polluted air over India, largely trapped by the anti-cyclonic circulations in this region, with some outflow over the Pacific. There are also indications of the transport of polluted air from the south east coast of the USA into the Atlantic Ocean. (**c**) O_3, showing the clear distinction between ozone-rich lower stratospheric air at mid- and high latitudes with ozone-poor air in the tropical upper troposphere. The "wave one" pattern in the tropics with low O_3 over the Pacific Ocean is a recurrent feature due, in part, to the convective transport of ozone-poor lower tropospheric air to these altitudes in this region.

pattern in the tropics with low O_3 over the Pacific Ocean is a recurrent feature, due in part to the convective transport of ozone-poor lower tropospheric air to these altitudes in this region.

4.6.5 *Conclusions*

The ability of microwave limb sounding techniques to retrieve tropospheric composition in all but the most cloudy of situations is an important tool for

quantifying critical processes in the upper troposphere. These processes include the long-range transport of air pollution, the influence of fast processes such as convection on tropospheric composition and hence radiative forcing, the influx of ozone-rich air from the stratosphere, and the transport of ozone depleting substances from the troposphere to the stratosphere. Observations from Aura MLS and Odin-SMR are providing needed new insights into these processes, however they lack the spatial and temporal resolution needed for full quantitative understanding.

The Stratosphere Troposphere Exchange And climate Monitor Radiometer (STEAM-R) is an instrument concept under development (led by the Odin-SMR team in Sweden) to make measurements in the upper troposphere and lower stratosphere with the improvements in vertical resolution needed to better quantify the processes listed above. STEAM-R uses a multi-beam array of fourteen 310– 360 GHz receivers simultaneously measuring from 5 to 28 km altitude with 1–2 km vertical resolution. Along-track spacing will be 30–50 km. STEAM-R measurement goals include O_3, CO, H_2O, nitric acid, HNO_3, nitrogen dioxide, N_2O, hydrogen cyanide, HCN, acetonitrile, CH_3CN, methyl chloride, CH_3Cl, chlorine monoxide, ClO and HDO. STEAM-R is a component of the Process Exploration through Measurements of IR and millimetre-wave Emitted Radiation (PREMIER) mission currently under consideration by the European Space Agency, and is intended to fly in a sun-synchronous low earth orbit, ideally in formation with meteorological missions such as METOP.

One of the most revolutionary advances in microwave techniques in recent years has been the development of Superconductor-Insulator-Superconductor (SIS) receivers. These offer a factor of *ca.* 30 improvement in signal-to-noise ratio (equivalent to a factor of about 1000 reduction in required integration time for a given signal to noise ratio). SIS technology has been deployed in ground-based and airborne astronomical and atmospheric applications for over 20 years, but it is only the recent development of space flight qualified coolers, capable of achieving the 4K temperatures required, that enable their use in orbit. The Japanese SMILES presently in orbit makes use of SIS technology.

A new SIS-based concept under development is the Scanning Microwave Limb Sounder (SMLS), which adds a horizontal scanning capability enabled by the dramatic reduction in needed integration time. SMLS can measure a ~65°-wide swath, equivalent to ~5,500 km width from an 830 km altitude orbit. SMLS observations would be spaced at ~50 × 50 km^2 in the horizontal. Such a swath observes 44% of the globe on every orbit. By choosing the appropriate orbital inclination, an SMLS instrument can make multiple measurements per day over large regions of the earth (see Fig. 4.19).
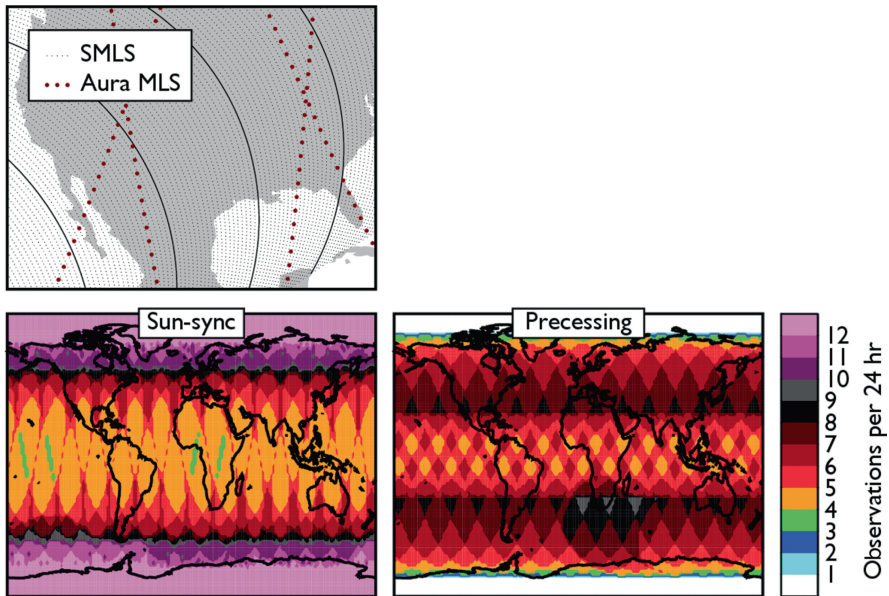
Fig. 4.19 (Top) SMLS observations (black dots) at 50×50 km^2 spacing for a single orbit, compared to Aura MLS observations for 24 h. Points in every 20th SMLS scan are connected for illustration. (Lower left and right) number of SMLS observations in 24 h for sun-synchronous and 52° inclined precessing orbits.

4.7   Active Techniques

4.7.1   Introduction

Two radar systems are currently flying in space. One is the Precipitation Radar (PR), which is part of TRMM, (see also Section 4.7.5). The second is the Cloud Profiling Radar (CPR) of the CloudSat mission, which observes both clouds and precipitation. These two radars are short-pulsed profiling radar systems that primarily measure the power backscattered by atmospheric targets (hydrometeors, such as ice crystals and cloud droplets) and any other target intercepted by the antenna beam (e.g. the Earth's surface). The target range for these systems is simply determined from the out-and-back time-of-travel of the pulse and, therefore, ranging by nadir viewing space-borne radars gives the altitude of the targets. The narrow antenna beam and the motion of the spacecraft resolve targets in the along-track direction.

The TRMM PR, launched in November 1997, transmits at 14 GHz and scans approximately 200 km across track. The CloudSat CPR, launched in April 2006, is

the first space-borne 94 GHz radar and is non-scanning, staring to Earth slightly offset from the nadir (0.16° off- geodetic nadir). The ESA EarthCare mission is to include a similar radar to CloudSat but with additional capabilities for providing Doppler motion measurements.

4.7.2   The CloudSat Radar

Cloud particles of a size typical of that measured in non-precipitating water and ice clouds are weak scatterers of microwave radiation. Data collected from cloud radars over many years reveal how the reflectivity of clouds varies over several orders of magnitude. The reflectivity factor ranges from below -30 dBZ[1], around the edges of the upper ice layers and low-level water clouds, to approximately 20 dBZ in heavier precipitation (Stephens et al. 2002). Low-level water clouds, in particular, are very dim targets and represent one of the main challenges for the current CloudSat mission. The reflectivity of the lower underlying Earth surface is much larger than that of clouds, typically 40 dBZ or greater, and varies as a function of surface type and condition, and can be influenced over land by vegetation, soil moisture, and snow depth for example, and surface wind speed over oceans. CloudSat is beginning to provide a wealth of new information about surface reflectivity.

The two-way attenuation of the radar pulse as it propagates through the atmosphere is not negligible at 94 GHz. This attenuation results from absorption by gases (chiefly water vapour), liquid water droplets, and precipitation sized particles (see Section 4.2). The dominant attenuation is from precipitation, which, if heavy enough, attenuates the CPR signal completely. Because of its magnitude, this attenuation by precipitation can be exploited to detect and estimate precipitation intensity.

Multiple scattering of radar pulses becomes an issue when space-borne radar footprints begin to exceed a kilometre, that is, become similar in size to the mean free path of microwave photons in hydrometeor suspensions. Through modelling and analysis, multiple scattering has been shown to affect interpretation of ranging of the CPR observations primarily for precipitation that exceeds about 5 mm/h (Haynes et al. 2008).

4.7.3   The CloudSat Mission

The CloudSat Mission was jointly developed by NASA, the JPL, the CSA, CSU, and the US Air Force. For CloudSat's CPR see Im et al. (2005). It is the first space-borne 94-GHz radar and provides unique information about the vertical cloud

---

[1]The different echo intensities (reflectivity) are measured in dBZ (decibels of Z, the amount of transmitted power returned to the radar receiver). The dBZ values increase as the strength of the signal returned to the radar increases.

profiles over the globe. The CPR instrument on CloudSat began operation in 2006 (Stephens et al. 2008). Since that time, CPR has been acquiring the first-ever continuous global time series of vertical cloud structures and vertical profiles of cloud liquid water and ice content, and precipitation incidence. The vertical resolution is 485 m and the spatial resolution is defined in terms of the antenna 3 dB footprint being 1.4 km. In order to take full advantage of observations by other types of space-borne atmospheric remote sensing instruments, the CloudSat spacecraft flies in formation as part of the Afternoon Constellation of satellites, the so called A-Train, (Stephens et al. 2002). In particular CloudSat flies in close formation within the Cloud-Aerosol Lidar and Infrared Pathfinder Satellite Observations (CALIPSO) (Winker et al. 2007), which carries a lidar system, so that their respective beams cover the same vertical column within about 15 s.

4.7.4 The Cloud Profiling Radar

The need to detect the weak cloud signals was the over-riding requirement on the CPR stated in terms of a minimum detectable cloud reflectivity Z_{min} approximately -28 dBZ at beginning of life. This requirement then dictated the frequency of operation of the radar and related technologies. This minimum sensitivity represents a sensitivity almost five orders of magnitude greater than the TRMM PR.

The CPR provides profiles of atmospheric hydrometeors. The quantity of immediate relevance to these profiles is the range-resolved radar cross-section per unit volume, η, at a specific range r defined as:

$$\eta = \frac{P_{rec}(4\pi)^3 r^2 L_a}{P_t \lambda^2 G_{rec} G^2 \Omega \Delta} \tag{4.4}$$

where P_{rec} is the output power of the receiver, P_t is the transmitted power, λ is the wavelength, G_{rec} is the receiver gain, G is the antenna gain, r is the range to the atmospheric target, Ω is the integral of the normalized two-way antenna pattern, Δ is the integral of the received waveform shape, and L_a is the two-way atmospheric loss. The quantity η is converted to the equivalent (attenuated) range-resolved reflectivity factor:

$$Z_e = \eta \frac{\lambda^4 10^{18}}{\pi^5 |K_w|^2} \tag{4.5}$$

where $|K_W|$ is set to 0.75, representative for water at $10°$C at approximately 90 GHz.

Absolute calibration of the radar requires precise knowledge of the various parameters in Eq. 4.4 above. Pre-launch calibration parameters were obtained either directly from laboratory measurements or by analysis of experimental data. In orbit,

the transmit power P_t. and receiver gain G_{rec} are routinely measured via internal calibration channels of the radar. Both have remained remarkably stable since launch. End-to-end system calibration is also evaluated using measured backscatter off the ocean surface. The method relies on measuring the backscatter off the ocean surface at an angle at which the sensitivity to wind is minimal. Over the 12 months between August 2006 and August 2007, the CloudSat spacecraft performed several calibration manoeuvres over pre-selected cloud-free oceanic areas and verified that the absolute calibration of the CPR is well within the required 2 dB requirement (Tanelli et al. 2008).

The in-orbit performance of the radar has also been independently verified by comparison with radar measurements obtained from several airborne programs since launch, matched in volume specifically to the space-borne radar observations. Analysis shows the reflectivity of the space-borne and airborne radars agree within 2 dB except in the region of heavy precipitation where multiple scattering in the CloudSat footprint becomes an issue.

Z_{min} is an important instrument design parameter. This minimum factor is defined as the cloud reflectivity factor Z_e, which, after averaging and noise subtraction, yields a power equal to the noise power standard deviation. Z_{min} is therefore determined by the equivalent noise floor and by the number of transmitted pulses. The noise floor ultimately depends on the radiometric temperature of the observed scene at 94 GHz. Based on the current calibration, the minimum detectable reflectivity ranges from −29.9 dBZ to −30.9 dBZ. Seasonal changes in temperature, land cover, and sea ice affect the distribution of Z_{min}.

The first images from CloudSat (Fig. 4.20) presents the historic first-look CPR image of the vertical structure of a warm front over the North Atlantic observed on 20th May 2006.

This image was acquired immediately after activation of CPR as part of a brief 4-h checkout test. The richness of the CloudSat information for studying these classic weather systems has since been highlighted by Posselt et al. (2008). These initial test data were transmitted in near real time and near-real time data are currently being exploited in a number of operational applications described elsewhere (Mitrescu et al. 2008).

4.7.5 The Tropical Rainfall Measurement Mission

Within the Mission to Planet Earth program (MTPE) (Simpson et al. 1988) TRMM was developed in a collaborative effort between NASA and the Japanese National Space Development Agency (NASDA) - now the Japan Aerospace Exploration Agency (JAXA) (Simpson et al. 1996; Kummerow et al. 2000; http://trmm.gsfc.nasa.gov/). The TRMM research program is dedicated to measuring tropical-subtropical rainfall over a long time period (measurements are now in their 12th year), to collect the first representative and consistent ocean climatology of precipitation and latent heating. The TRMM satellite was initially launched into a
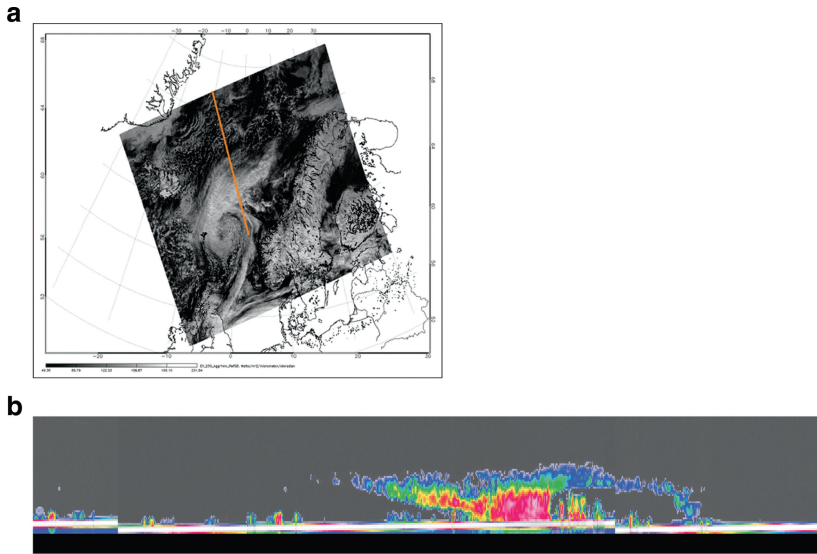
Fig. 4.20 A MODIS image (upper) of a warm frontal system intersected by CloudSat along the orbit track. The first quick-look image of CPR reflectivity gathered for an approximate 1,400 km section of orbit on 20th May 2006 is shown in the lower panel captured immediately after the first turn on of the CPR. The height of the image represents 30 km. (from Stephens et al. 2008).

low-altitude (350 km), non-sun-synchronous orbit inclined 35° to the Earth's equatorial plane, with a nominal mission lifetime of three years. During August 2001, the TRMM orbit altitude was boosted to 400 km in order to lower drag and reduce fuel consumption. The TRMM satellite is expected to remain operational until 2012/2013, at which time it will no longer have sufficient fuel for station keeping. The satellite measures precipitation over tropical latitudes, the coverage extends from 35°S to 35°N, which includes the sub-tropical zones. The tropical-sub-tropical regions are important because more than two thirds of global rainfall occurs there, while precipitation-induced latent heating strongly controls the large-scale general circulation, and various seasonal/intra-seasonal modulated synoptic scale and mesoscale weather disturbances.

TRMM carried a precipitation radar (PR) using a through-nadir scanning, non-coherent, 2×2 m^2 slotted wave-guide-phased array antenna providing a ~220 km swath width. The radar system operates at 13.8 GHz, and is capable of generating near real time 3-D pictures of rain rate with a calibration accuracy of ~0.5 dBZ. The radar was developed by NASDA's partner agency in Japan, NiCT. Its design and capabilities have been described in Okamoto et al. (1988), Meneghini and Kozu (1990), Nakamura et al. (1990), Okamoto and Kozu (1993), Kozu et al. (2001), Okamoto (2003) and Okamoto and Shige (2008).

The TRMM satellite also carries the TRMM microwave imager (TMI). This is a conical-scanning radiometer with a swath width of ~760 km, 9 channels at 10.7 GHz, 19 GHZ, 21.3 GHz, 37 GHz and 89 GHz, all channels are dual polarized

vertical and horizontal with the exception of the vertical polarized water vapour channel at 21.3 GHz. All channels make use of the same 0.6 m diameter antenna. The TMI has been described by Kummerow et al. (1998; 2000), Smith and Hollis (2003), and Fiorino and Smith (2006). The TMI measurements allow estimates of rain rates to be made because of a well known relationship between the microphysical properties of rain and the up welling microwave radiation. The various frequencies are important for obtaining information at different vertical levels of the atmosphere. The swath width of the TMI is three times greater than the PR (~780 vs. ~220 km) and enables the TMI to measure precipitation over a wide area with a high duty cycle. The PR measures the detailed physics of precipitation along the narrow radar track at the centre of the radiometer track. The combined radar-radiometer algorithms have become the most accurate of the TRMM data analysis (Smith et al. 1995a).

Three additional instruments on the TRMM satellite are used to study precipitation indirectly, these are: (a) the 5-channel Visible and InfraRed Scanner (VIRS), (b) the Lightning Imaging Sensor (LIS), and (c) the prototype Cloud and Earth's Radiant Energy System (CERES), see Kummerow et al. (1998) for details.

4.7.6 Results from TRMM

The TRMM project is very successful in providing high quality geophysical parameters at levels 2 and 3 based on data collected by the different instruments. The L2 algorithm produces instantaneous rain rates at full spatial resolution (i.e. at the resolution of either the radar beam or a mean convolved radiometer beam) while the L3 algorithms produces monthly-averaged rain rates at $5 \times 5°$ spatial resolution.

Fig. 4.21 compares monthly-averaged rain maps over ocean from the most recent algorithm versions. The maps show close agreement between four greatly different retrieval approaches: (a) L2 TMI only, (b) L2 PR only, (c) L2 TMI and PR combined, and (d) L3 TMI only.

Some key characteristics of the algorithms used are given below. The 2a12 TMI-only rain rate profile algorithm combines a mesoscale cloud resolving model (CRM) with a microwave radiative transfer model (Mugnai and Smith 1984; 1988; Mugnai et al. 1990; 1993; Smith and Mugnai 1988; 1989; Smith et al. 1992a; 1992b; Marzano et al. 1999; Di Michele et al. 2003). Kummerow et al. (1996) adopted this strategy making use of a large number of microphysical profiles of the Goddard cumulus ensemble model (GCE) (Tao and Simpson 1993; Simpson and Tao 1993), and the University of Wisconsin nonhydrostatic modelling system (UW-NMS) (Tripoli 1992), to establish a set of profiles, which forms a probability density function of rainfall.

The current 2a12 algorithm uses a CRD which is calculated by linking microwave radiative transfer calculations to a large set of simulated microphysical profiles i.e. pairs of CRM-generated microphysical profiles together with corresponding synthetic top-of-atmosphere microwave brightness temperatures. This approach requires that the CRD of possible cloud-precipitation structures is well

Fig. 4.21 Distributions of monthly rainfall accumulations over tropical oceans for February 1998 produced by most recent versions (V6) of standard TRMM L2 and L3 algorithms. (**a**) shows TMI-only (L2 algorithm 2a12), (Kummerow et al. 1996, 2001; Olson et al. 2001, 2006), (**b**) shows PR-only (L2 algorithm 2a25), (Iguchi et al. 2000; Meneghini et al. 2000; Iguchi 2007), (**c**) shows PR-TMI Combined (L2 algorithm 2b31), (Haddad et al. 1997; Smith et al. 1997), while (**d**) shows TMI-only (L3 algorithm 3a11), (Wilheit et al. 1991a; 1991b; Hong et al. 1997; Tesmer and Wilheit 1998). Colour bar denotes average rain rate in mm/day.

populated, if this is not the case, an iterative variational relaxation technique is more appropriate such as described in Smith et al. (1994a; 1994b; 1995b).

The 2a12 algorithm's greatest strength is that it is an attenuation type solution, i.e. the relationship between radiance (or brightness) temperatures and drop size goes according to D^4 with D the diameter of a spherical droplet instead of the radar backscatter D^6 dependence. This reduces the sensitivity of the retrieved rain rates to the drop size distribution. A weakness is the low spatial resolution of the TMI compared to the PR, which means the retrievals contain greater uncertainty due to beam filling effects, Panegrossi et al. (1998) and Mugnai et al. (2008) have described different ways to mitigate the latter problem.

The 2a25 PR-only L2 rain rate profile algorithm is a hybrid method described by Iguchi et al. (2000), Meneghini et al. (2000) and Iguchi (2007), based on earlier work by Iguchi and Meneghini (1994). The algorithm uses the radar reflectivity vector (Z) to produce a vertical profile of rain. However, in order to get accurate results, it is essential that the path integrated attenuation (PIA) is known. To achieve this, a Hitschfeld-Bordan solution (Hitschfeld and Bordan 1954) is used in a first step to accumulate attenuation in a top-down sequence, followed by application of what is called the surface reference technique (SRT), which provides a correction of the retrieved vertical rain rate vector according to the difference between the Hitschfeld-Bordan PIA and the SRT-derived PIA (Meneghini et al. 1983). For the SRT, the surface return from a rain-filled path is compared to that from a climatological rain-free path created by combining all prior cloud-free pixels over the mission life into a background climatology.

The strength of the 2a25 algorithm is the use of range-gated returns, which results in a well resolved vertical structure. The greatest weakness in using the SRT scheme is the assumption that the differences between two surface returns are caused only by atmospheric path attenuation, and are not due to different surface conditions. In reality, surface reflectivity depends on the roughness of the surface due to wind and internal waves over ocean, and seasonally varying surface properties over land. The greatest error source is the strong dependence of the backscatter on the diameter of the drops, proportional to D^6, and thus is very sensitive to the drop size distribution. Two additional error sources are the sensitivity to residual systematic errors in the PR calibration, and severe attenuation due to high rain rates.

The 2b31 algorithm uses PR and TMI measurements simultaneously. Such a technique is referred to as a "tall vector" algorithm (Farrar 1997); an example is the algorithm to analyse SSM/I data by Smith et al. (1994b) based on hydrometeor profiles from the University of Wisconsin nonhydrostatic modelling system (UW-NMS). Haddad et al. (1997) and Smith et al. (1997) formulate an algorithm based on the design of algorithm 2a25, but use Bayesian probabilities to retrieve the rain rate profile. As with algorithm 2a25, 2b31 first uses the SRT to constrain the Hitschfeld-Bordan solution but then uses the 10.7, 19, and 37 GHz TMI brightness temperatures to estimate the PIA at 13.8 GHz, thus providing a second PIA constraint beyond the SRT. The main weaknesses of this approach are its sensitivity

to any residual calibration offset in the PR measurements, and inconsistencies between the radiative transfer model for the passive and active sensors. Farrar (1997) is using a combined Radiative transfer model to overcome this problem. Thus, this type of algorithm shares the strengths of both the 2a25 and 2a12 algorithms.

4.7.7 Conclusions

Since becoming operational, the CloudSat CPR has provided unique, global views of the vertical structure of clouds and precipitation. These new observations have provided the first real estimates of the ice contents of clouds, the direct effects of clouds on radiative heating and how fast and how often clouds produce rainfall (Stephens et al. 2008). The observations have also revealed new knowledge about occurrence and properties of high latitude cloudiness by demonstrating quantitatively the important role of reduced Arctic cloudiness during the 2007 summer to the sea ice loss that occurred (Kay et al. 2008).

The planned aerosol-cloud experiment mission (ACE) will consist of one or more satellites in a LEO, in which the overall science payload is dedicated to obtaining aerosol and cloud profiles for climate and water cycle research. The ACE payload includes a dual-frequency near 13 and 90 GHz (Ka/W-band) Doppler radar designed so that the Ka-band radar scans and the W-band radar acquires multiple beams across-track, enabling vertical profiling of the precipitation rate across a large dynamic range (from very light to heavy), to obtain information on the drop size distribution, to measure the vertical motion, and to determine latent heating (from knowledge of vertical motion profile and thus vertical derivative of horizontal divergence). Finally the optional polarization diversity will give extra information concerning precipitation phase, liquid, frozen, mixed, and melting ice.

The PR/TMI instruments on TRMM have produced new results of vertical structure of precipitation and collected unique data of clouds, convection, frontal zones, precipitating storms, and tropical cyclones. NASA and JAXA are now planning the Global Precipitation Measurement Mission (GPM) (Smith et al. 2007; Mugnai et al. 2007; http://gpm.gsfc.nasa.gov/).

For nearly continuous observations of precipitation at mid- and low-latitudes, the next generation weather radar (NEXRAD) in Space (NIS) consists of a satellite in a GEO carrying a Doppler Ka-band radar used for tropical cyclone monitoring over a ~48° (~5,300 km) diameter great circle disk. The radar design allows for continuous storm pointing enabling rapid-updated storm observations, as frequent as every 15 min at a moderate resolution of ~12 km. The main scientific goal of this mission is to provide a continuous data stream for operational tropical cyclone prediction, as demonstrated through the observing system simulation experiments (OSSE).

4.8 Measuring Atmospheric Parameters Using the Global Positioning System

GPS satellites transmit signals at two microwave frequencies, L1 = 1.57542 GHz and L2 = 1.2276 GHz. The signals are used primarily for precise positioning and navigation, but they can also be used to probe the atmosphere, and this has led to the relatively new field of GPS meteorology. GPS meteorology is concerned with measuring how the Earth's atmosphere affects the propagation of the GPS signals, and then deriving atmospheric state information from these measurements. The atmosphere affects the GPS signal propagation in two ways: firstly the velocity of the signal is reduced because the refractive index of the atmosphere is greater than unity and secondly the ray paths are curved as a result of gradients in the refractive index.

There are two quite distinct GPS measurement types which have very different information content. GPS radio occultation measurements have a satellite-to-satellite, limb geometry and they provide profile information with good vertical resolution properties. In contrast, ground-based GPS measurements have a satellite-to-ground geometry and they primarily give column integrated water-vapour information.

4.8.1 GPS Radio Occultation

The methodology of radio occultation measurements was pioneered by planetary scientists in the 1960s and it formed part of NASA's Mariner 3 and 4 missions to Mars. During the 1980s it was realised that these techniques could be applied to measuring the Earth's atmosphere using the GPS signals. A detailed description of GPS radio occultation (GPSRO) and its error characteristics can be found in Kursinski et al. (1997). The geometry of the measurement is illustrated in Fig. 4.22. A radio signal is transmitted by a GPS satellite, passes through the atmosphere and is measured with a GPS receiver placed on a satellite in LEO. The ray path between the satellites is bent as a result of gradients in the refractive index of the atmosphere, which in turn can be related to gradients in the temperature and humidity.

The bending angle, α, is not measured directly. Given estimates of the satellite locations and velocities, α can be derived from the time derivative of the additional time delay for the radio signal to propagate between the satellites caused by the atmosphere. The motion of the LEO satellite enables the variation of α as a function of the impact parameter, a, to be determined. Bending angles are derived for both the L1 and L2 GPS signals, and this enables the ionospheric bending contribution to be corrected because the ionosphere is dispersive at these frequencies. The ionosphere-corrected bending angle profile can then be inverted with an Abel transform to provide a vertical profile of refractive index. Temperature and humidity information can be derived from the bending angle or refractive index profiles.
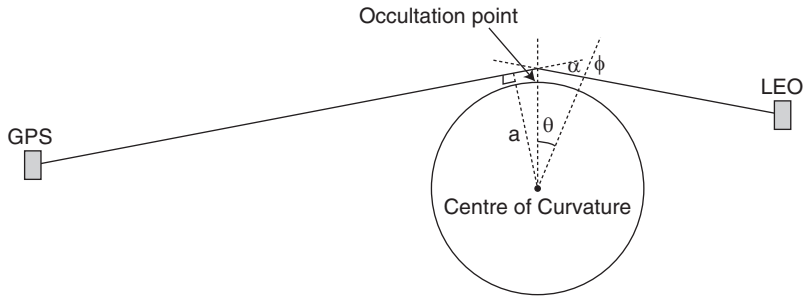
Fig. 4.22 The geometry of the GPSRO measurement technique.

The proof-of-concept was demonstrated in 1995 with the GPS/MET experiment. This showed that the temperature profiles derived from GPSRO measurements were of sub-Kelvin accuracy for heights between 7 km and 25 km (Kursinski et al. 1996; Rocken et al. 1997), despite using a sub-optimal temperature retrieval technique.

4.8.2   Data Availability and Impact

The success of the GPS/MET mission led to a number of missions of opportunity, most notably the Challenging Mini-satellite Payload (CHAMP) (Wickert et al. 2001). This was followed by the Constellation Observing System for Meteorology Ionosphere and Climate (COSMIC) of six receivers (Anthes et al. 2008) and then the Global Navigation Satellite System Receiver for Atmospheric Sounding (GRAS) on METOP-A, which is the first fully operational GPSRO mission (Luntama et al. 2008).

Currently, the COSMIC constellation and GRAS provide around 2000 and 650 profiles per day respectively, distributed globally. Each profile contains between 250 and 300 bending angles, spanning the vertical interval from the surface up to 60 km. To put these numbers in context, ECMWF currently assimilates around 10 million observations per 12 h assimilation window, of which ~90% are radiance measurements. The number of COSMIC and GRAS bending angles actively assimilated account for less than 3% of the total.

Despite the relatively low data numbers, GPSRO measurements are valuable in NWP because their information content complements that provided by satellite radiance measurements. GPSRO measurements have good vertical resolution, an all-weather capability and can be assimilated over both land and sea. Furthermore, they can be assimilated without bias correction. This measurement characteristic is particularly important because it means that the data help to distinguish between model and observation biases, and they provide anchor-points to prevent model drift in adaptive bias correction schemes (Dee 2005). Assimilation without bias correction is possible because the fundamental GPSRO measurement is a time-delay with an atomic clock, and the forward problem is relatively simple to model when compared to the radiative transfer problem.

The GPSRO errors are smallest in a fractional sense in the height interval from 8 to 30 km, and this is where their information content is greatest (Collard and Healy 2003). Theoretical information content studies show that GPSRO measurements contain primarily humidity information in the lower troposphere and temperature information in the upper troposphere and stratosphere. In addition GPSRO measurements potentially provide surface pressure information. This arises because the measurements are assimilated as a function of a height coordinate-ordinate, meaning that the hydrostatic integration is part of the observation operator.

Most operational NWP centres currently assimilate either vertical profiles of bending angle or refractivity, using one-dimensional observation operators. These approaches ignore the two-dimensional, limb geometry of the observation which introduces additional forward model errors, but research into more advanced operators is ongoing (Sokolovskiy et al. 2005; Healy et al. 2007). Observing system experiments at a number of NWP centres have demonstrated that GPSRO measurements provide extremely good temperature information in the upper troposphere and lower stratosphere, confirming the theoretical information content studies (Healy and Thépaut 2006; Cucurull et al. 2007; Aparicio and Deblonde 2008; Poli et al. 2009).

In most cases, the measurements have clearly improved stratospheric analysis and forecast biases with respect to radio-sonde temperature measurements. The measurements have also corrected systematic errors that are in the null space of the radiance measurements as a result of the superior vertical resolution. Furthermore, experiments have demonstrated that the GPSRO measurements have an impact on the bias corrections applied to AMSU-A channels 8, 9, 10 and 11 radiances, generally resulting in an improvement in the fit to radio-sonde measurements.

To date, it has proved more difficult to show any significant impact on the lower tropospheric humidity forecasts, and it is clear that the humidity analysis is being driven by other measurements. This may be because the weight given to the GPSRO observations in the lower troposphere is too low, but the observation processing and forward model errors are certainly larger in this region. Some improvement might be expected with the introduction of two-dimensional observation operators, and data processing techniques in the lower troposphere are continually evolving and improving (Jensen et al. 2003).

GPSRO measurements are now being assimilated in reanalyses. Fig. 4.23 shows the impact of introducing COSMIC measurements in the ECMWF ERA-Interim project on the analyses and short-range forecasts departure statistics for radio-sonde temperature measurements at 100 hPa in the northern and southern hemispheres. The COSMIC measurements are assimilated from 12th December 2006, and there is a clear improvement in the biases from this period with a shift in the bias of order 0.1 K and 0.2 K in the northern and southern hemispheres, respectively.

One outstanding issue that must be addressed in the context of planning future GPSRO missions is the optimum size (number) of the constellation of LEO receivers. There is no indication that the current number of receivers is anywhere near the saturation point, where adding more receivers provide no additional benefit, so the current number probably represents a lower limit. However, estimating the number of receivers where saturation may occur is a challenging problem,
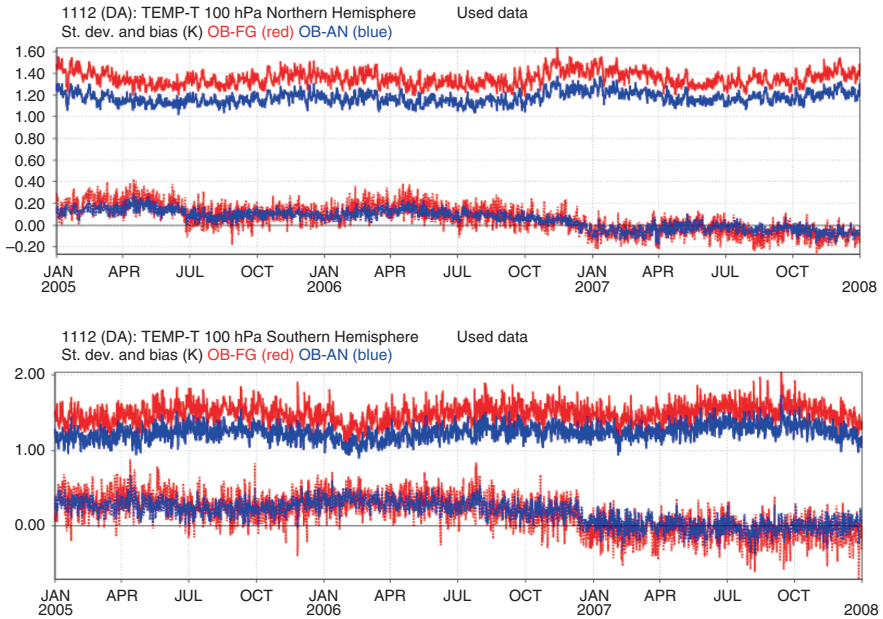
Fig. 4.23 The mean (dotted) and standard deviation (solid) of the ERA-Interim (observation minus background) and (observation minus analysis) temperature departures at 100 hPa in the northern and southern hemispheres. The background departures are in red and the analysis departures in blue. The period is from 1st January 2005 to 31st December 2007.

although the ensemble data assimilation techniques outlined by Tan et al. (2007) may be applicable.

4.8.3 Ground-Based GPS Observations

Ground-based networks of GPS receivers provide information on atmospheric humidity distribution. Meteorological use of these measurements relies on heavy pre-processing to account for various geophysical and geodetic effects. The quantity to be assimilated in NWP is usually Zenith Total Delay (ZTD); sometimes ZTD is converted further to PW prior to data assimilation. ZTD is one of the parameters that are estimated through a least-squares adjustment to find a geodetically consistent solution from a given set of raw measurement data.

ZTD is a measure of the so-called tropospheric refraction that follows from the fact that the propagation speed of microwave signals is decreased in a medium. In case of the neutral atmosphere, this loss of propagation speed is related to distributions of pressure, temperature and water vapour (Bevis et al. 1992). Forward modelling of ZTD observations from given background profiles makes use of these data in NWP. The accuracy of the background humidity field dominates the error budget of ZTD

forward modelling. Consequently, the information that is obtained via the ZTD observation minus background departures is translated primarily to the analysis of humidity and only secondarily to the analyses of pressure and temperature.

The major advantages of the ground-based GPS observing system include the high temporal observing resolution (up to around 5 min), the low financial cost of setting up and maintaining the equipment, and the ability of providing ZTD data with an accuracy and usability that is practically independent of the prevailing weather conditions. Due to these advantages, the GPS data is expected to remain an important complement to other humidity-related observing systems. The data assimilation of ZTD observations has already reached the operational status at the UK Met Office and Météo-France.

The ground-based GPS observing system consists of regional and local networks that, in most cases, have been originally set up for geodetic purposes by governmental institutes, or private agencies. The meteorological use of these networks comes as a by-product of the geodetic processing and it is usually of secondary importance from the maintenance point of view. Therefore, the observation density and the data quality vary considerably from one country to another. Moreover, the complexity of geodetic pre-processing makes it necessary in practice to limit the number of receiver stations to only few hundred at a time. This implies that there is a trade-off between the spatial resolution and coverage of the data that is to be pre-processed. The approach taken in Europe is to combine pre-processed data from a number of analysis centres that deal with the geodetic processing with different subsets of the available raw data. The resulting receiver station network, as on 9th September 2009, is shown in Fig. 4.24. Unfortunately, different analysis centres apply slightly different processing methods and software, which results in inhomogeneities in the ZTD data processed at the continental scale.

The ongoing EUMETNET GPS water vapour programme (E-GVAP) has paid significant attention on homogenizing both the ground-based GPS observing system and the pre-processing methods, but considerable inhomogeneities are still likely to be present in the data to be assimilated in Europe. The receiver networks in North America and Japan are likely to be more internally homogeneous. On a global scale, a homogeneous set of GPS ZTD data (from 420 receiver stations on 9th September 2009) are provided by the International GPS Service (IGS).

Pre-processing using geodetic software is a necessary step in order to have the ZTD (or PW) data available in the first place. Unfortunately, the pre-processing step makes observation error characteristics very complicated. The pre-processing introduces a spatially and temporally correlated component of observation error into the data. In order to maintain the statistical optimality of the data assimilation scheme, a way needs be found to deal with the correlation. The data assimilation experiments that have been performed so far have, almost exclusively, assumed that these correlations are negligible (Poli et al. 2007; Yan et al. 2009). This assumption is sometimes justified by applying horizontal thinning to the data (Macpherson et al. 2008). Another way to avoid dealing with observation error correlation is to decrease the weight of the correlated data by setting an overly large value for observation error standard deviation (Vedel and Sattler 2006).

Fig. 4.24 Status of the European ground-based GPS observing network on 9th September 2009, as reported by the E-GVAP programme. Green, yellow and red squares indicate the locations of those receiver stations for which the ZTD observation is as recent as 3, 6, and 54 h, respectively.

Slowly evolving observation biases constitute an even more severe complication to ZTD data assimilation. The origin of the bias is unknown. The fact that the bias seems to be specific to each receiver station makes it difficult to apply sophisticated bias correction schemes in a similar fashion that is applied in, for example, microwave and infrared radiance data assimilation. A common strategy is to derive receiver station-dependent bias corrections from past observation minus background departure statistics.

4.8.4   Impact Studies

Data assimilation experiments using ZTD data have been carried out in both regional 3D- and 4D-Var and global 4D-Var frameworks. The impact of ZTD data assimilation is reported to be slightly positive in terms of reduced forecast error on PW and other humidity-related parameters, surface pressure and geopotential height, and has thus improved the description of the synoptic circulation. The positive impact extends up to the fourth forecast day (Poli et al. 2007). However, the reported positive impacts on long-term verification scores are in most cases below the level of statistical significance. In addition to the standard upper-air meteorological parameters, in most studies a positive impact is found on the categorical forecasts of accumulated precipitation, in particular when relatively high precipitation accumulations are considered (Vedel and Sattler 2006; Macpherson et al. 2008).

More evidence of positive forecast impact is reported in the context of case studies focusing on intense precipitation events (De Pondeca and Zou 2001; Vedel and Sattler 2006; Yan et al. 2009).

Figure 4.25 shows an example of results of such a case study. In this particular case, a convective-scale NWP system Application of Research to Operations in
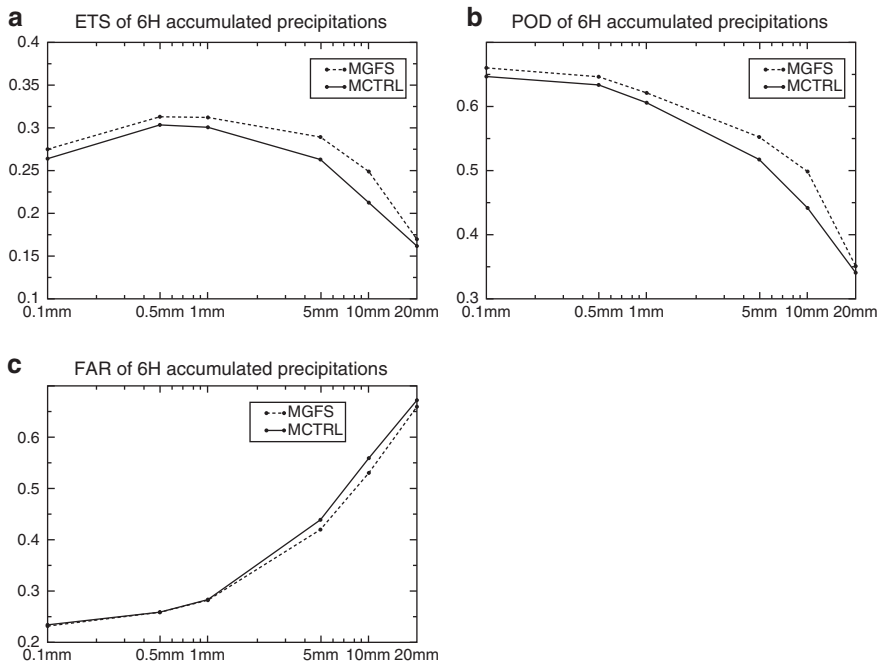

Fig. 4.25 Impact of ZTD data assimilation on (**a**) Equitable Threat Score, (**b**) Probability of Detection, and (**c**) False Alarm Rate of 6-h forecasts of accumulated precipitation in a case study of Mediterranean heavy rainfall. The experiment with ZTD data (dashed lines) shows improved scores with respect to the control run (solid lines) (Yan et al. 2009).

Meso-scale (AROME) has been deployed to investigate the impact of 3D-Var data assimilation of ZTD observations in a case of Mediterranean heavy rainfall. The positive impact of assimilating ZTD data is shown at all thresholds of 6-h accumulated precipitation.

4.9 Outlook

The following section highlights areas where promising work is ongoing or where the authors feel a special effort is needed in the future.

For all applications using microwave radiometry, improvements in microwave spectroscopy will help to interpret the collected data better. For example the question of line pressure broadening is an important topic, and in particular the non-resonant absorption of water vapour needs more work. Also improved modelling of cloud scattering effects, both for liquid and frozen particles, will help to retrieve cloud parameters and enable the observation of atmospheric composition within clouds. Such observations will also help to model chemical transport and climate forecasting better.

Synergetic use of the visible, infrared, and microwave observations has not yet been systematically explored for the retrieval of atmospheric constituents and parameters. Further investigations should be conducted, to benefit from the complementary sensitivities of the different wavelengths to each atmospheric parameter and so help constrain the inversion problem. This also includes the combined analysis of passive and active observations by microwave sensors as has been used successfully for the TRMM project.

While sensors operating in the visible and IR domains are limited to optically thin ice clouds with particle diameters <100 μm, microwave sensors observing below 200 GHz are insensitive to cloud ice water content lower than roughly 300 g/m^2. The sub-millimetre wavelength range appears to be well suited to cover this gap. Space-borne imagers and sounders for meteorological applications are so far limited to frequencies below 190 GHz. New sensors operating over a wide frequency range from 100 to 1,000 GHz to investigate cirrus clouds, would allow for the first time, the collection of global data sets with good horizontal resolution on the ice water content and on particle shapes and size distribution.

The success of the microwave limb sounder made NASA include, in its decadal survey of future earth-science missions, an advanced microwave limb sounder as one of the instruments in a future Global Atmospheric Composition Mission.

For future meteorology instrument scenarios, see for example the US-Europe Joint Polar System, combining the National Polar-Orbiting Operational Environmental Satellite System (NPOESS) and the follow-on to the EUMETSAT's Polar System (EPS), improvements are needed with respect to temperature sounding for the lower troposphere, and more complementary sounding and imaging capabilities to constrain clouds, precipitation and temperature/moisture at the same time. Soil moisture data assimilation also offers significant potential in the future. The

potential of soil moisture related observations on NWP forecast accuracy has long been recognized, in particular in situations where the atmospheric hydrological cycle is strongly affected by evaporation rather than oceanic moisture advection.

Future developments require, apart from refined instruments, more advanced data assimilation techniques and improved models. In particular, in areas where current systems do not fully exploit existing data, such as clouds and over land surfaces, better physical parameterisations and more flexible data assimilation techniques will greatly improve forecasting. The great potential of future microwave observations lies in constraining the models' hydrological cycle, namely the diabatic process in the atmosphere and, as mentioned above, soil moisture.

In addition to the GPM Core Satellite instruments, more sophisticated missions are planned, such as the European-GPM (EGPM) forming an important contributor to monitor the Earth's water cycle and climate at mid-to-high latitudes. EGPM consists of a sun-synchronous low Earth orbit satellite carrying two precipitation measurement payloads. A microwave radiometer containing, along with the standard precipitation channels from 18 to 150 GHz, an additional set of 50–55 and 118 GHz O_2 channels that would enable precipitation discrimination and profiling in light-to-moderate rainfall and snowfall, and a radar at Ka-band with a detection threshold of 5 dBZ, to measure light-to-moderate rainfall and snowfall, over both land and oceans, at both mid and high latitudes.

Millimetre and sub-millimetre observations from geostationary satellites are under investigation for near-real time estimates of precipitation, since current visible and IR observations from high orbit do not provide accurate quantification of the rain rates. High sampling intervals of precipitation are particularly crucial in the follow-up to severe weather events.

The recent successful operation of several smaller satellites flying in close formation, the A-Train including active and passive sensors, will certainly lead to similar missions, creating a larger observatory from several smaller spacecraft.

There is potential to extend the use of ground-based GPS measurements towards assimilation of slant delay (SD) observations in convection-resolving NWP systems. SD observations are inherently capable of containing information on azimuthal asymmetry and fine-scaled atmospheric structures, and are therefore of particular interest in forecasting high-impact severe weather phenomena. Unfortunately, the experience gathered to date suggests that the SD data is very noisy and suffers from significant observation error correlation. Operational use of SD data will therefore require a special effort in the further development of geodetic pre-processing, together with improved methods for data assimilation in convective scale NWP systems.

Finally on the hardware side the development of low noise sensors operating up to 1,000 GHz are needed for a number of applications, mainly to investigate clouds or to operate instruments on geostationary orbits. Also extremely low-noise sensors for measurements requiring high spectral resolution are needed, such as the cryogenic sensors presently being used by SMILES and planned for future limb sounders. For microwave sensors in geostationary orbit, as planned for continuous observations in the tropics and mid-latitudes, light-weight large antenna systems have to be developed, offering the required spatial resolution in the order of 10 km.

4.10   Tables of Microwave Sensors

Space borne passive microwave sensors in space are listed in Table 4.1 for meteorological observations and in Table 4.2 for limb sounders.

Table 4.1 A summary of operational meteorological microwave sensors presently in space

Instrument	Platform time coverage	Spectral range (GHz)	Scanning type Spatial resolution	Objectives
SSM/I	DMSP Since 1987	19VH, 22V, 37VH, 85VH	Conical scanning (53°) From 60 to 15 km	Integrated H_2O, cloud and rain, surface properties
SSMI/S	DMSP Since 2003	19VH, 22V, 37VH, 50-59H (7 channels), 91V, 150H, 183H (3 channels)	Conical scanning (53°) From 60 to 15 km	H_2O and T profiles, cloud and rain, surface properties
TMI	TRMM Since 1997	10VH, 19VH, 21V, 37VH, 85VH	Conical scanning (53°) From 50 to 6 km	Integrated H_2O, cloud and rain, surface properties
AMSR-E	NASA/Aqua Since 2002	19VH, 22V, 37VH, 85VH	Conical scanning (53°) From 50 to 5 km	Integrated H_2O, cloud and rain, surface properties
AMSU-A	NOAA, NASA/Aqua ESA/MetOp Since 1998	23, 33, 50–57 (12 channels), 89	Cross-track scanner (±50°) ~45 km at nadir	T profiles
AMSU-B	NOAA Since 1998	89, 157, 183 (3 channels)	Cross-track scanner (±50°) ~15 km at nadir	H_2O profiles
MHS	NASA/Aqua ESA/MetOp Since 2003	150, 183 (3 channels)	Cross-track scanner (±50°) ~15 km at nadir	H_2O profiles
MWRI	FY-3 Since May 2008	10VH, 19VH, 24VH, 36VH, 89VH, 150 VH	Conical scanning (53°) From 15 to 80 km	Integrated H_2O, cloud and rain, surface properties
MWTS	FY-3 Since May 2008	50–57 (4 channels)	Cross-track scanner (±53°) ~50 km at nadir	T profiles
MWHS	FY-3 Since May 2008	150, 183 (3 channels)	Cross-track scanner (±53°) ~15 km at nadir	H_2O profiles

Table 4.2 Summary of previous, current and planned microwave limb sounding instruments

Instrument	Mission timespan	Developer	Radiometers	Main Stratospheric products	Main Tropospheric products
MLS	UARS Sep 1991 – Jan 2000	NASA JPL, USA	63 GHz, 205 GHz, 183 GHz	Temperature, O_3, H_2O, ClO	Temperature, H_2O, Cloud Ice
MAS	ATLAS Mar 1992, Mar/Apr 1993, Nov 1994	MPI, Aeronomy, D, Uni-Bern, CH, NRL, USA	63 GHz, 183 GHz, 205 GHz	Temperature, O_3, H_2O, ClO	Temperature, H_2O, Cloud Ice
SMR	Odin Feb 2001 to present	Chalmers Uni., S, Swedish Space Corp.	119 GHz, 486–503 GHz, 541–581 GHz	ClO, O_3, N_2O, H_2O, $H_2^{17}O$, $H_2^{18}O$, CO, HO_2, HNO_3, NO, HDO,	H_2O, Cloud ice
MLS	Aura July 2004 to present	NASA JPL	118 GHz, 190 GHz, 240 GHz, 640 GHz, 2,500 GHz	Temperature, GPH, H_2O, O_3, HNO_3, N_2O, ClO, HCl, HOCl, BrO, CO, HCN, CH_3CN, SO_2, OH, HO_2	Temperature, H_2O, O_3, CO, HNO_3, Cloud Ice
JEM/SMILES	ISS Launched 2009	JAXA, J	640 GHz superconducting receiver	O_3, HCl, ClO, HO_2, H_2O_2, HOCl, BrO, HNO_3	

References

Adler, R. F., G. J. Huffman, A. Chang, R. Ferraro, P. Xie, J. Janowiak, B. Rudolf, U. Schneider, S. Curtis, D. Bolvin, A. Gruber, J. Susskind, P. Arkin, and E. Nelkin, 2003, The version 2 global precipitation climatology project (gpcp) monthly precipitation analysis (1979-Present). *J. Hydrometeor.*, **4**, 1147–1167.

Aires, F., C. Prigent, W. Rossow, and M. Rothstein, 2001, A new neural network approach including first guess for retrieval of atmospheric water vapor, cloud liquid water path, surface temperature, and emissivities over land from satellite microwave observations. *J. Geophys. Res.*, **106**, D14, 14887–14907.

Akvilonova, A. B., A. E. Basharinov, A. K. Gorodetskii, A. S. Gurvich, M. S. Krilova, B. G. Kutuza, D. T. Matveev, and A. P. Orlov, 1973, Determination of meteorological parameters wit measurements from the satellite Cosmos-384. *Atmos. Ocean. Phys.*, **9**, 187–198.

Alishouse, J. C., S. A. Snyder, E. R. Westwater, C. T. Swift, C. S. Ruf, S. A. Snyder, J. Vonsathom, and R. R. Ferraro, 1990, Determination of cloud liquid water content using the SSM/I. *IEEE Trans. Geosci. Remote Sens.*, **28**, 817–822.

Allan, D. W., 1966, Statistics of Atomic Frequency Standards. *Proc. IEEE.*, **54**, 221–230.

Andersson, E., J. Pailleux, J.-N. Thépaut, J. R. Eyre, A. P. McNally, G. A. Kelly, and P. Courtier, 1994, Use of cloud-cleared radiances. *Q. J. R. Meteorol. Soc.*, **120**, 627–653.

Andersson, E., R. Dumelow, H. Huang, J.-N. Thépaut, and A. Simmons, 2004, Space/terrestrial link – outline study proposal for consideration by EUCOS management (available at EUCOS secretariat).

Andersson, E., E. Holm, P. Bauer, A. Beljaars, G. A. Kelly, A. P. McNally, A. J. Simmons, and J.-N. Thépaut, 2007, Analysis and forecast impact of the main humidity observing system. *Q. J. R. Meteorol. Soc.*, doi: 10.1002/QJ.112.

Andersson, E., and J.-N. Thépaut, 2008, ECMWF's 4D-Var data assimilation system - the genesis and ten years in operation. *ECMWF Newsletter*, **115**, 8–12.

Anthes, R., P. A. Bernhardt, Y. Chen, L. Cucurull, K. F. Dymond, D. Ector, S. B. Healy, S.-P. Ho, Y.-H. Kuo, D. C. Hunt, H. Liu, K. Manning, C. McCormick, T. K. Meehan, W. J. Randel, C. Rocken, W. S. Schreiner, S. V. Sokolovskiy, S. Syndergaard, D. C. Thompson, K. E. Trenberth, T. K. Wee, N. L. Yen, and Z. Zeng, 2008, The COSMIC/FORMOSAT-3 Mission, Early Results. *Bull. Am. Meteor. Soc.*, **89**, 313–333.

Aparicio, J., and G. Deblonde, 2008, Imapct of the assimilation of [CHAMP] refractivity profiles in environment canada global forecasts. *Mon. Wea. Rev.*, **136**, 257–275.

Arnold, C.P. and C.H. Dey, 1986, Observing-system simulation experiments: Past, present and future, *Bull. Amer. Meteorol. Soc.*, **67**, 687–695.

Auligné, T., A.P. McNally, and D.P. Dee, 2007, Adaptive bias correction for satellite data in a numerical weather prediction system, *Q. J. R. Meteorol. Soc.*, **133**, 631–642.

Barath, F.T., A.H. Barrett, J. Copeland, D.E. Jones, and A.E. Lilley, 1964, Mariner 2 microwave radiometer experiments and results, *Astron. J.*, **69**, 49–58.

Barath, F.T., M.C. Chavez, R.E. Cofield, D.A. Flower, M.A. Frerking, M.B. Gram, W.M. Harris, J.R. Holden, R.F. Jarnot, W.G. Kloezeman, G.J. Klose, G.K. Lau, M.S. Loo, B.J. Maddison, R.J. Mattauch, R.P. McKinney, G.E. Peckham, H.M. Pickett, G. Siebes, F.S. Soltis, R.A. Suttie, J.A. Tarsala, J.W. Waters, and W.J. Wilson, 1993, The Upper Atmosphere Research Satellite Microwave Limb Sounder Experiment, *J. Geophys. Res.*, **98**, 10,751–10,762.

Battaglia, A., M.O. Ajewole and C. Simmer, 2006, Evaluation of radar multiple scattering effects from a GPM perspective. Part I: model description and validation, *J. Appl. Meteor. Clim.*, 45, 12, 1634–1647.

Battaglia, A., C.P. Davis, C. Emde and C. Simmer, 2007, Microwave radiative transfer intercomparison study for 3-D dichroic media. *J. Quant. Spectrosc. Radiat. Transfer*, **105**, 55–67.

Bauer, P., and P. Schluessel, 1993, Rainfall, total water, ice water, and water vapor over sea from polarized microwave simulations and Special Sensor Microwave Imager data. *J. Geophys. Res.*, **98(D11)**, 20737–20759.

Bauer P., P. Amayenc, C.D. Kummerow, E.A. Smith, 2001a, Over-ocean rainfall retrieval from multisensor data of the Tropical Rainfall Measuring Mission. Part I: Design and evaluation of inversion databases. *J. Atmos. Oceanic Technol.*, **18**, 1315–1330.

Bauer P. 2001b, Over-ocean rainfall retrieval from multisensor data of the Tropical Rainfall Measuring Mission. Part II: Algorithm implementation. *J. Atmos. Oceanic Technol.*, **18**, 1838–1855.

Bauer P., A. Mugnai, 2003, Precipitation profile retrievals using temperature-sounding microwave observations, *J. Geophys. Res.,* **108(23)**, 4730, doi:10.1029/2003JD003572.

Bauer, P., E. Moreau, F. Chevallier, and U. O'Keefe, 2006a, Multiple-scattering microwave radiative transfer for data assimilation applications. *Q. J. R. Meteorol. Soc.*, **132**, 1259–1281.

Bauer, P., P. Lopez, A. Benedetti, D. Salmond, and E. Moreau, 2006b, Implementation of 1D+4D-Var assimilation of precipitation affected microwave radiances at ECMWF, Part I: 1D-Var, *Q. J. R. Meteorol. Soc.*, **132**, 2277–2306.

Bauer, P., P. Lopez, A. Benedetti, D. Salmond, S. Saarinen and M. Bonazzola, 2006 c, Implementation of 1D+4D-Var assimilation of precipitation affected microwave radiances at ECMWF, Part II: 4D-Var, *Q. J. R. Meteorol. Soc.*, **132**, 2307–2332.

Benedetti, A., P. Lopez, P. Bauer, and E. Moreau, 2005, Experimental use of TRMM Precipitation Radar observations in 1D+4D-Var assimilation. *Q.J.R. Meteorol. Soc.*, **131**, 2473–2495.

Bevis, M., S. Businger, T.A. Herring, C. Rocken, R.A. Anthes, and R.H. Ware, 1992, GPS Meteorology: Remote Sensing of Atmospheric Water Vapor Using the Global Positioning System. *J. Geophys. Res.*, **97(D14)**, 15787–15801.

Bohren, C., and D.R. Huffman, 1998, Absorption and scattering of light by small particles, Wiley Science Paperback Series.

Borg, L.A. and R. Bennartz, 2007, Vertical structure of stratiform marine boundary layer clouds and its impact on cloud albedo, *Geophys. Res. Lett.*, 34, L05807, doi:10.1029/2006GL028713.

Bouttier, F., and P. Courtier, 2002, Data assimilation concepts and methods, ECMWF Training course lectures, available from ECMWF, Shinfield Park, Reading, UK, 59p.

Buehler, S.A., P. Eriksson, T. Kuhn, A. von Engeln, C. Verdes, 2005, ARTS, the atmospheric radiative transfer simulator, *J. Quant. Spectros. Radiat. Transfer,* **91**, 65–93.

Buehler, S.A., C. Jiménez, K.F. Evans, P. Eriksson, B. Rydberg, A.J. Heymsfield, C. Stubenrauch, U. Lohmann, C. Emde, V.O. John, T.R. Sreerekha and C.P. Davis, 2007, A concept for a satellite mission to measure cloud ice water path and ice particle size, *Q. J. R. Meteorol. Soc.*, **133**, 109–128, doi:10.1002/QJ.143.

Cabrera-Mercader, C.R. and D.H. Staelin, 1995, Passive microwave relative humidity retrievals using feedforward neural networks, *IEEE Trans. Geosci. Remote Sensing,* **33**, 1324.

Cardinali, C., S. Pezzulli, and E. Andersson, 2004, Influence-matrix diagnostic of a data assimilation system, *Q. J. R. Meteorol. Soc.*, **130**, 2767–2786.

Cecil, D.J., S.J. Goodman, D.J. Boccippio, E.J. Zipser and S.W. Nesbitt, 2005, Three years of TRMM precipitation features. Part I: Radar, radiometric, and lightning characteristics, *Month. Weather Rev.*, **133**, 543–566.

Chandra, S., J.R. Ziemke, W. Min, and W.G. Read, 1998, Effects of 1997–1998 El Niño on tropospheric ozone and water vapor, *Geophys. Res. Lett.*, **25**, 3867–3870.

Chandrasekhar, S., 1960, Radiative transfer, Dover Publications, New York.

Chang, A.T.C. and T.T. Wilheit, 1979, Remote sensing of atmospheric water vapor, liquid water, and wind speed at the ocean surface by passive microwave techniques from the Nimbus-5 satellite, *Radio Sci.*, **14**, 793–802.

Collard, A., and S. Healy, 2003, The combined impact of future space-based atmospheric sounding instruments on numerical weather prediction analysis fields: A simulation study. *Quart. J. Roy. Meteorol. Soc.*, **129**, 2741–2760.

Courtier, P., J. Derber, R. Errico, J.-F. Luis, and T. Vukicevic, 1993, Important literature on the use of adjoint, variational methods and the Kalman filter in meteorology, *Tellus*, **45A,** 342–357.

Croskey, C.L., N. Kaempfer, R. Belivacqua, G.K. Hartmann, K.F. Kunzi, P. Schwartz, J.J. Olivero, S.E. Puliafito, C. Aellig, G. Umlauft, 1992, The Millimeter Wave Atmospheric

Sounder (MAS): A shuttle-based remote sensing experiment, *IEEE Trans. Microwave Theory and Techniques,* **40,** 1090–1100.

Cucurull, L., J. Derber, R. Treadon, and R. Purser, 2007, Assimilation of Global Positioning System Radio Occultation Observations into NCEP's Global Data Assimilation System. *Mon. Wea. Rev.*, **135**, 3174–3193.

Czekala, H., and C. Simmer, 1998, Microwave radiative transfer with nonspherical precipitating hydrometeors, *J. Quant. Spectrosc. Radiat. Transfer*, **60**, 3, 365–374.

Daley, R., 1991, Atmospheric Data Analysis, Cambridge Atmospheric and Space Science Series, Cambridge University Press, Cambridge, 457pp.

Davis, C., C. Emde and R. Harwood, 2005, A 3D polarized reversed Monte Carlo radiative transfer model for mm and sub-mm passive remote sensing in cloudy atmospheres, *IEEE Trans. Geosci. Remote Sens.,* **43(6)**, 1096–1101.

Deblonde, G., and N. Wagneur, 1997, Evaluation of global numerical weather prediction analysis and forecasts using DMSP special sensor microwave imager retrievals 1. Satellite retrieval algorithm intercomparison study, *J. Geophys. Res.,* **102, D2**, 1833–1850.

Dee, D.P., and A.M. Da Silva, 2003, The choice of variable for atmospheric moisture analysis, *Mon. Wea. Rev*., **131**, 155–171.

Dee, D., 2005, Bias and data assimilation. Quart. J. Roy. Meteorol. Soc., 131, 3323–3343.

Deeter, M.N., and K.F. Evans, 2000, A novel ice-cloud retrieval algorithm based on the Millimeter-wave Imaging Radiometer (MIR) 150–220 GHz channels, *J. Appl. Meteorol.*, **39**, 623–633.

Defer, E., C. Prigent, F. Aires, J.R. Pardo, J.C. Walden, O.-Z. Zanife, J.-P. Chaboureau, and J.-P. Pinty, 2008, Developments of precipitation retrievals at millimeter and sub-millimeter wavelength for geostationary satellites, *J. Geophys. Res.,* **113**, D08111, doi:10.1029/2007JD008673.

De Pondeca, M. and X. Zou, 2001, A case study of the variational assimilation of GPS zenith delay observations into a mesoscale model. *J. Appl. Meteorol.*, **40**, 1559–1576.

Derber, J.C. and W.-S. Wu, 1998, The use of TOVS cloud-cleared radiances in the NCEP SSI analysis system, *Mon. Wea. Rev.*, **8**, 2287–2302.

Di Michele, S., F.S. Marzano, A. Mugnai, A. Tassa, and J.P.V. Poiares Baptista, 2003, Physically based statistical integration of TRMM microwave measurements for precipitation profiling. *Radio Sci.,* **38 (8072)**, doi:10.1029/2002RS002636, 16 pp.

Draine, B.T. (2000) The Discrete Dipole Approximation for Light Scattering by Irregular Targets, In: M.I. Mishchenko, J.W. Hovenier, and L.D. Travis (eds) Light Scattering by Nonspherical Particles: Theory, Measurements and Applications. Academic Press, London, pp. 131–144.

Drusch, M., 2007, Initializing numerical weather prediction models with satellite-derived surface soil moisture: Data assimilation experiments with ECMWF's integrated forecasting system and the TMI soil moisture data set, *J. Geophys. Res.*, **112**, doi:10.1029/2006JD007478.

Ekström, M., P. Eriksson, D. Rydberg, and D.P. Murtagh, 2007, First Odin sub-mm retrievals in the tropical upper troposphere: humidity and cloud ice signals, *Atmos. Chem. Phys.*, **7**, 459–469.

Ekström, M., P. Eriksson, W.G. Read, M. Milz, and D.P. Murtagh, 2008, Comparison of satellite limb-sounding humidity climatologies of the uppermost tropical troposphere, *Atmos. Chem. Phys.*, **8**, 309–320.

Emde, C., S.A. Buehler, C. Davis, P. Eriksson, T.R. Sreerekha and C. Teichmann, 2004, A polarized discrete ordinate scattering model for simulations of limb and nadir longwave measurements in 1D/3D spherical atmospheres, *J. Geophys. Res.,* **109(24)**, 24207.

Eriksson, P., M. Ekström, S.A. Buehler and C. Melsheimer, 2006, Efficient forward modelling by matrix representation of sensor responses. *Int. J. Remote Sensing*. **27**, 1793–1808.

Eriksson, P., M. Ekström, B. Rydberg, and D.P. Murtagh, 2007, First Odin sub-mm retrievals in the tropical upper troposphere: ice cloud properties, *Atmos. Chem. Phys.*, **7**, 471–483.

Eriksson, P., S.A. Buehler, (eds), 2008, ARTS-1.x user guide (available at http://www.sat.ltu.se/arts/misc/arts2/doc/uguide/uguide.pdf).

Eriksson, P., M. Ekström, B. Rydberg, D.L. Wu, R.T. Austin, and D.P. Murtagh, 2008, Comparison between early Odin-SMR, Aura MLS and CloudSat retrievals of cloud ice mass in the tropical upper troposphere, *Atmos. Chem. Phys.*, **8,** 1937–1948.

Errico, R., P. Bauer, and J.-F. Mahfouf, 2007, Assimilation of cloud and precipitation data: Current issues and future prospects, *J. Atmos. Sci.*, **64,** 3789-3802.

Evans, K.F. and J. Vivekanandan, 1990, Multiparameter radar and microwave radiative transfer modeling of non spherical atmospheric ice particles, *IEEE Trans. Geosci. Remote Sens.*, **28**, 423–437.

Evans, K.F., and G.L. Stephens, 1995a, Microwave radiative transfer through clouds composed of realistically shaped ice crystals, part I, Single scattering properties, *J. Atmos. Sci.*, **52**, 2041–2057.

Evans, K.F., and G.L. Stephens, 1995b, Microwave radiative transfer through clouds composed of realistically shaped ice crystals, part II, Remote sensing of ice clouds, *J. Atmos. Sci.*, **52**, 2058–2072.

Evans, K.F., S.J. Walter, A.J. Heymsfield, and M.N. Deeter, 1998, Modeling of submillimeter passive remote sensing of cirrus clouds, *J. Appl. Meteorol.*, **37**, 184–205.

Evans, K.F., 1998, The spherical harmonic discrete ordinate method for three-dimensional atmospheric radiative transfer. *J. Atmos. Sci.*, **55**, 429–446.

Evans, K.F., A.H. Evans, I.G. Nolt. and B.T. Marshall, 1999, The prospect for remote sensing of cirrus clouds with a submillimeter-wave spectrometer, *J. Appl. Meteorol.*, **38**, 514–525.

Evans, K.F., S.J. Walter, A.J. Heymsfield and G.M. McFarquhar, 2002, The submillimeter-wave cloud ice radiometer: Simulations of retrieval algorithm performance. *J. Geophys. Res.,* **107**, doi: 10.1029/2001JD000709.

Evans, K.F., J.R. Wang, P. Racette, G. Heymsfield and L. Li, 2005, Ice cloud retrievals and analysis with data from the Compact Scanning Submillimeter Imaging Radiometer and the Cloud Radar System during CRYSTAL-FACE, *J. Appl. Meteor.*, **44**, 839–859.

Eyre, J.R. 1991, A fast radiative transfer model for satellite sounding systems, ECMWF Research Dept. Tech. Memo. **176** (available from the librarian at ECMWF)

Eyre, J., G.A. Kelly, A.P. McNally, E. Andersson, and A. Persson, 1993, Assimilation of TOVS radiance information through one-dimensional variational analysis*, Q. J. R. Meteorol. Soc.,* **119**, 1427–1463.

Farrar, M.R., 1997, Combined Radar-Radiometer Rainfall Retrieval for TRMM Using Structure Function-Based Optimization. Ph.D. Dissertation (E.A. Smith, Major Prof.), Dept. of Meteorology, The Florida State University, Tallahassee, FL, 185 pp.

Ferraro, R.R, F. Weng, N.C. Grody and L. Zhao, 2000, Precipitation characteristics over land from the NOAA-15 AMSU Sensor. *Geophys. Res. Let.*, **27**, 2669–2672.

Ferraro, R.R., F. Weng, N. Grody, L. Zhao, H. Meng, C. Kongoli, P. Pellegrino, S. Qiu and C. Dean, 2005, NOAA operational hydrological products derived from the AMSU, *IEEE Trans. Geo. Rem. Sens.,* **43**, 1036–1049.

Filipiak, M.J., R.S. Harwood, J.H. Jiang, Q. Li, N.J. Livsey, G.L. Manney, W.G. Read, M.J. Schwartz, J.W. Waters, D.L. Wu, 2005, Carbon monoxide measured by the EOS Microwave Limb Sounder on Aura: First results, *Geophys. Res. Lett.*, **32**, L14825, doi:1029/2005GL022765.

Fiorino, S.T., and E.A. Smith, 2006, Critical assessment of microphysical assumptions within TRMM-radiometer rain profile algorithm using satellite, aircraft and surface datasets from KWAJEX. *J. Appl. Meteor. Clim.*, **45**, 754–786.

Forster, P.M.d.F., and K.P. Shine, 1997, Radiative forcing and temperature trends from stratospheric ozone changes, *J. Geophys. Res.*, **102**, 10841–10855.

Gasiewski, A.J., 1992, Numerical sensitivity analysis of passive EHF and SMMW channels to tropospheric water vapor, clouds, and precipitation, *IEEE Trans. Geosci. Remote Sens.*, **30**, 859–870.

Goody, R.M., and Y.L. Yung, 1989, Atmosphere radiation, Theoretical basis (2ed), Oxford University Press.

Greenwald, T.J., G.L. Stephens, T.H.V. Haar and D.L. Jackson, 1993, A Physical Retrieval of Cloud Liquid Water Over the Global Oceans Using Special Sensor Microwave/Imager (SSM/I) Observations, *J. Geophys. Res.*, **98(10)**, 18,471–18,488.

Greenwald T.J. and S.A. Christopher, 2002, Effect of cold clouds on satellite measurements near 183 GHz, *J. Geophys. Res.*, **107**, 4170, doi:10.1029/2000JD000258.

Greenwald, T.J., T.S. L'Ecuyer and S.A. Christopher, 2007, Evaluating specific error characteristics of microwave-derived cloud liquid water products, *Geophys. Res. Lett.,* **34**, L22807, doi:10.1029/2007GL031180.

Grody, N.C., 1991, Classification of snow cover and precipitation using the Special Sensor Microwave/Imager (SSM/I), *J. Geophys. Res.*, **96**, 7423–7435.

Haddad, Z.S., E.A. Smith, C.D. Kummerow, T. Iguchi, M.R. Farrar, S.L. Durden, M. Alves, and W.S. Olson, 1997, The TRMM 'Day-1' radar/radiometer combined rain-profiling algorithm. *J. Meteor. Soc. Japan*, **75**, 799–809.

Haynes, J. L'Ecuyer, G. Stephens, S. Miller, C. Mitrescu and S. Tanelli, 2008, Rainfall retrieval over the ocean with spaceborne W-band radar, *J. Geophys. Res.*, **114**, D00A22, doi:10.1029/2008JD009973.

Healy, S., and J.-N. Thépaut, 2006, Assimilation experiments with CHAMP GPS radio occultation measurements. *Quart. J. Roy. Meteorol. Soc.*, **132**, 605–623.

Healy, S., J. Eyre, M. Hamrud, and J.-N. Thépaut, 2007, Assimilating GPS radio occultation measurements with two-dimensional bending angle observation operators. *Quart. J. Roy. Meteorol. Soc.*, **133**, 1213–1227.

Held, I. M., and B. J. Soden, 2000, Water vapor feedback and global warming, *Ann. Rev. Energy Environ.*, **24**, 441–475.

Heymsfield, A. J., A. Bansemer, C. Schmitt, C. Twohy and M. R. Poellot, 2004, Effective ice particle densities derived from aircraft data, *J. Atmos. Sci.*, 61, 982–1003.

Hitschfeld, W., and J. Bordan, 1954, Errors inherent in the radar measurement of rainfall at attenuating wavelengths. *J. Meteor.*, **11**, 58–67.

Hong G., G. Heygster, and K. Kunzi 2005 a, Intercomparison of deep convective cloud fractions from passive infrared and microwave radiance measurements, IEEE Geosc. Remote Sensing Lett., **2**, 18–24.

Hong, G., G. Heygster, J. Miao and K. Kunzi, 2005b, Detection of tropical deep convective clouds from AMSU-B water vapor channels measurements, *J. Geophys. Res.*, **110**, D05205, doi:10.1029/2004JD004949.

Hong, Y., T.R. Wilheit, and W.R. Russell, 1997, Estimation of monthly rainfall over oceans from truncated rain-rate samples: Applications to SSM/I data. *J. Atmos. Oceanic Technol.*, **14**, 1012–1022.

Horváth Á. and R. Davies, 2007, Comparison of microwave and optical cloud water path estimates from TMI, MODIS, and MISR, J. Geophys. Res., **112**, D01202, doi:10.1029/2006JD007101.

Iguchi, T., and R. Meneghini, 1994, Intercomparison of single-frequency methods for retrieving a vertical rain profile from airborne or spaceborne radar data. *J. Atmos. Oceanic Tech.*, **11**, 1507–1511.

Iguchi, T., T. Kozu, R. Meneghini, J. Awaka, and K. Okamoto, 2000, Rain-profiling algorithm for the TRMM precipitation radar. *J. Appl. Meteor.*, **39**, 2038–2052.

Iguchi, T., 2007, Space-borne radar algorithms. Measuring Precipitation from Space: EURAINSAT and the Future (V. Levizzani, P. Bauer, and F.J. Turk, eds.), Advances in Global Change Research (Vol. 28), Springer, Dordrecht, Netherlands, 199–212.

Im, E., C. Wu and S.L. Durden, 2005, Cloud profiling radar for the CloudSat mission, IEEE Radar Conference, 9–12 May, pp 483–486.

Janssen, M.A., 1993, Atmospheric remote sensing by microwave radiometry, Wiley, ISBN 0-471-62891-3

Jensen, A., M. Lohmann, H.-H. Benzon, and A. Nielsen, 2003, Full Spectrum Inversion of radio occultation signals. Radio Sci., **38,** 1040, doi:10.1029/2002RS002763.

Jiang, J.H., N.J. Livesey, H. Su, L. Neary, J.C. McConnell, and N.A.D. Richards, 2007, Connecting surface emissions, convective uplifting, and long-range transport of carbon monoxide in the upper-troposphere: New observations from the Aura Microwave Limb Sounder, Geophys. Res. Lett., **34**, L18812, doi:10.1029/2007GL030638.

Jiménez, C., P. Eriksson, V.O. John and S.A. Buehler, 2005, A demonstration of AMSU retrieval precision for mean upper tropospheric humidity by a non-linear multi-channel regression method, Atmos. Chem. Phys., **5**, 451–459.

Jiménez, C., S.A. Buehler, B. Rydberg, P. Eriksson and K.F. Evans, 2007, Performance simulations for a submillimetre wave cloud ice satellite instrument, *Q. J. R. Meteorol. Soc.*, **133,** 129–149, doi:10.1002/QJ.134.

Joiner, J. and D.P. Dee, 2000, An error analysis of radiance and suboptimal retrieval assimilation, *Q. J. R. Meteorol. Soc.*, **126**, 1495–1514.

Jones, A. and T. Vonder Haar, 1990, Passive microwave remote sensing of cloud liquid water over land regions, *J. Geophys. Res.*, **95**, 10, 16673–16683.

Karbou, F., Aires, F., Prigent, C., L. Eymard, 2005, Potential of Advanced Microwave Sounding Unit-A (AMSU-A) and AMSU-B measurements for atmospheric temperature and humidity profiling over land, *J. Geophys. Res.*, **110**, D07109 10.1029/2004JD005318.

Kay, J.E., T. L'Ecuyer, G.L. Stephens, A. Gettelman, and C.O'Dell, 2008, The contribution of cloud and radiation anomalies to the 2007 Arctic sea ice extent minimum, *Geophys. Res. Lett.*, 35, L08503, doi:10.1029/2008GL033451.

Kelly, G.A. and J.-N. Thépaut, 2007, Evaluation of the impact of the space component of the Global Observing System through observing system experiments, ECMWF Newsletter, **113**, 16–28.

Kim M.-J., 2006, Single scattering parameters of randomly oriented snow particles at microwave frequencies, J. Geophys. Res., **111,** 14201, doi:10.1029/2005JD006892.

Kim, M., J.A. Weinman, W.S. Olson, D.-E. Chang, G. Skofronick-Jackson and J.R. Wang, 2008, A physical model to estimate snowfall over land using AMSU-B observations, *J. Geophys. Res.*, **113**, doi: 10.1029/2007JD008589.

Klein B., S.D. Philipp, R. Güsten, I. Krämer, D. Samtleben, 2006, A new generation of spectrometers for radio astronomy: Fast Fourier Transform Spectrometer, SPIE-FFTS2006.pdf

Klein, M., and A.J. Gasiewski, 2000, Nadir sensitivity of passive millimeter and submillimeter wave channels to clear air temperature and water vapor variations, *J. Geophys. Res.*, **105**, 17 481–17 511.

Kozu, T., T. Kawanishi, H. Kuroiwa, M. Kojima, K. Oikawa, H. Kumagai, K. Okamoto, M. Okumura, H. Nakatsuka, K. Nishikawa, 2001, Development of Precipitation Radar on-board the Tropical Rainfall Measuring Mission satellite. IEEE Trans. Geosci. Rem. Sens., **39**, 102–116.

Krasnopolsky, V.M., 2007, Neural network emulations for complex multidimensional geophysical mappings: Applications of neural network techniques to atmospheric and oceanic satellite retrievals and numerical modelling, Rev. Geophys., **45**, RG3009, doi:10.1029/2006RG000200.

Kuhn, T., 2003, Atmospheric absorption models for the millimeter range, PhD thesis, University of Bremen.

Kummerow C.D., R.A. Mack and I.M. Hakkarinen, 1989, A self-consistency approach to improve microwave rainfall estimates from space. *J. Appl. Meteor.*, **39**, 1801–1820

Kummerow C.D. and L. Giglio, 1994, A passive microwave technique for estimating rainfall and vertical structure information from space. Part I: algorithm description. *J. Appl. Meteor.*, **33**, 3–18.

Kummerow, C., W.S. Olson and L. Giglio, 1996, A simplified scheme for obtaining precipitation and vertical hydrometeor profiles from passive microwave sensors. IEEE. Trans. Geosci. Remote Sensing, **34**, 1213–1232.

Kummerow, C., W. Barnes, T. Kozu, J. Shiue, and J. Simpson, 1998, The tropical rainfall measuring mission (TRMM) sensor package. *J. Atmos. Oceanic Tech.*, **15**, 809–817.

Kummerow, C., J. Simpson, O. Thiele, W. Barnes, A.T.C. Chang, E. Stocker, R.F. Adler, A. Hou, R. Kakar, F. Wentz, P. Ashcroft, T. Kozu, Y. Hong, K. Okamoto, T. Iguchi, H. Kuroiwa, E. Im, Z. Haddad, G. Huffman, B. Ferrier, W.S. Olson, E. Zipser, E.A. Smith, T.T. Wilheit, G. North, T. Krishnamurti, and K. Nakamura, 2000, The status of the Tropical Rainfall Measuring Mission (TRMM) after two years in orbit. *J. Appl. Meteor.*, **39**, 1965–1982.

Kummerow, C., Y. Hong, W.S. Olson, S. Yang, R.F. Adler, J. McCollum, R. Ferraro, G. Petty, D.-B. Shin, and T.T. Wilheit, 2001, The evolution of the Goddard Profiling Algorithm (GPROF) for rainfall estimation from passive microwave sensors. *J. Appl. Meteor.*, **40**, 1801–1820.

Kunzi, K., G. Heygster and J. Miao, 2001, Ice cloud and background water vapour by sub-mm and very-high frequency MW radiometer, CLOUDS, A cloud, aerosol, radiation and precipitation explorer, proposal submitted to the ESA Call for Ideas for the Next Earth Explorer Core Missions.

Kursinski, E., G. Hajj, W. Bertiger, S. Leroy, T. Meehan, L. Romans, J. Schofield, D. McCleese, W. Melbourne, C. Thornton, T. Yunck, J. Eyre, and R. Nagatani, 1996, Initial results of radio occultation observations of earth's atmosphere using the Global Positioning System. Science, **271**, 1107–1110.

Kursinski, E., G. Hajj, J. Schofield, R. Linfield, and K. Hardy, 1997, Observing earth's atmosphere with radio occultation measurements using the Global Positioning System. *J. Geophys. Res.*, **102,** 23429–23465.

Lafore, J.-P.J. Stein, N. Asencio, P. Bougeault, V. Ducrocq, J. Duron, C. Fischer, P. Héreil, P. Mascart, V. Masson, J.-P. Pinty, J.-L. Redelsperger, E. Richard, J. Vilà-Guerau de Arellano, 1998, The Meso–NH Atmospheric Simulation System. Part I: adiabatic formulation and control simulations Scientific objectives and experimental design, *Ann. Geophys.*, **16**, 90–109.

L'Ecuyer, T.S. and G.L. Stephens, 2003, The tropical oceanic energy budget from the TRMM perspective, Part I: Algorithm and uncertainties, *J. Clim.*, 16, 1967–1985.

Li, Q. B., J.H. Jiang, W.G. Read, N.J. Livesey, J.W. Waters, Y. Zhang, B. Wang, M.J. Filipiak, C.P. Davis, S. Turquety, S. Wu, R.J. Park, R.M. Yantosca, D.J. Jacob, 2005, Convective outflow of South Asian pollution: A global CTM simulation compared with EOS MLS observations, *Geophys. Res. Lett.*, **32**, L14826, doi:10.1029/2005GL022762.

Liebe, H.J., G.A. Hufford and M.G. Cotton, 1993, Propagation modeling of moist air and suspended water/ice particles at frequencies below 1000 GHz., in AGARD 52nd Specialists Meeting of the Electromagnetic Wave Propagation Panel, Palma de Mallorca, Spain, pp. 3.1–3.10.

Lin, B. and W. Rossow, 1994, Observations of cloud liquid water path over oceans: Optical and microwave remote sensing methods, *J. Geophys. Res.*, **99**, 10, 20907–20927.

Lin, B. and W.B. Rossow, 1996, Seasonal variation of liquid and ice water path in non-precipitating clouds over oceans, *J. Clim.*, **9**, 2890–2902.

Liou, K.N., 2002, An introduction to atmospheric radiation, 2nd ed., Academic Press.

Liu, G. and J. Curry, 1993, Determination of characteristic features of cloud liquid water from satellite microwave measurements, *J. Geophys. Res.*, **98(D3),** 5069–5092.

Liu, G. and J.A. Curry, 1998, Remote sensing of ice water characteristics in tropical clouds using aircraft microwave measurements, *J. Appl. Meteorol.*, **37**, 337-355.

Liu, G. and J.A. Curry, 1999, Tropical ice water amount and its relations to other atmospheric hydrological parameters as inferred from satellite data, *J. Appl. Meteorol.*, **38**, 1182–1194.

Liu, G. and J.A. Curry, 2000, Determination of ice water path and mass median particle size using multichannel microwave measurements, American Meteorological Soc., **39,** 1318–1329.

Liu, G., 2004, Approximation of single scattering properties of ice and snow for high microwave frequencies, *J. Atmos. Sci.*, **61**, 2441–2456.

Liu, C., E. Zipser, T. Garrett, J.H. Jiang, and H. Su, 2007, How do the water vapor and carbon monoxide "tape recorders" start near the tropical tropopause?, *Geophys. Res. Lett.*, **32**, L09804, doi:10.1029/2006GL029234.

Livesey, N.J., M.J. Filipiak, L. Froidevaux, W.G. Read, A. Lambert, M.L. Santee, J.H. Jiang, H.C. Pumphrey, J.W. Waters, R.E. Cofield, D.T. Cuddy, W.H. Daffer, B.J. Drouin, R.A. Fuller,

R.F. Jarnot, Y.B. Yiang, B.W. Knosp, Q.B. Li, V.S. Perun, M.J. Schwartz, W.V. Snyder, P.C. Stek, R.P. Thurstans, P.A. Wagner, M. Avery, E.V. Browell, J.-P Cammas, L.E. Christensen, G.S. Diskin, R.-S. Gao, H.-J-. Jost, M. Loewenstein, J.D. Lopez, P. Nedelec, G.B. Osterman, G.W. Sachse, C.R. Webster, 2008, Validation of Aura Microwave Limb Sounder O_3 and CO observations in the upper troposphere and lower stratosphere, *J. Geophys. Res.*, **113**, D15S02, doi:10.1029/2007JD008805.

Luntama, J.-P., G. Kirchengast, M. Borsche, U. Foelsche, S. Steiner, S. Healy, A. von Engeln, E. O'Clerigh, and C. Marquardt, 2008, Prospects of the EPS GRAS Mission for Operational Atmospheric Applications. *Bull. Amer. Meteor. Soc.*, **89**, 1863–1875.

Macpherson, S.R., G. Deblonde, J.M. Aparicio, and B. Casati, 2008, Impact of NOAA ground-based GPS observations on the Canadian regional analysis and forecast system. *Mon. Wea. Rev.*, **136**, 2727–2746.

Madden, R.A., and P.R. Julian, 1971, Detection of a 40–50 day oscillation in the zonal wind in the tropical Pacific, *J. Atmos. Sci.*, **28**, 702–708.

Madden, R.A., and P.R. Julian, 1994, Observations of the 40–50 day tropical oscillation – A review, *Mon. Weather. Rev.*, **122**, 814–837.

Manning, W., and J.R. Wang, 2003, Retrieval of precipitable water using Special Sensor Micro-wave/Temperature-2 (SSM/T-2) millimeter-wave radiometric measurements, *Radio Sci.*, 38, 1097, doi:10.1029/2002RS002735.

Marzano, F.S., A. Mugnai, G. Panegrossi, N. Pierdicca, E.A. Smith, and J. Turk, 1999, Bayesian estimation of precipitating cloud parameters from combined measurements of spaceborne microwave radiometer and radar. IEEE Trans. Geosci. Remote Sensing, **37**, 596–613.

Matricardi, M., F. Chevallier, G.A. Kelly, and J.-N. Thépaut, 2004, An improved general fast radiative transfer model for the assimilation of radiance observations, *Q. J. R. Meteorol. Soc.*, **130**, 153–173.

Mätzler, 2002, C., MATLAB functions for Mie scattering and absorption - Version 2, Tech. Rep. 2002–11, Universität Bern.

Mätzler, C. (Ed.), 2006, Thermal microwave radiation: Applications for remote sensing, IET Electromagnetic Waves Series, The Institution of Engineering and Technology, London, ISBN 0-86341-573-3, 555pp.

Meeks, M.L., 1961, Atmospheric emission and opacity at millimeter wavelengths due to oxygen, J. Geophys. Res., **66**, 3749–3757.

Meirold-Mautner, I., C. Prigent, E. Defer, J.-R. Pardo, J.-P. Chaboureau, J.-P. Pinty, M. Mech and S. Crewell, 2007, Radiative transfer simulations using mesoscale cloud model outputs: comparisons with passive microwave and infrared satellite observations for mid-latitudes, *J. Atmos. Sc.*, **64,** 1550–1568.

Melsheimer, C., C. Verdes, S.A. Buehler, C. Emde, P. Eriksson, D.G. Feist, S. Ichizawa, V.O. John, Y. Kasai, G. Kopp, N. Koulev, T. Kuhn, O. Lemke, S. Ochiai, F. Schreier, T.R. Sreerekha, M. Suzuki, C. Takahashi, S. Tsujimaru and J. Urban, 2005, Intercomparison of General Purpose Clear Sky Atmospheric Radiative Transfer Models for the Millimeter/Submillimeter Spectral Range, Radio Sci., 40, R**S1007**, doi:10.1029/2004RS003110.

Meneghini, R.J., J. Eckerman, and D. Atlas, 1983, Determination of rain rate from a spaceborne radar technique. IEEE Trans. Geosci. Rem Sens., **2**1, 34–43.

Meneghini, R., and T. Kozu, 1990, Spaceborne Weather Radar. Artech House, 199pp.

Meneghini, R., T. Iguchi, T. Kozu, L. Liao, K. Okamoto, J. Jones, and J. Kwiatkowski, 2000, Use of the surface reference technique for path attenuation estimates from the TRMM Precipitation Radar. J. Appl. Meteor., **39**, 2053–2070.

Minnis P., J. Huang, B. Lin, Y. Yi, R.F. Arduini, T.-F. Fan, J.K. Ayers, G.G. Mace, 2007, Ice cloud properties in ice-over-water cloud systems using Tropical Rainfall Measuring Mission (TRMM) visible and infrared scanner and TRMM Microwave Imager data, J. Geophys. Res., **112**, D06206, doi:10.1029/2006JD007626.

Mishchenko, M.I., L.D. Travis, and A.A. Lacis, 2002, Scattering, Absorption and Emission of Light by Small Particles, Cambridge University Press, Cambridge. ISBN 0-521-78252

Mitrescu,C., S. Miller, G Hawkins, T. L'Ecuyer, J. Turk, P. Partain and G. Stephens, 2008, Near real time applications of CloudSat data, J. App. Met., **47**, 1982–1994.

Mohr, K.I., J.S. Famiglietti and E.J. Zipser, 1999, The contribution to tropical rainfall with respect to convective system type, size, and intensity estimated from the 85-GHz ice-scattering signature, J. Appl. Meteorol., **38**, 596–606.

Moreau E., P. Bauer and F. Chevallier, 2003, Variational retrieval of rain profiles from spaceborne passive microwave radiance observations, J. Geophys. Res., **108**(D16), 4521, doi:10.1029/2002JD003315.

Mote, P.W., K.H. Rosenlof, J.R. Holton, R.S. Harwood, and J.W. Waters, 1995, Seasonal variation of water vapour in the tropical lower stratosphere, Geophys. Res. Lett., **22**, 1093–1096.

Mote, P. W., K.H. Rosenlof, M.E. McIntyre, E.S. Carr, J.C. Gille, J.R. Holten, J.S. Kinnersley, H.C. Pumphrey, J.M. Russell III, J.W. Waters, 1996, An atmospheric tape recorder: the imprint of tropical tropopause temperatures on stratospheric water vapor, J. Geophys. Res., **101**, 3989–4006.

Mote, P.W., H.L. Clark, T.J. Dunkerton, R.S. Harwood, and H.C. Pumphrey, 2000, Intraseasonal variations of water vapor in the tropical upper troposphere and tropopause region, J. Geophys. Res., **105**, 17457–17470.

Mugnai, A., and E.A. Smith, 1984, Passive microwave radiation transfer in an evolving cloud medium. IRS-84: Current Problems in Atmospheric Radiation, Proceedings of the IAMAP International Radiation Symposium (G. Fiocco, editor), ISBN 0-937194-08-5, A. Deepak Publishing, Hampton, VA, 297–300.

Mugnai, A., and E.A. Smith, 1988: Radiative transfer to space through a precipitating cloud at multiple microwave frequencies. Part I: Model description. *J. Appl. Meteor.*, **27**, 1055–1073.

Mugnai, A., H.J. Cooper, E.A. Smith and G.J. Tripoli, 1990, Simulation of microwave brightness temperatures of an evolving hail storm at the SSM/I frequencies. Bull. Amer. Meteor. Soc., **71**, 2–13.

Mugnai, A., E.A. Smith and G.J. Tripoli, 1993, Foundation for statistical-physical precipitation retrieval from passive microwave satellite measurements. Part 1: Emission source and generalized weighting function properties of a time dependent cloud-radiation model, J. Appl. Meteorol., **32**, 17–39.

Mugnai, A., S. Di Michele, E.A. Smith, F. Baordo, P. Bauer, B. Bizzarri, P. Joe, C. Kidd, F.S. Marzano, A. Tassa, J. Testud, and G.J. Tripoli, 2007, Snowfall measurements by proposed European GPM mission. Measuring Precipitation from Space: EURAINSAT and the Future (V. Levizzani, P. Bauer, and F.J. Turk, eds.), Advances in Global Change Research (Vol. 28), Springer, Dordrecht, Netherlands, 655–674.

Mugnai, A., E.A. Smith, G.J. Tripoli, S. Dietrich, V. Kotroni, K. Lagouvardos, and C.M. Medaglia, 2008, Explaining discrepancies in passive microwave cloud-radiation databases in microphysical context from two different cloud-resolving models. Meteor. Atmos. Phys., **101**, 127–145, doi 10.1007/s00703-007-0281-4, 19 pp.

Murtagh, D., U. Frisk, F. Merino, M. Ridal, A. Jonsson, J. Stegman, G. Witt, P. Eriksson, C. Jiménez, G. Megie, J. de la Noö, P. Ricaud, P. Baron, J.R. Pardo, A. Hauchcorne, E.J. Llewellyn, D.A. Degenstein, R.L. Gattinger, N.D. Lloyd, W.F.J. Evans, I.C. McDade, C.S. Haley, C. Sioris, C. von Savigny, B.H. Solheim, J.C. McConnell, K. Strong, E.H. Richardson, G.W. Leppelmeier, E. Kyrölä, H. Auvinen, L. Oikarinenh, 2002, An overview of the Odin atmospheric mission, Can. J. Phys., **80**, 309–319.

Nakamura, K., K. Okamoto, T. Ihara, J. Awaka, and T. Kozu, 1990, Conceptual design of rain radar for the Tropical Rainfall Measuring Mission. Int. J. Sat. Comm., **8,** 257–268.

Nesbitt, S.W., E.J. Zipser and D.J. Cecil, 2000, A census of precipitation features in the tropics using TRMM: radar, ice scattering, and lightning observations, J. Clim., **13**, 4087–4106.

Okamoto, K., J. Awaka, and T. Kozu, 1988, A feasibility study of rain radar for the Tropical Rainfall Measuring Mission 6: A case study of rain radar system. J. Comm. Research Lab., **35**, 183–208.

Okamoto, K., and T. Kozu, 1993, TRMM Precipitation Radar algorithms. Proc. IGARSS'93, IEEE Trans Geosci Remote Sens, **31**, 426–428.

Okamoto, K., 2003, A short history of the TRMM Precipitation Radar. AMS Meteorological Monographs: Cloud Systems, Hurricanes, and the Tropical Rainfall Measuring Mission (TRMM) - A Tribute to Dr. Joanne Simpson, **29**, 187–195.

Okamoto, K., and S. Shige, 2008, TRMM precipitation radar and its observation results (in Japanese). IEICE Trans. Commun., **J91-B**, 723–733.

Olson, W.S., Y. Hong, C.D. Kummerow, and J. Turk, 2001, A texture-polarization method for estimating convective - stratiform precipitation area coverage from passive microwave radiometer data. *J. Appl. Meteorol.*, **40**, 1577–1591.

Olson, W.S., C.D. Kummerow, S. Yang, G.W. Petty, W.-K. Tao, T.L. Bell, S.A. Braun, Y. Wang, S.E. Lang, D.E. Johnson, and C. Chiu, 2006, Precipitation and latent heating distributions from satellite passive microwave radiometry. Part I: Improved method and uncertainties. *J. Appl. Meteor. Climatol.*, **45**, 702–720.

Ossenkopf, V., 2008, The stability of spectroscopic instruments: a unified Allan variance computation scheme, Astronony & Astrophysics **479**(3), 915–926, DOI: 10.1051/0004-6361:20079188

Panegrossi G., S. Dietrich, F.S. Marzano, A. Mugnai, E.A. Smith, X. Xiang, G.J. Tripoli, P.K. Wang, J.P.V. Poiares Baptista, 1998, Use of cloud model microphysics for passive microwave-based precipitation retrieval: Significance of consistency between model and measurement manifolds. *J. Atmos. Sci.*, **55**, 1644–1673.

Pardo, J.R., J. Cernicharo, and E. Serabyn, 2001, Atmospheric Transmission at Microwaves (ATM): An improved model for mm/submm applications, IEEE Trans. on Antennas and Propagation, **49(12)**, 1683–1694.

Phalippou, L., 1996, Variational retrieval of humidity profile, wind speed and cloud liquid water path with the SSM/I: Potential for numerical weather prediction, *Q. J. Roy. Meteorol. Soc.*, **122**, 327–355.

Pickett, H.M., R.L. Poynter, E.A. Cohen, M.L. Delitsky, J.C. Pearson, and H.S.P. Müller, 2001, Submillimeter, millimeter, and microwave spectral line catalog, Tech. rep., Jet Propulsion Laboratory.

Poli, P., P. Moll, F. Rabier, G. Desroziers, B. Chapnik, L. Berre, S.B. Healy, E. Andersson, and F.-Z. El Guelai, 2007, Forecast impact studies of zenith total delay data from European near real-time GPS stations in Météo France 4DVAR. *J. Geophys. Res.*, **112**, D06114, doi:10.1029/2006JD007430.

Poli, P., P. Moll, D. Puech, F. Rabier, and S. Healy, 2009, Quality control, error analysis, and impact assessment of {FORMOSAT-3/COSMIC} in numerical weather prediction. Terr. Atmos. Ocean, **20**, 101–113.

Posselt, D., G.L. Stephens, and M. Miller, 2008, CloudSat: Adding a new dimension to a classical view of extratropical cyclones. Bull. Amer. Met. Soc., **89**, 599–609.

Prabhakara, C., G. Dalu, G.L. Liberti, J.J. Nucciarone and R. Suhasini, 1992, Rainfall estimation over oceans from SMMR and SSM/I microwave data, *J. Appl. Meteorol.*, **31**, 532–552.

Prigent, C., A. Sand, C. Klapisz and Y. Lemaitre, 1994, Physical retrieval of liquid water contents in a North Atlantic cyclone using SSM/I data, *Q. J. R. Meteorol. Soc.*, **120**, 1179–1207.

Prigent, C. and W.B. Rossow, 1999, Retrieval of surface and atmospheric parameters over land from SSM/I: Potential and limitations, Q. J. Roy. Meteorol. Soc., **125**, 2379–2400.

Prigent, C., E. Defer, J. Pardo, C. Pearl, W.B. Rossow and J.-P. Pinty, 2005, Relations of polarized scattering signatures observed by the TRMM Microwave Instrument with electrical processes in cloud systems, Geophys. Res. Lett., **32**, L04810, doi: 10.1029/2004GL022225.

Prigent, C., J. Pardo, and B. Rossow, 2006, Comparisons of the millimeter and submillimeter bands for atmospheric temperature and water vapor soundings for clear and cloudy skies, *J. Appli. Meteorol. Climat.*, **45**, 1622–1633.

Pumphrey, H.C., D. Rind, J.M. Russell, III, and J.E. Harries, 1998, A preliminary zonal mean climatology of water vapour in the stratosphere and mesosphere, Adv. Space. Res., **21**, 1417–1420.

Pumphrey, H.C., C. Boone, K.A. Walker, P. Bernath, and N.J. Livesey, 2008, The tropical tape recorder observed in HCN, *Geophys. Res. Lett.* **35**, L05801, doi:10.1029/2007GL032137.

Rau, G., R.Schieder, B.Vowinkel, 1984, Characterization and Measurement of Radiometer Stability, Proc. 14th European Microwave Conf., Sept. 10–13, Liege, Belgium, 248–253

Racette,P., R.F. Adler, J.R. Wang, A.J. Gasiewski, D.M. Jackson and D.S. Zacharias, 1996, An airborne millimeter-wave imaging radiometer for cloud, precipitation, and atmospheric water vapor studies, *J. Appl. Oceanic Technol.*, **13**, 610–619.

Read, W.G., J.W. Waters, D.A. Flower, L. Froidevaux, R.F. Jarnot, D.L. Hartman, R.S. Harwood, and R.B. Rood, 1995, Upper–tropospheric water vapor from UARS MLS, Bull. Amer. Meteorol. Soc., **76**, 2381–2389.

Read, W.G., J.W. Waters, D.L. Wu, E.M. Stone, Z. Shippony, A.C. Smedley, C.C. Smallcomb, S. Oltmans, D. Kley, H.G.J. Smit, J.L. Mergenthaler, M.K. Karki, 2001, UARS Microwave Limb Sounder upper tropospheric humidity measurement: Method and validation, *J. Geophys. Res.*, **106**, 32207–32258.

Read, W.G., D.L. Wu, J.W. Waters, and H.C. Pumphrey, 2004a, A new 147-56 hPa water vapor product from the UARS Microwave Limb Sounder, *J. Geophys. Res.*, **109**, D06111.

Read, W.G., D.L. Wu, J.W. Waters, and H.C. Pumphrey, 2004b,Dehydration in the tropical tropopause layer: Implications from UARS MLS, *J. Geophys. Res.*, **109,** D06110, doi:10.1029/2003JD004056.

Read, W.G., Z. Shippony, M.J. Schwartz, N.J. Livesey and W.V. Snyder, 2006, The clear-sky unpolarized forward model for the EOS Microwave Limb Sounder (MLS), IEEE Trans. Geosci. Remote Sens., **44**(5), 1367–1379.

Read, W.G., A. Lambert, J. Bacmeister, R.E. Cofield, L.E. Christensen, D.T. Cuddy, W.H. Daffer, B.J. Drouin, E. Fetzer, L. Froidevaux, R. Fuller, R. Herman, R.F. Jarnot, J.H. Jiang, Y.B. Jiang, K. Kelly, B.W. Knosp, H.C. Pumphrey, K.H. Rosenlof, X. Sabounchi, M.L. Santee, M.J. Schwartz, W.V. Snyder, P.C. Stek, H. Su, L.L. Takacs, R.P. Thurstans, H. Vomel, P.A. Wagner, J.W. Waters, C.R. Webster, E.M. Weinstock, and D.L. Wu, 2007, EOS Aura Microwave Limb Sounder upper tropospheric and lower stratospheric humidity validation, *J. Geophys. Res.*, **112**, D24S35, doi:10.1029/2007JD008752.

Read, W.G., M.J. Schwartz, A. Lambert, H. Su, N.J. Livesey, W.H. Daffer, and C.D. Boone, 2008, The roles of convection, extratropical mixing, and *in situ* freeze-drying in the tropical tropopause layer, Atmos. Chem. Phys. Discus., **8**, 3961–4000.

Ricaud, P., B. Barret, J.L. Attié, E.L. Flochmoën, H. Teyssèdre, V.H. Peuch, N. Livesey, A. Lambert, and J.P. Pommerau, 2007, Impact of land convection on troposphere-stratosphere exchange in the tropics, Atmos. Chem. Phys., **7**, 5639–5657.

Rocken, C., R. Anthes, M. Exner, D. Hunt, S. Sokolovsky, R. Ware, M. Gorbunov, W. Schreiner, D. Feng, B. Herman, Y.-H. Kuo, and X. Zou, 1997, Analysis and validation of {GPS/MET} data in the neutral atmosphere. J. Geophys. Res., **102**, 29849–29866.

Rodgers, C., 1976, Retrieval of atmospheric temperature and composition from remote measurements of thermal radiation, Rev. Geophys., **14**, 609–624.

Rodgers, C., 1990, Characterization and error analysis of profiles retrieved from remote sounding measurements, J. Geophys. Res., **95**, 5587–5595.

Rodgers, C., 2000, Inverse methods for atmospheric sounding: Theory and Practice, World Scientific.

Rosenkranz, P.W., 1993, Absorption of microwaves by atmospheric gases, in Atmospheric remote sensing by microwave radiometry, edited by M. A. Janssen, pp. 37–90, John Wiley & Sons, Inc.

Rosenkranz, P.W., K.D. Hutchinson, K.R. Hardy, and M.S. Davis, 1997, An assessment of the impact of satellite microwave sounder incidence angle and scan geometry on the accuracy of atmospheric temperature profile retrievals, J. Atmos. Ocean. Tech., **14**, 488–494.

Rosenkranz, P.W., 1998, Water vapor microwave continuum absorption: A comparison of measurements and models, Radio Sci., **33**, 919–928.

Rossow, W.B. and R.A. Schiffer, 1999, Advances in understanding clouds from ISCCP, Bull. Amer. Meteorol. Soc., **80**, 2261–2287.

Rothman, L.S., D. Jacquemart, A. Barbe, D.C. Benner, M. Birk, L.R. Brown, M.R. Carleer, C. Chackerian Jr, K. Chance, L.H. Coudert, V. Dana, V.M. Davi, J.-M. Flaud, R.R. Gamache,

A. Goldman, J.-M. Hartmann, K.W. Jucks, A.G. Maki, J.-Y. Mandin, S.T. Masie, J. Orphal, A. Perrin, C.P. Rinsland, M.A.H. Smith, J. Tennyson, R.N. Tolchenov, R.A. Toth, J.V. Auwera, P. Varanasi, G. Wagner, 2005, The HITRAN 2004 molecular spectroscopic database, J. Quant. Spectrosc. Radiat. Transfer, **96**, 139–204.

Santee, M.L., A. Lambert, W.G. Read, N.J. Livesey, R.E. Cofield, D.T. Cuddy, W.H. Daffer, B.J. Drouin, L. Froidevaux, R.A. Fuller, R.F. Jarnot, B.W. Knosp, G.L. Manney, V.S. Perun, W.V. Snyder, P.C. Stek, R.P. Thurstans, P.A. Wagner, J.W. Waters, G. Muscari, R.L. de Zafra, J.E. Dibb, D.W. Fahey, P.J. Popp, T.P. Marcy, K.W. Jucks, G.C. Toon, R.A. Stachnik, P.F. Bernath, C.D. Boone, K.A. Walker, J. Urban, D. Murtagh, 2007, Validation of the Aura Microwave Limb Sounder HNO$_3$ measurements, J. Geophys. Res., **112**, D24S40, doi: 10.1029/2007JD008721.

Saunders, R., M. Matricardi, and P. Brunel, 1999, An improved fast radiative transfer model for assimilation of satellite radiance, *Q. J. R. Meteorol. Soc.*, **125**, 1407–1425.

Schaerer, G., and T. T. Wilheit, 1979, A passive microwave technique for profiling of atmospheric water vapor, Radio Sci., **14**, 371–375.

Schoeberl, M.R., B.N. Duncan, A.R. Douglass, J.W. Waters, N.J. Livesey, W.G. Read, and M.J. Filipiak, 2006, The carbon monoxide tape recorder, Geophys. Res. Lett., **33**, L12811, doi: 10.1029/2006GL026178.

Scipal, K., M. Drusch, W. Wagner, 2008, Assimilation of a ERS scatterometer derived soil moisture index in the ECMWF numerical weather prediction system. Adv. Water Resources, **31,** 1101–1112.

Seuffert, G., H. Wilker, P. Viterbo, J.-F. Mahfouf, M. Drusch, and J.-C. Calvet, 2003, Soil moisture analysis combining screen-level parameters and microwave brightness temperatures: A test with field data. Geophys. Res. Lett., **30**, 1498, doi:10.1029/2003GL017128.

Simpson, J., R.F. Adler, and G. North, 1988, A Proposed Tropical Rainfall Measuring Mission (TRMM) satellite. Bull. Amer. Meteor. Soc., **69**, 278–295.

Simpson, J., and W.-K. Tao, 1993, The Goddard Cumulus Ensemble Model. Part II: Applications for studying cloud precipitating processes and for NASA TRMM. Terrestrial, Atmospheric and Oceanic Sciences, **4**, 73–116.

Simpson, J., C. Kummerow, W.-K. Tao, and R.F. Adler, 1996, On the Tropical Rainfall Measuring Mission (TRMM) satellite. *Meteorol. Atmos. Phys.*, **60**, 19–36.

Skofronick-Jackson, G.M., J.R. Wang, G.M. Heymsfield, R. Hood, W. Manning, R. Meneghini and J.A. Weinman, 2003, Combined radiometer-radar microphysical profile estimations with emphasis on high frequency brightness temperature observations, *J. Appl. Meteorol.*, **42**, 476–487.

Skofronick-Jackson G., A. Heymsfield, E. Holthaus, C. Albers, and M.-J. Kim, 2008, Nonspherical and spherical characterization of ice in Hurricane Erin for wideband passive microwave comparisons, *J. Geophys. Res.*, **113**, D06201, doi:10.1029/2007JD008866.

Smith, E.A., and A. Mugnai, 1988, Radiative transfer to space through a precipitating cloud at multiple microwave frequencies. Part II: Results and analysis. *J. Appl. Meteor.*, **27**, 1074–1091.

Smith, E.A., and A. Mugnai, 1989, Radiative transfer to space through a precipitating cloud at multiple microwave frequencies. Part III: Influence of large ice particles. *J. Meteor. Soc. Japan*, **67**, 739–755.

Smith, E.A., X. Xiang, A. Mugnai, and G. Tripoli, 1992a, A cloud radiation model for spaceborne precipitation retrieval. Extended Abstract Vol. of International TRMM Workshop on the Processing and Utilization of the Rainfall Data Measured from Space, Communications Research Laboratory, Tokyo, Japan, 273–283.

Smith, E.A., A. Mugnai, H.J. Cooper, G.J. Tripoli, and X. Xiang, 1992b, Foundations for statistical - physical precipitation retrieval from passive microwave satellite measurements. Part I: Brightness temperature properties of a time dependent cloud - radiation model. *J. Appl. Meteor.*, **31**, 506–531.

Smith, E.A., C. Kummerow, and A. Mugnai, 1994a, The emergence of inversion-type profile algorithms for estimation of precipitation from satellite passive microwave measurements. Remote Sensing Reviews, **11**, 211–242.

Smith, E.A., X. Xiang, A. Mugnai, and G.J. Tripoli, 1994b, Design of an inversion-based precipitation profile retrieval algorithm using an explicit cloud model for initial guess microphysics. Meteorol. Atmos. Phys., **54**, 53–78.

Smith, E.A., Z. Haddad, and C. Kummerow, 1995a, Overview on TRMM combined algorithm development. In: J. Simpson & C. Kummerow (eds) Contribution to TRMM Science Operations Plan, Florida State University, Tallahassee, FL, pp65.

Smith, E.A., A. Mugnai, and G. Tripoli, 1995b, Theoretical foundations and verification of a multispectral, inversion-type microwave precipitation profile retrieval algorithm. In Passive Microwave Remote Sensing of Land-Atmosphere Interactions (599–621), VSP Press, Utrecht - The Netherlands, 685 pp.

Smith, E.A., J. Turk, M. Farrar, A. Mugnai, and X. Xiang, 1997, Estimating 13.8 GHz path integrated attenuation from 10.7 GHz brightness temperatures for TRMM combined PR-TMI precipitation algorithm. *J. Appl. Meteor.*, **36**, 365–388.

Smith, E.A., P. Bauer, F. S. Marzano, C. D. Kummerow, D. McKague, A. Mugnai, G. Panegrossi, 2002, Intercomparison of microwave radiative transfer models for precipitating clouds, IEEE Trans Geosci. Remote Sens., **40**, 541–549.

Smith, E.A., and T.D. Hollis, 2003, Performance evaluation of level 2 TRMM rain profile algorithms by intercomparison and hypothesis testing. AMS Meteorological Monographs: Cloud Systems, Hurricanes, and the Tropical Rainfall Measuring Mission (TRMM) – A Tribute to Dr. Joanne Simpson, **29**, 207–222.

Smith, E.A., G. Asrar, Y. Furuhama, A. Ginati, A. Mugnai, K. Nakamura, R.F. Adler, M.-D. Chou, M. Desbois, J.F. Durning, F. Einaudi, J.K. Entin, R.R. Ferraro, R. Guzzi, P.R. Houser, P.H. Hwang, T. Iguchi, P. Joe, R. Kakar, J.A. Kaye, M. Kojima, C.D. Kummerow, K.-S. Kuo, D.P. Lettenmaier, V. Levizzani, N. Lu, A.V. Mehta, C. Morales, P. Morel, T. Nakazawa, S.P. Neeck, K. Okamoto, R. Oki, G. Raju, J.M. Shepherd, J. Simpson, B.-J. Sohn, E.F. Stocker, W.-K. Tao, J. Testud, G.J. Tripoli, E.F. Wood, S. Yang, and W. Zhang, 2007, International Global Precipitation Measurement (GPM) Program and Mission: An overview. Measuring Precipitation from Space: EURAINSAT and the Future. In: V. Levizzani, P. Bauer, and F.J. Turk, (eds.), Advances in Global Change Research, Vol. 28, Springer, Dordrecht, Netherlands, 611–653.

Sokolovskiy, S., Y.-H. Kuo, and W. Wang, 2005, Assessing the accuracy of a linearized observation operator for assimilation of radio occultation data: Case simulations with a high-resolution weather model. Mon. Wea. Rev., **133**, 2200–2212.

Sorooshian S., X. Gao, K. Hsu, R.A. Maddox, Y. Hong, H.V. Gupta and B. Imam, 2002, Diurnal Variability of Tropical Rainfall Retrieved from Combined GOES and TRMM Satellite Information. J. Clim., **15**, 983–1001.

Spencer, R.W., B.B. Hinton and W.S. Olson, 1983, Nimbus-7 37 GHz radiances correlated with radar rain rates over the Gulf of Mexico, *J. Appl. Meteorol. Climatol.*, **22**, 2095–2099.

Spencer, R.W., H.M. Goodman and R.E. Hood, 1989, Precipitation retrieval over land and ocean with the SSM/I: identification and characteristics of the scattering signal. J. Atmos. Oceanic Tech., **6**, 254–273.

Sreerekha, T.R., C. Emde, N. Courcoux, C. Teichmann, S.A. Buehler, U. Loehnert, M. Mech, S. Crewell, A. Battaglia, P. Eriksson, B. Rydberg, C. Davis, C. Jimenez, S. English and A. Doherty (2006), Development of an RT model for frequencies between 200 and 1000 GHz, Final Report, ESTEC Contract No 17632/03/NL/FF.

Staelin, D.H., K.F. Kunzi, R.L. PettyJohn, R.K.L. Poon and R.W. Wilcox, 1976, Remote sensing of atmospheric water vapor and liquid water with the Nimbus-5 microwave spectrometer, *J. Appl. Meteorol.*, **15**, 1204–1214.

Staelin, D.H. and F. W. Chen, 2000, Precipitation observations near 54 and 183 GHz using the NOAA-15 satellite," IEEE Trans. Geosci. Remote Sens., **38(5)**, 2322–2332.

Staelin D.H., and C. Surussavadee, 2007, Precipitation Retrieval Accuracies for Geo-Microwave Sounders, IEEE Trans. Geosci. Remote Sens., **45**, 3150–3159.

Stephens, G.L. and T.J. Greenwald, 1991, The Earth's radiation budget in relation to atmospheric hydrology: 2 Observations of cloud effects, *J. Geophys. Res.*, **96**, 15,325–15,340.

Stephens, G.L., D.G. Vane, R.J. Boain, G.G. Mace, K. Sassen, Z. Wang, A.J. Illingworth, E. J. O'Connor, W.B. Rossow, S.L. Durden, S.D. Miller, R.T. Austin, A. Benedetti, C. Mitrescu, and the CloudSat Science Team, 2002, The CloudSat mission and the A-TRAIN: A new dimension to space-based observations of clouds and precipitation. Bull. Am. Met. Soc., **83**, 1771–1790.

Stephens, G.L, D.G. Vane, S. Tanelli, E. Im, S. Durden, M. Rokey, D. Reinke, P. Partain, G.G. Mace, R. Austin, T. L'Ecuyer, J. Haynes, M. Lebsock, K. Suzuki, D. Waliser, D. Wu, J. Kay, A. Gettelman, Z. Wang, R. Marchand, 2008, The CloudSat Mission: Performance and early science after the first year of operation, *J. Geophys. Res.*, **113**, D00A18, doi:10.1029/ 2008JD009982.

Stohl, A., S. Eckhardt, C. Forster, P. James, and N. Spichtinger, 2002, On the pathways and timescales of intercontinental air pollution transport, *J. Geophys. Res.*, **107**, 4684, doi:10.1029/ 2001JD001396.

Stone, E.M., W.J. Randel, J.L. Stanford, W.G. Read, and J.W. Waters, 1996, Baroclinic wave variations observed in MLS upper tropospheric water vapour, Geophys. Res. Lett., **23**, 2967–2970.

Stubenrauch, C.J., A. Chédin, G. Rädel, N.A. Scott and S. Serrar, 2006, Cloud properties and their seasonal and diurnal variability from TOVS Path-B, J. Clim., **19**, 5531–5553.

Su, H., W.G. Read, J.H. Jiang, J.W. Waters, D.L. Wu, and E.J. Fetzer, 2006, Enhanced positive water vapor feedback associated with tropical deep convection: New evidence from Aura MLS, Geophys. Res. Lett., **33**, 5709, doi:10.1029/2005GL025505.

Surussavadee C. and D.H. Staelin, 2008 a, Global Millimeter-Wave Precipitation Retrievals Trained with a Cloud-Resolving Numerical Weather Prediction Model, Part I: Retrieval Design, IEEE Trans. Geosci. Remote Sens., **46**, 99–108.

Surussavadee, C. and D.H. Staelin, 2008b, Global Millimeter-Wave Precipitation Retrievals Trained with a Cloud-Resolving Numerical Weather Prediction Model, Part II: Performance Evaluation, IEEE Trans. Geosci. Remote Sens., **46**, 109–118.

Tan, D.G.H., E. Andersson, M. Fisher, and I. Isaksen, 2007, Observing-system impact assessment using a data assimilation ensemble technique: application to the ADM-Aeolus wind profiling mission. *Quart. J. Roy. Meteorol. Soc.*, **133**, 381–390.

Tanelli, S., S.L. Durden, E. Im, K. Pak, D. Reinke, P. Partain, J. Haynes, R. Marchand, 2008, CloudSat's Cloud Profiling Radar after 1 year in orbit: performance, external calibration, and processing, IEEE Trans. Geosc. and Rem. Sens., **46**, 3560–3573.

Tao, W.-K., and J. Simpson, 1993, The Goddard Cumulus Ensemble Model. Part I: Model description. Terrestrial, Atmospheric and Oceanic Sciences, **4**, 35–72.

Tapiador F.J., C. Kidd, V. Levizzani, F.S. Marzano, 2004, A neural networks-based fusion technique to estimate half-hourly rainfall estimates at $0.1°$ resolution from satellite passive microwave and infrared data, J. Appl. Meteor., **43**, 576–594.

Tassa A., S. Di Michele, A. Mugnai, F.S. Marzano, J.P.V. Poiares Baptista, 2003, Cloud model–based Bayesian technique for precipitation profile retrieval from the Tropical Rainfall Measuring Mission Microwave Imager, Radio Sci., **38**, doi:10.1029/2002RS002674.

Tesmer, J.R., and T.T. Wilheit, 1998, An improved microwave radiative transfer model for tropical oceanic precipitation. *J. Atmos. Sci.*, 55, 1674–1689.

Tiuri, M.E., 1966, Radio-Telescope Receivers, pp 236 – 293 in, J.D. Kraus Radio Astronomy, McGraw-Hill Book Company, New York.

Tripoli, G.J., 1992, A nonhydrostatic model designed to simulate scale interaction. Mon. Wea. Rev., **120**, 1342–1359.

Turner D.D., A.M. Vogelmann, R.T. Austin, J.C. Barnard, K. Cady-Pereira, J.C. Chiu, S.A. Clough, C. Flynn, M.M. Khaiyer, J. Liljegren, K. Johnson, B. Lin, C. Long, A. Marshak, S.Y. Matrosov, S.A. McFarlane, M. Miller, Q. Min, P. Minnis, W. O'Hirok, Z. Wang, and W. Wiscombe, 2007,

Thin liquid water clouds: Their importance and our challenge, Bull. Am. Meteorol. Soc., **88,** 177–190.

Ulaby F.T., R.K. Moore, A.K. Fung, 1981, Microwave remote sensing, active and passive, Vol. 1, Artech House Publishers.

Uppala, S., P. Kållberg, A. Hernandez, S. Saarinen, M. Fiorino, X. Li, K. Onogi, N. Sokka, U. Andrae and V. Da Costa Bechtold, 2004, ERA-40: ECMWF 45-year reanalysis of the global atmosphere and surface conditions 1957–2002, ECMWF Newsletter, **101**, 2–21.

Vaneck, M.D., I.G. Nolt, N.D. Tappan, P.A.R. Ade, F.C. Gannaway, P.A. Hamilton, C. Lee, J.E. Davis and S. Predko, 2001, Far-infrared sensor for cirrus (FIRSC): an aircraft-based Fourier-transform spectrometer to measure cloud radiance, Appl. Optics, **40**, 2169–2176.

Vedel, H. and K. Sattler, 2006, Comparison of TOUGH impact studies with ground-based GPS observations. TOUGH Project Rep. D49, 18 pp. Available online at http://web.dmi.dk/pub/ tough/deliverables/d49-compare-results.pdf.

Vowinkel, B., 1988, Passive Mikrowellenradiometrie, Vieweg, ISBN 3-528-08959-8

Wang, J.R., P. Racette, J.D. Spinhirne, K.F. Evans and W.D. Hart, 1998, Observations of cirrus clouds with airborne MIR, CLS, and MAS during SUCCESS, Geophys. Res. Lett., **25**, 1145–1148.

Wang, Y., Y. Choi, T. Zeng, B. Ridley, N. Blake, D. Blake, and F. Flocke, 2006, Late-spring increase of trans-Pacific pollution transport in the upper troposphere, Geophys. Res. Lett., **33**, L01811, doi:10.1029/2005GL024975.

Waters, J.W., K.F. Kunzi, R.L. PettyJohn, R.K.L. Poon, and D.H. Staelin, 1975, Remote sensing of atmospheric temperature profiles with the Nimbus 5 microwave spectrometer, J. Atmos. Sci., **32**, 1953–1969.

Waters, J.W., W.G. Read, L. Froidevaux, R.F. Jarnot, R.E. Cofield, D.A. Flower, G.K. Lau, H.M. Pickett, M.L. Santee, D.L. Wu, M.A. Boyles, J.R. Burke, R.R. Lay, M.S. Loo, N.J. Livesey, T.A. Lungu, G.L. Manney, L.L. Nakamura, V.S. Perun, B.P. Ridenoure, Z. Shippony, P.H. Siegel, and R.P. Thurstans, R.S. Harwood, H.C. Pumphrey, and M.J. Filipiak, 1999, The UARS and EOS Microwave Limb Sounder (MLS) experiments, J. Atmos. Sci., **56**, 194–217.

Waters, J.W., L. Froidevaux, R.S. Harwood, R.F. Jarnot, H.M. Pickett, W.G. Read, P.H. Siegel, R.E. Cofield, M.J. Filipiak, D.A. Flower, J.R. Holden, G.K. Lau, N.J. Livesey, G.L. Manney, H.C. Pumphrey, M.L. Santee, D.L. Wu, D.T. Cuddy, R.R. Lay, M.S. Loo, V.S. Perun, M.J. Schwartz, P.C. Stek, R.P. Thurstans, M.A. Boyles, K.M. Chandra, M.C. Chavez, C. Gun-Shing, B.V. Chudasama, R. Dodge,R.A. Fuller, M.A. Girard, J.H. Jiang, Y. Jiang, B.W. Knosp, R.C. LaBelle, J.C. Lam, K.A. Lee, D. Miller, J.E. Oswald, N.C. Patel, D.M. Pukala, O. Quintero, D.M. Scaff, W. Van Snyder, M.C. Tope, P.A. Wagner, M.J. Walch, 2006, The Earth Observing System Microwave Limb Sounder (EOS MLS) on the Aura satellite, IEEE Trans. Geosci. Remote Sens., **44**, 1075–1092.

Weng, F. and N.C. Grody, 1994, Retrieval of cloud liquid water using the special sensor microwave imager (SSM/I), *J. Geophys. Res.*, **99(D12)**, 25535–25551.

Weng, F., N.C. Grody, R. Ferraro, A. Basist and D. Forsyth, 1997, Cloud liquid water climatology from the Special Sensor Microwave/Imager, *J. Clim.*, **10**,1086–1098.

Weng, F. J. and N. C. Grody, 2000, Retrieval of ice cloud parameters using a microwave imaging radiometer, *J. Atmos. Sci.*, **57**, 1069–1081.

Wentz, F.J., 1997, A well calibrated ocean algorithm for special sensor microwave/imager, *J. Geophys. Res.*, **102**, 8703–8718.

Wentz, F.J. and R.W. Spencer, 1998, SSM/I rain retrievals within a unified all-weather ocean algorithm. *J. Atmos. Sci.*, **55**, 1613–1627.

Wickert, J., C. Reigber, G. Beyerle, R. König, C. Marquardt, T. Schmidt, L. Grunwaldt, R. Galas, T. Meehan, W. Melbourne, and K. Hocke, 2001, Atmosphere sounding by GPS radio occulta- tion: First results from (CHAMP). Geophys. Res. Lett., **28**, 3263–3266.

Wiedner, M., C. Prigent, J. Pardo, O. Nuissier, J.-P. Chaboureau, J.-P. Pinty and P. Mascart, 2004, Modeling of passive microwave responses in convective situations using outputs from

mesoscale models: comparison with TRMM / TMI satellite observations, *J. Geophys. Res.*, **109**, D06214, doi:10.1029/2003/JD004280.

Wilheit, T.T., A.T.C. Chang, M.S.V. Rao, E.B. Rodgers and J.S. Theon, 1977, Satellite technique for quantitatively mapping rainfall rates over oceans, *J. Appl. Meteorol.*, **16**, 551–560.

Wilheit, T.T., A.T.C. Chang, M.S.V. Rao, E.B. Rodgers and J.S. Theon, 1991a, A satellite technique for quantitatively mapping rainfall over oceans, *J. Appl. Oceanic Technol.*, **8**, 118–136.

Wilheit, T.T., A.T.C. Chang, and L.S. Chiu, 1991b, Retrieval of monthly rainfall indices from microwave radiometric measurements using probability distribution functions. *J. Atmos. Oceanic Tech.*, **8**, 118–136.

Winker, D., W. Hunt, and M. McGill, 2007, Initial performance assessment of CALIOP, Geophys. Res. Lett., **34**, L19803, doi:10.1029/2007GL030135.

Wu, D.L., W.G. Read, A.E. Dessler, S.C. Sherwood, and J.H. Jiang, 2005, UARS/MLS cloud ice measurements: Implications for H_2O transport near the tropopause, *J. Atmos. Sci.*, **62**, 518–530.

Wu, D.L., J.H. Jiang, W.G. Read, R.T. Austin, C.P. David, A. Lambert, G.L. Stephens, D.G. Vane, and J.W. Waters, 2008, Validation of Aura MLS cloud Ice Water Content (IWC) measurements, *J. Geophys. Res.*, **113**, D15S10, doi:10.1029/2007JD008931.

Yan, X., V. Ducrocq, P. Poli, M. Hakam, G. Jaubert, and A. Walpersdorf, 2009, Impact of GPS zenith delay assimilation on convective-scale prediction of Mediterranean heavy rainfall. *J. Geophys. Res.*, **114**, D03104, doi:10.1029/2008JD011036.

Zhu, Y. and R. Gelaro, 2008, Observation sensitivity calculations using the adjoint of the gridpoint statistical interpolation (GSI) analysis system, Mon. Wea. Rev., 136, 335–351.

Ziemke, J.R., and S. Chandra, 2003, A Madden-Julian Oscillation in tropospheric zone, Geophys. Res. Lett., **30**, 2182, doi:10.1029/2003GL018523.